

# DEVELOPMENT AND IMPLEMENTATION OF PRACTICAL OPTIMAL LES MODELS

Final Report for Contract F49620-04-1-0032

R. D. Moser<sup>1</sup>, and R. J. Adrian<sup>2</sup>

Department of Theoretical and Applied Mechanics  
University of Illinois, Urbana-Champaign

## 1 Motivation and Objectives

One of the most promising techniques for the prediction of turbulent flows is that of Large Eddy Simulation (LES), in which an under-resolved representation of the turbulence is simulated numerically by modeling the effects of the unresolved small-scales on the simulation. Such simulations have been applied in several flows with reasonable success. However, there are several outstanding problems that need to be addressed before LES can fulfill its promise as a tool for turbulence prediction in engineering flows. The most serious problems limiting the usefulness of LES is the representation of turbulence near walls and other strong inhomogeneities and the dependence of models on the filter and/or numerical discretization.

The optimal LES formulation<sup>1,2</sup> provides a rigorous framework in which to address these issues and to develop and analyze LES models and simulations. Optimal LES modeling has been found to produce accurate LES simulations when based on reliable statistical information, so the primary thrust of the current research is to reduce or eliminate the need for empirical statistical input through theory and modeling of turbulence statistics. When small-scale isotropy is a valid assumption, the Kolmogorov theory and isotropy can provide much information. However, when inhomogeneity and anisotropy are strong, or the Reynolds number is not too large, more information will be required, and models for this are being developed, particularly for near-wall turbulence.

Theoretical models for the turbulence multi-point correlations allow optimal LES models to be implemented relatively simply in production CFD codes, and preliminary implementations in FDL3DI at AFRL have been pursued.

---

<sup>1</sup>Currently Department of Mechanical Engineering, University of Texas

<sup>2</sup>Currently Department of Mechanical and Aerospace Engineering, Arizona State University

Report Documentation Page				Form Approved OMB No. 0704-0188	
Public reporting burden for the collection of information is estimated to average 1 hour per response, including the time for reviewing instructions, searching existing data sources, gathering and maintaining the data needed, and completing and reviewing the collection of information. Send comments regarding this burden estimate or any other aspect of this collection of information, including suggestions for reducing this burden, to Washington Headquarters Services, Directorate for Information Operations and Reports, 1215 Jefferson Davis Highway, Suite 1204, Arlington VA 22202-4302. Respondents should be aware that notwithstanding any other provision of law, no person shall be subject to a penalty for failing to comply with a collection of information if it does not display a currently valid OMB control number.					
1. REPORT DATE <b>31 MAR 2007</b>		2. REPORT TYPE <b>N/A</b>		3. DATES COVERED <b>-</b>	
4. TITLE AND SUBTITLE <b>Development and Implementation of Practical Optimal LES Models</b>				5a. CONTRACT NUMBER	
				5b. GRANT NUMBER	
				5c. PROGRAM ELEMENT NUMBER	
6. AUTHOR(S)				5d. PROJECT NUMBER	
				5e. TASK NUMBER	
				5f. WORK UNIT NUMBER	
7. PERFORMING ORGANIZATION NAME(S) AND ADDRESS(ES) <b>University of Illinois at Urbana-Champaign Urbana, IL 61801</b>				8. PERFORMING ORGANIZATION REPORT NUMBER	
9. SPONSORING/MONITORING AGENCY NAME(S) AND ADDRESS(ES)				10. SPONSOR/MONITOR'S ACRONYM(S)	
				11. SPONSOR/MONITOR'S REPORT NUMBER(S)	
12. DISTRIBUTION/AVAILABILITY STATEMENT <b>Approved for public release, distribution unlimited</b>					
13. SUPPLEMENTARY NOTES <b>The original document contains color images.</b>					
14. ABSTRACT					
15. SUBJECT TERMS					
16. SECURITY CLASSIFICATION OF:			17. LIMITATION OF ABSTRACT <b>SAR</b>	18. NUMBER OF PAGES <b>74</b>	19a. NAME OF RESPONSIBLE PERSON
a. REPORT <b>unclassified</b>	b. ABSTRACT <b>unclassified</b>	c. THIS PAGE <b>unclassified</b>			

## 2 Background & Approach

The starting point for the development of LES is the definition of a spatial filter  $\tilde{\cdot}$ , which can be applied to the Navier-stokes equations to obtain an equation for the filtered velocity  $\tilde{u}_i$ :

$$\frac{\partial \tilde{u}_i}{\partial t} = -\frac{\partial \tilde{u}_i \tilde{u}_j}{\partial x_j} - \frac{\partial \tilde{p}}{\partial x_i} + \frac{1}{\text{Re}} \frac{\partial^2 \tilde{u}_i}{\partial x_j \partial x_j} + M_i, \quad (1)$$

Where  $M_i$  is the sub-grid model (force) term, which includes the divergence of the sub-grid stress as well as terms that arise when the filter does not commute with differentiation. The problem in LES of course is to model  $M_i$ . A very important result of our research<sup>1</sup> is that an LES  $w$  will match the one-time statistics of filtered turbulence  $\tilde{u}$  if and only if the model  $m_i(w)$  of  $M_i$  is given by

$$m_i(w) = \langle M_i(u) | \tilde{u} = w \rangle \quad (2)$$

This model also minimizes the difference between  $M_i$  and  $m_i$  (in the mean-square sense), and so this model has all the properties that one could ask of a sub-grid model. We therefore call it the ideal sub-grid model.

Unfortunately, the conditional average in (2) cannot practically be determined, since the conditions are that the entire filtered velocity field match the entire LES field. However, it can be estimated using stochastic estimation<sup>3</sup> which is a well-established technique for estimating conditional averages. The result is a class of estimation based LES models as first proposed by Adrian<sup>4</sup>. To perform stochastic estimation of the model term  $M_i$ , one must provide correlations of the LES variables  $w$  with the model term, as well as correlations of LES variables with themselves. Previously, before the current effort, this data had been obtained from direct numerical simulations, but this is clearly unacceptable for a predictive LES model. In this research, we develop the theoretical models of the required correlations to be used in an optimal LES model.

As will be shown in the following section, it will usually be sufficient to estimate the subgrid model term  $M$  as linear in the LES variables, thus the correlations which must be determined are:

$$\langle \tilde{u}_j(\mathbf{x}') \tilde{u}_k(\mathbf{x}'') \rangle \quad \text{and} \quad \langle M_i(\mathbf{x}) \tilde{u}_k(\mathbf{x}'') \rangle. \quad (3)$$

We do not, however, generally have theory for these two-point correlations of filtered and model quantities. But we do have theory for multi-point velocity correlations, and as will be shown, the LES correlations (3) can be obtained by applying the filtering operator to the following two and three-point correlations:

$$\mathbb{R}(\mathbf{r}, \mathbf{s}) = \langle \mathbf{u}(\mathbf{r}) \mathbf{u}(\mathbf{s}) \rangle \quad (4)$$

$$\mathbb{B}(\mathbf{r}, \mathbf{s}) = \langle \mathbf{u}(\mathbf{r}) \mathbf{u}(\mathbf{s}) \mathbf{u}(\mathbf{s}) \rangle \quad (5)$$

$$\mathbb{T}(\mathbf{r}, \mathbf{s}, \mathbf{t}) = \langle \mathbf{u}(\mathbf{r}) \mathbf{u}(\mathbf{s}) \mathbf{u}(\mathbf{t}) \rangle \quad (6)$$

Thus, models for these correlation tensors are needed. When the small scales are isotropic, Kolmogorov inertial range theory applies, and this will be sufficient to determine all but  $\mathbb{T}$ , and an extended inertial-range model to determine  $\mathbb{T}$  has also been developed. Furthermore, correlations of filtered velocities with themselves can be computed directly from an LES, thus it is possible to determine some of the necessary correlations dynamically in a running LES. In this case, a model is only needed for the two-point third order correlations  $\mathbb{B}$ .

When the assumption of small-scale isotropy and homogeneity are not valid, the models for the required correlations must be more complex. The most common example of this situation is near-wall turbulence. In the log-layer of wall-bounded turbulence, however, self-similarity of the correlations<sup>5</sup> can be used to represent the inhomogeneity. To model anisotropy, we extend the description of single-point anisotropy in terms of structure tensors<sup>6</sup> to the two-point correlation.

With models of the multi-point correlations in hand, and making use of dynamic procedures, practical optimal models that do not require DNS data can be formulated. And these have been tested in non-wall-bounded flows.

### 3 Supported Research

To pursue the objectives defined above, a number of research activities were pursued under the current grant. These are described briefly below and in more detail in the following subsections, and the referenced publications.

1. **Development and Testing of Theoretical/Dynamic OLES Models:** To produce OLES models for turbulence that is isotropic in the small scales, theoretical expressions for the correlations  $\mathbb{R}$  and  $\mathbb{B}$ , are readily available from Kolmogorov inertial range theory. However, the three-point third-order correlation is more difficult. To avoid needing *a priori* information on the three-point correlation, a dynamic approach in which correlation of LES variables with themselves is determined from the LES as it runs, was formulated. It was implemented along with a the theoretical model for  $\mathbb{B}$ , and tested in isotropic turbulence and a free-shear layer. An initial implementation in a (compressible) production CFD code (FDL3DI) was also pursued.
2. **Development of a Model for the Three-Point Correlation:** No previous model for the three-point third-order correlation had previously been developed because of the complexity of this object. A model of this tensor was developed however, by recasting a classical result<sup>7</sup> for the most general tensor form, and selecting for the scalar functions appearing in the form, the simplest expressions that can possibly be consistent with the known inertial-range scaling. This produced a tensor representation with 4 adjustable constants, which was fit to DNS data.
3. **Modeling the Two-Point Correlation in Wall-Bounded Turbulence:** To formulate near-wall OLES models, the two-point second and third order correlations valid in the log-layer are needed. We concentrate first on the second-order correlation, but the third-order correlation can be determined in terms of the second-order. There are three complications that have been addressed: inhomogeneity, anisotropy and finite Reynolds number. Inhomogeneity and finite Reynolds number effects are treated together, because in near-wall turbulence the effective Reynolds number of the turbulence varies in the wall-normal direction. A general anisotropy model for the two-point correlation was developed in terms of the structure-tensor formulation devised by Kassinos, Reynolds & Rogers<sup>6</sup>.
4. **Testing and Evaluation of the Filtered Wall Formulation for the Wall-Layer:** In previous work, the filtered wall LES formulation was devised, which avoids many of the problems of

very near-wall turbulence, essentially by filtering them out. This modeling approach was further tested and modified to characterize the performance of the model. Further it is being reformulated for finite volumes, instead of the spectral methods originally used.

## 4 Development and Testing of Theoretical/Dynamic OLES Models

It was shown previously<sup>8</sup> that finite-volume “filtering” in which discrete volume averages constitute the LES variables, yields a good approximation to the ideal LES of isotropic turbulence. However, this assessment relied on the use of DNS data to compute the necessary correlations. The dependence of the correlations on DNS data does not allow the use of OFVLES models in other flows. Alternative methods for determining the correlations, which do not rely on detailed empirical data, must be developed. In this chapter, theoretical and dynamical approaches for determining the correlations in isotropic turbulence OFVLES models are described.

### 4.1 Theoretical Modeling of Correlations

Theoretical modeling of the correlations in OFVLES will be restricted to the ones required for the convective fluxes ( $M_{\text{conv}}$ ) for two reasons. The theory used in modeling the correlations, Kolmogorov’s scaling laws for velocity structure functions<sup>9–13</sup>, is strictly valid only in the limit of an infinite Reynolds number. Also, the viscous terms’ contributions to the evolution are small far from solid boundaries. Close to solid boundaries, the current theoretical formulations are not valid, efforts to address this problem are described in section 6.

In this section, the convective fluxes are defined as

$$M_{ij} = \int_{\partial\Omega_{ji}} u_j u_k n_k d\mathbf{x}'. \quad (7)$$

where the extra  $i$  and  $j$  subscripts are introduced to represent all convective fluxes through a single expression. With this notation, the estimation equation may be rewritten as

$$\langle m_{ij} E_k \rangle = \langle M_{ij} E_k \rangle. \quad (8)$$

Substitution of the expressions for the model and events in the estimation equation, Eq. (8), yields a linear system of equations for the model coefficients:

$$\langle M_{ij} \rangle = A_{ij} + \sum_{\alpha} L_{ijk}^{\alpha} \langle w_k^{\alpha} \rangle + \sum_{\alpha, \beta} Q_{ijkl}^{\alpha\beta} \langle w_k^{\alpha} w_l^{\beta} \rangle, \quad (9)$$

$$\langle w_m^{\gamma} M_{ij} \rangle = A_{ij} \langle w_m^{\gamma} \rangle + \sum_{\alpha} L_{ijk}^{\alpha} \langle w_k^{\alpha} w_m^{\gamma} \rangle + \sum_{\alpha, \beta} Q_{ijkl}^{\alpha\beta} \langle w_k^{\alpha} w_l^{\beta} w_m^{\gamma} \rangle, \quad (10)$$

$$\langle w_m^{\gamma} w_n^{\delta} M_{ij} \rangle = A_{ij} \langle w_m^{\gamma} w_n^{\delta} \rangle + \sum_{\alpha} L_{ijk}^{\alpha} \langle w_k^{\alpha} w_m^{\gamma} w_n^{\delta} \rangle + \sum_{\alpha, \beta} Q_{ijkl}^{\alpha\beta} \langle w_k^{\alpha} w_l^{\beta} w_m^{\gamma} w_n^{\delta} \rangle. \quad (11)$$

To close these equations, the following correlations of the filtered velocity must be computed:

$$I_{ij}^0(s) = \langle M_{ij} \rangle, \quad (12)$$

$$I_{ijm}^1(s, \gamma) = \langle w_m^\gamma M_{ij} \rangle, \quad (13)$$

$$I_{km}^2(\alpha, \gamma) = \langle w_k^\alpha w_m^\gamma \rangle, \quad (14)$$

$$I_{klm}^3(\alpha, \beta, \gamma) = \langle w_k^\alpha w_l^\beta w_m^\gamma \rangle, \quad (15)$$

$$I_{ijmn}^4(s, \gamma, \delta) = \langle w_m^\gamma w_n^\delta M_{ij} \rangle, \quad (16)$$

$$I_{klmn}^5(\alpha, \beta, \gamma, \delta) = \langle w_k^\alpha w_l^\beta w_m^\gamma w_n^\delta \rangle, \quad (17)$$

where  $s$  is the surface over which the flux is computed. Note that  $\langle w \rangle = 0$ , due to homogeneity and Galilean invariance of the filtered equation.

The integrals representing the effect of the finite-volume filter on the unfiltered velocities can be commuted with the averaging operator, yielding functions that are integrals of correlations of the unfiltered velocities:

$$I_{ij}^0(s) = \int_s \langle u_i(\mathbf{x}) u_j(\mathbf{x}) \rangle d\mathbf{x}, \quad (18)$$

$$I_{ijk}^1(s, \alpha) = \int_\alpha \int_s \langle u_i(\mathbf{x}) u_j(\mathbf{x}) u_k(\mathbf{x}') \rangle d\mathbf{x} d\mathbf{x}', \quad (19)$$

$$I_{ij}^2(\alpha, \beta) = \int_\beta \int_\alpha \langle u_i(\mathbf{x}) u_j(\mathbf{x}') \rangle d\mathbf{x} d\mathbf{x}', \quad (20)$$

$$I_{ijk}^3(\alpha, \beta, \gamma) = \int_\gamma \int_\beta \int_\alpha \langle u_i(\mathbf{x}) u_j(\mathbf{x}') u_k(\mathbf{x}'') \rangle d\mathbf{x} d\mathbf{x}' d\mathbf{x}'', \quad (21)$$

$$I_{ijkl}^4(s, \alpha, \beta) = \int_\beta \int_\alpha \int_s \langle u_i(\mathbf{x}) u_j(\mathbf{x}) u_k(\mathbf{x}') u_l(\mathbf{x}'') \rangle d\mathbf{x} d\mathbf{x}' d\mathbf{x}'', \quad (22)$$

$$I_{ijkl}^5(\alpha, \beta, \gamma, \delta) = \int_\delta \int_\gamma \int_\beta \int_\alpha \langle u_i(\mathbf{x}) u_j(\mathbf{x}') u_k(\mathbf{x}'') u_l(\mathbf{x}''') \rangle d\mathbf{x} d\mathbf{x}' d\mathbf{x}'' d\mathbf{x}'''. \quad (23)$$

Therefore, to close the system of estimation equations for the quadratic OFVLES model coefficients for the convective fluxes, the following correlations of the unfiltered velocities are required:

$$R_{ij}(\mathbf{r}) = \langle u_i(\mathbf{x}) u_j(\mathbf{x} + \mathbf{r}) \rangle, \quad (24)$$

$$T_{ijk}(\mathbf{0}, \mathbf{r}) = \langle u_i(\mathbf{x}) u_j(\mathbf{x}) u_k(\mathbf{x} + \mathbf{r}) \rangle, \quad (25)$$

$$T_{ijk}(\mathbf{r}^1, \mathbf{r}^2) = \langle u_i(\mathbf{x}) u_j(\mathbf{x} + \mathbf{r}^1) u_k(\mathbf{x} + \mathbf{r}^2) \rangle, \quad (26)$$

$$F_{ijkl}(\mathbf{0}, \mathbf{r}^2, \mathbf{r}^3) = \langle u_i(\mathbf{x}) u_j(\mathbf{x}) u_k(\mathbf{x} + \mathbf{r}^2) u_l(\mathbf{x} + \mathbf{r}^3) \rangle, \quad (27)$$

$$F_{ijkl}(\mathbf{r}^1, \mathbf{r}^2, \mathbf{r}^3) = \langle u_i(\mathbf{x}) u_j(\mathbf{x} + \mathbf{r}^1) u_k(\mathbf{x} + \mathbf{r}^2) u_l(\mathbf{x} + \mathbf{r}^3) \rangle. \quad (28)$$

Hence, expressions for the two-point, second- and third-order, the three-point, third-order and the three- and four-point, fourth-order correlations of the unfiltered velocities are needed.

To model these velocity correlations, three assumptions are necessary:

1. The turbulence is isotropic, at least at the length scales encountered in the correlations.

2. The separations ( $\mathbf{r}$ ,  $\mathbf{r}^1$ ,  $\mathbf{r}^2$  and  $\mathbf{r}^3$ ) are within the Kolmogorov inertial range.
3. The Reynolds number of the turbulence is sufficiently large that it may be considered infinite.

These assumptions are consistent with the ones used by Kolmogorov to deduce expressions for second- and third-order longitudinal structure functions, which are used to derive the two-point, second- and third-order velocity correlations:

$$R_{ij}(\mathbf{r}) = u^2 \delta_{ij} + \frac{C_1}{6} \epsilon^{2/3} |r|^{-4/3} (r_i r_j - 4|r|^2 \delta_{ij}), \quad (29)$$

$$T_{ijk}(\mathbf{0}, \mathbf{r}) = \frac{\epsilon}{15} \left( \delta_{ij} r_k - \frac{3}{2} (\delta_{ik} r_j + \delta_{jk} r_i) \right). \quad (30)$$

For the fourth-order velocity correlations, the controversial quasi-normal approximation (QNA) is used. In this approximation, the fourth-order cumulants are assumed to vanish as with normally distributed variables. This assumption allows the expression of the fourth-order correlations in terms of products of second-order correlations:

$$F_{ijkl}(\mathbf{r}^1, \mathbf{r}^2, \mathbf{r}^3) = R_{ij}(\mathbf{r}^1) R_{ij}(\mathbf{r}^3 - \mathbf{r}^2) + R_{ij}(\mathbf{r}^2) R_{ij}(\mathbf{r}^3 - \mathbf{r}^1) + R_{ij}(\mathbf{r}^3) R_{ij}(\mathbf{r}^2 - \mathbf{r}^1). \quad (31)$$

While experimental<sup>14</sup> and numerical<sup>15</sup> evidence has shown that this approximation is quite accurate in isotropic turbulence, use of the QNA in two-point closure models has led to negative energy spectra—a review of the issues may be found in Lesieur<sup>16</sup>. However, in this case, the anomalous behavior of the spectra was due to unrestrained growth of the third-order moments during the simulation and, in the application to OFVLES, third-order correlations are not determined in this way. It must be emphasized that the moment equation simulations using QNA were quite accurate for small time intervals and displayed unphysical behavior only after long simulation times<sup>16</sup>.

The only remaining correlation needed for closure of the estimation equations is the three-point, third-order velocity correlation. The general expression for this correlation is more easily expressed in wave-space<sup>14</sup>. The six-dimensional Fourier transform of  $\mathbf{T}$  and its inverse are defined by

$$\hat{T}_{ijk}(\mathbf{k}^1, \mathbf{k}^2) = \frac{1}{(2\pi)^6} \int_{\mathbf{r}^1} \int_{\mathbf{r}^2} T_{ijk}(\mathbf{r}^1, \mathbf{r}^2) e^{-i(\mathbf{k}^1 \cdot \mathbf{r}^1 + \mathbf{k}^2 \cdot \mathbf{r}^2)} d\mathbf{r}^1 d\mathbf{r}^2 \quad (32)$$

$$T_{ijk}(\mathbf{r}^1, \mathbf{r}^2) = \int_{\mathbf{k}^1} \int_{\mathbf{k}^2} \hat{T}_{ijk}(\mathbf{r}^1, \mathbf{r}^2) e^{i(\mathbf{k}^1 \cdot \mathbf{r}^1 + \mathbf{k}^2 \cdot \mathbf{r}^2)} d\mathbf{k}^1 d\mathbf{k}^2, \quad (33)$$

and the general expression for  $\hat{\mathbf{T}}$  is

$$\begin{aligned} \hat{T}_{ijk}(\mathbf{k}^1, \mathbf{k}^2) = & -i\mathcal{P}_{im}(-\mathbf{k}^1 - \mathbf{k}^2) \mathcal{P}_{jn}(\mathbf{k}^1) \mathcal{P}_{kp}(\mathbf{k}^2) (\Phi(\kappa^1, \kappa^2, \kappa^3) k_m^1 \delta_{np} - \Phi(\kappa^3, \kappa^2, \kappa^1) k_n^2 \delta_{mp} \\ & + \Phi(\kappa^1, \kappa^3, \kappa^2) k_p^1 \delta_{nm} + \Psi(\kappa^1, \kappa^2, \kappa^3) k_m^1 k_n^2 k_p^1), \end{aligned} \quad (34)$$



where  $\kappa^1 = |k^1|$ ,  $\kappa^2 = |k^2|$  and  $\kappa^3 = |k^1 + k^2|$ . The divergence-free projection operator  $\mathcal{P}$  is defined by

$$\mathcal{P}_{ij}(\mathbf{k}) = \delta_{ij} - \frac{k_i k_j}{|\mathbf{k}|^2}. \quad (35)$$

Using the QNA to close the evolution equation for the third-order moments, Proudman & Reid<sup>17</sup> derived the following equations for  $\Phi$  and  $\Psi$ :

$$\frac{\partial}{\partial t} \Phi(\kappa^1, \kappa^2, \kappa^3) = f(\kappa^3) [f(\kappa^2) - f(\kappa)] - \nu \left( (\kappa^1)^2 + (\kappa^2)^2 + (\kappa^3)^2 \right) \Phi(\kappa^1, \kappa^2, \kappa^3) \quad (36)$$

$$\frac{\partial}{\partial t} \Psi(\kappa^1, \kappa^2, \kappa^3) = -\nu \left( (\kappa^1)^2 + (\kappa^2)^2 + (\kappa^3)^2 \right) \Psi(\kappa^1, \kappa^2, \kappa^3), \quad (37)$$

where  $f(\kappa) = E(\kappa)/4\pi\kappa^2$  and  $E(\kappa)$  is the three-dimensional energy spectrum.

For stationary turbulence, the function  $\Psi$  vanishes. For  $\Phi$ , the eddy-damping approximation (EDQNM) is introduced to avoid the realizability issues encountered when using the QNA for closure. The damping term actually reproduces the damping effects of the fourth-order cumulants that were discarded in the QNA. Using the EDQNM approximation and assuming an infinite Reynolds number (so that the viscous term may be dropped) yield the following equation for  $\Phi$ :

$$\Phi(\kappa^1, \kappa^2, \kappa^3) = \frac{f(\kappa^3) [f(\kappa^2) - f(\kappa)]}{\mu(\kappa^1, \kappa^2, \kappa^3)}. \quad (38)$$

Finding the inverse Fourier transform of  $\Phi$  is equivalent to finding the real-space representation of the three-point, third-order correlation  $\mathbf{T}$ . Unfortunately, the analytical inverse Fourier transform of  $\Phi$  is complicated due to the singular behavior of the integrand at the origin. There has been no solution to this problem to date.

However, Eq. (38) can still produce valuable information. The damping term is usually of the form

$$\mu(\kappa^1, \kappa^2, \kappa^3) \sim \epsilon^{1/3} \mathcal{F}(\kappa^1, \kappa^2, \kappa^3), \quad (39)$$

where  $\mathcal{F}$  is a function only of geometric quantities, not of any flow-dependent quantities. Substituting the expressions for the spectra

$$E(\kappa) = C\epsilon^{2/3} k^{-5/3} \quad (40)$$

and the damping term into Eq. (38) yields a function for  $\hat{T}$  of the form

$$\hat{T}_{ijk}(\kappa^1, \kappa^2, \kappa^3) = \epsilon \mathcal{H}_{ijk}(\kappa^1, \kappa^2, \kappa^3). \quad (41)$$

The scaling equation for the Fourier coefficients of the three-point, third-order velocity correlation, Eq. (41), may also be found in a more straightforward way by invoking Kolmogorov's scaling arguments for structure functions in the inertial range<sup>9,10</sup>. Kolmogorov postulates that, in the inertial range of turbulence, the velocity structure function may depend only on the dissipation and separation, since it is far removed in scale from the production and dissipation ranges (where viscosity

and the length scales of the forcing would be of importance). Therefore, by using dimensional analysis, clearly the only possible functional form for the three-point, third-order velocity correlation is linear in dissipation, yielding Eq. (41).

Note that the three-point, third-order velocity correlation is a linear function of dissipation,  $\epsilon$ , multiplied by a term is a function only of geometrical or spatial properties of the grid/filter,  $\mathcal{H}$ . Therefore, the function for the correlation can be divided into two parts, one which depends only on the flow, and is a known function of dissipation, and one that depends only on geometric properties of the numerical grid/filter. The geometry-dependent function is unknown and can be approximated only through a difficult inverse Fourier transform. However, for a given grid configuration, a single DNS may be used to supply the correlation data for any flow situation.

Even in the simple case of a cubic grid, such as the one used in the isotropic turbulence simulations in this dissertation, it is not possible to derive closed forms for the integrated correlations, with the exception of the two-point, third-order correlation,  $I^1$ . Function  $I^1$  can easily be computed for the cubic grid due to the linear nature of the integrand:

$$\begin{aligned}
I_{ijk}^1(s, \alpha) &= \frac{1}{\Delta^5} \int_{\alpha} \int_s \frac{\epsilon}{15} \left( \delta_{ij} (x'_k) - \frac{3}{2} (\delta_{ik} (x'_j - x_j) + \delta_{jk} (x'_i - x_i)) \right) d\mathbf{x} d\mathbf{x}' \\
&= \frac{\epsilon}{15\Delta} \left[ \delta_{ij} \frac{x'_k{}^2}{2} \Big|_{x_k^\alpha - \Delta/2}^{x_k^\alpha + \Delta/2} - \frac{3}{2} \left( \delta_{ik} \frac{x'_j{}^2 \Big|_{x_j^\alpha - \Delta/2}^{x_j^\alpha + \Delta/2} - x_j^2 \Big|_{-\Delta/2}^{\Delta/2}}{2} + \delta_{jk} \frac{x'_i{}^2 \Big|_{x_i^\alpha - \Delta/2}^{x_i^\alpha + \Delta/2} - x_i^2 \Big|_{-\Delta/2}^{\Delta/2}}{2} \right) \right] \\
&= \frac{\epsilon}{15\Delta} \left[ \delta_{ij} \Delta x_k^\alpha - \frac{3}{2} (\delta_{ik} \Delta x_j^\alpha + \delta_{jk} \Delta x_i^\alpha) \right] \\
&= \frac{\epsilon}{15} \left( \delta_{ij} x_k^\alpha - \frac{3}{2} (\delta_{ik} x_j^\alpha + \delta_{jk} x_i^\alpha) \right), \tag{42}
\end{aligned}$$

where  $\mathbf{x}^\alpha$  is the center-point of the cubic volume  $\alpha$  and  $\Delta$  is the grid spacing.

The integrals dependent on the two-point, second-order correlations— $I^2$ ,  $I^4$  and  $I^5$ —are singular at the origin,  $\mathbf{r}$ , while the integrand for  $I^3$  is not even known. In this dissertation, Gauss quadrature was used to compute the integrals with known integrands, including  $I^1$ .

#### 4.1.1 Theoretical Scaling of the Estimation Equations

The theoretical expressions derived in the previous section can be used to suggest the appropriate scaling for the integral functions  $I$  and the coefficients  $A$ ,  $L$ , and  $Q$ <sup>18</sup>. The scalings for functions and coefficients for the convective flux OFVLES model, with dependencies on volumes and

surfaces removed to simplify notation, are

$$\begin{aligned}
I_{ij}^0 &= u^2 \Delta^2 \delta_{ij} \bar{I}_{ij}^0 \\
I_{ij}^1 &= \epsilon \Delta^6 \bar{I}_{ij}^1 \\
I_{ij}^2 &= \epsilon^{2/3} \Delta^{20/3} \bar{I}_{ij}^2 \\
I_{ij}^3 &= \epsilon \Delta^{10} \bar{I}_{ij}^3 \\
I_{ij}^4 &= u^4 \Delta^8 \bar{I}_{ij}^4 \\
I_{ij}^5 &= u^4 \Delta^{12} \bar{I}_{ij}^5 \\
A_{ij} &= u^2 \Delta^2 \delta_{ij} \\
L_{ij} &= \left( \frac{\epsilon}{\Delta^2} \right)^{1/3} \bar{L}_{ij} \\
Q_{ij} &= \frac{1}{\Delta^4} \bar{Q}_{ij},
\end{aligned} \tag{43}$$

where the quantities with an overbar are order-one scaled quantities.

Substituting these scalings in the estimation equations, Eq. (9)–(11), results in the scaled estimation equations

$$\bar{I}_{ij}^0 = \bar{A}_{ij} + \left( \frac{\epsilon \Delta}{u^3} \right)^{2/3} \sum \sum \bar{Q}_{ij} \bar{I}_{ij}^2, \tag{44}$$

$$\bar{I}_{ij}^1 = \sum \bar{L}_{ij} \bar{I}_{ij}^2 + \sum \sum \bar{Q}_{ij} \bar{I}_{ij}^3, \tag{45}$$

$$\bar{I}_{ij}^4 = \left( \frac{\epsilon \Delta}{u^3} \right)^{2/3} \bar{A}_{ij} \bar{I}_{ij}^2 + \left( \frac{\epsilon \Delta}{u^3} \right)^{4/3} \sum \bar{L}_{ij} \bar{I}_{ij}^3 + \sum \sum \bar{Q}_{ww} \bar{I}_{ww}^5. \tag{46}$$

Two length scales appear in the estimation equations: the filter scale,  $\Delta$ , and the large turbulence scale,  $u^3/\epsilon$ . The ratio of the filter scale to the large turbulence scale appears in Eq. (44), multiplying the quadratic coefficient, and in (46), multiplying both the constant and linear coefficients. In LES, the filter scale should be in the inertial range, so that the ratio of the filter scale to the large-turbulence scale should be small and, therefore, Eqs. (44) and (46) should uncouple from Eq. (45). In the limit when this ratio tends to zero,  $\Delta \ll u^3/\epsilon$ , the system of estimation equations becomes

$$\bar{I}_{ij}^0 = \bar{A}_{ij}, \tag{47}$$

$$\bar{I}_{ij}^1 = \sum \bar{L}_{ij} \bar{I}_{ij}^2 + \sum \sum \bar{Q}_{ij} \bar{I}_{ij}^3, \tag{48}$$

$$\bar{I}_{ij}^4 = \sum \sum \bar{Q}_{ww} \bar{I}_{ww}^5, \tag{49}$$

where Eq. (47) is an uncoupled equation for the constant coefficient  $A$ , Eq. (49) is an uncoupled equation for the quadratic coefficient  $Q$ , and Eq. (48) is the equation for the linear coefficient  $L$ , which is dependent on the solution for  $Q$ .

#### 4.1.2 Results for Theory-Derived Convective Flux Models

The comparison of theory- and DNS-based OFVLES models is difficult due to the low Reynolds number of the DNS simulations and the lack of viscous-flux models for infinite-Reynolds-number theory-based OFVLES. However, it is of interest to compare the results of the theory- and DNS-based OFVLES models even though the theory-based model is used in simulations outside its range of applicability. Closure of the theory-based models is achieved using scaled DNS data for the third-order, three-point velocity correlation. The values for the velocity variance,  $u^2$ , and the dissipation,  $\epsilon$ , used in computing the theory-based correlations, were set from the DNS data and the energy input for the simulation, respectively.

*A posteriori* statistics for theory- and DNS-based OFVLES, and dynamic Smagorinsky models are compared in Fig. 1. Note that both the DNS-based OFVLES and dynamic Smagorinsky models contain viscous terms, but the theory-based model does not. While the theory-based model most accurately simulates the third-order structure function, especially at the smallest separations, the energy spectrum results are not as good. The large wavenumber energy spectrum from the theory-based model is considerably lower than the filtered DNS result and that of the other models. The relatively low Reynolds number of the simulated flow may be the reason for such discrepancy, given that the theory-based model is strictly valid only in the infinite Reynolds number limit.

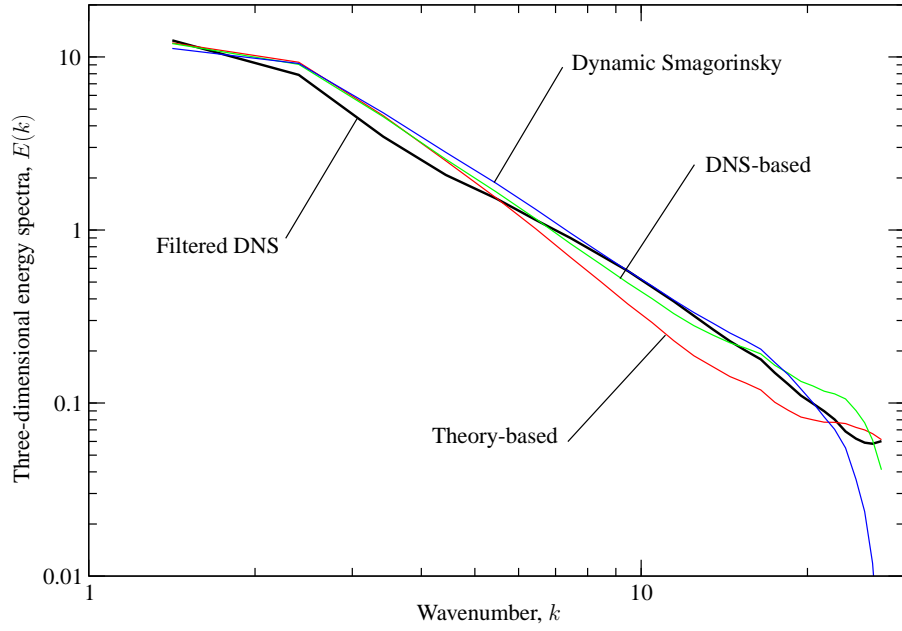
A study of the effects of stencil geometry, has been conducted for the theory-derived OFVLES models, to confirm that the conclusions reached in DNS-based OFVLES<sup>8,19</sup> are valid for the theoretically derived models. In addition, a grid/filter refinement analysis for a high-Reynolds-number isotropic-turbulence case was performed, which was not possible with the DNS-based OFVLES models, which are restricted to a single Reynolds number and grid configuration.

**Analysis of linear part of the theory-derived models** As in the analysis of the DNS-based OFVLES models, two quadratic flux models with identical quadratic parts (with events identical to the S4 DNS-based model) but with different sized linear stencils displayed little variation in both *a priori* and *a posteriori* results. The *a priori* variation, displayed in Table 1, changes insignificantly when increasing the size of the linear stencil, consistent with the conclusion reached when analyzing the DNS-based models. The *a posteriori* statistics, Fig. 2, also display little variation in the results between the model using the smaller  $1 \times 1 \times 2$  stencil and the one using the larger  $1 \times 1 \times 4$  stencil. A small difference in the spectra is noticed only at the highest wavenumbers, while the structure functions for the two models show only minimal differences throughout the separation range.

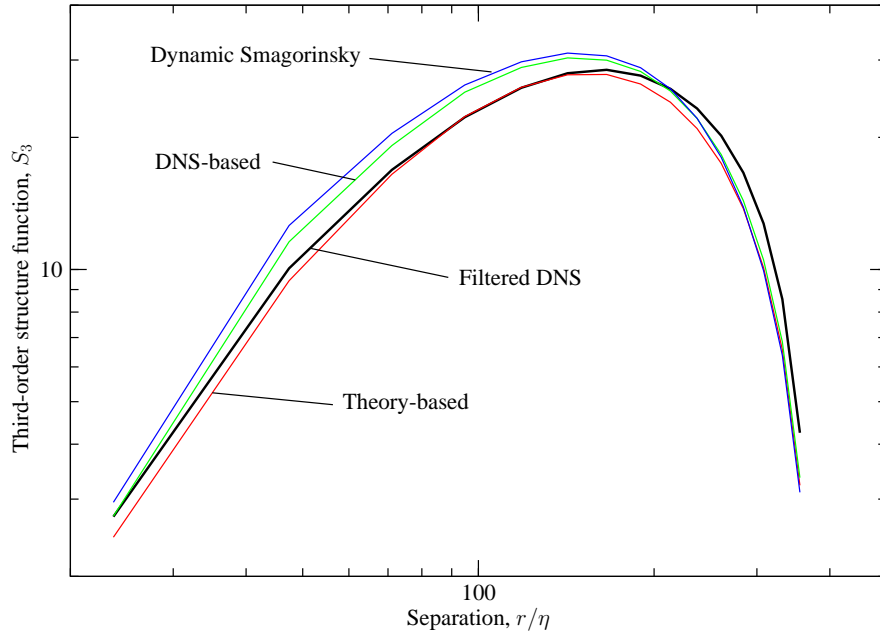
With the simplification afforded by the small stencil for the linear part of the OFVLES model and the decoupling of the quadratic part, it is possible to write a simplified expression for the coefficient  $L$  for the linear part:

$$L_{ij} = \frac{\langle M_{ij} w_i^- \rangle - \sum_{\alpha, \beta} Q_{ij} \langle w_i^\alpha w_j^\beta w_i^- \rangle}{\langle w_i^+ w_i^- \rangle - \langle w_i^- w_i^- \rangle}, \quad (50)$$

where there is no sum on repeated indices. The  $+$  and  $-$  superscripts denote velocity events in volumes shifted in the positive and negative directions, respectively, normal to the flux face. The numerator of Eq. (50) represents the energy transfer due to the linear part of the model and is



(a) Three-dimensional energy spectra,  $E(k)$



(b) Third-order structure function,  $S_3$

Figure 1: Filtered DNS statistics compared with theory-based OFVLES, DNS-based OFVLES and dynamic Smagorinsky results.

Table 1: *A priori* relative estimation variation for theory-based models with varying linear stencil geometry only. DNS-based results repeated for comparison.

Linear stencil	DNS-based		Theory-based	
	$M_{uw}$	$M_{ww}$	$M_{uw}$	$M_{ww}$
$1 \times 1 \times 2$	0.3165	0.2071	0.3193	0.2179
$1 \times 1 \times 4$	0.3165	0.2070	0.3193	0.2186

Table 2: *A priori* relative estimation variation for theory-based models with differing constraints for the quadratic part. DNS-based results are repeated for reference.

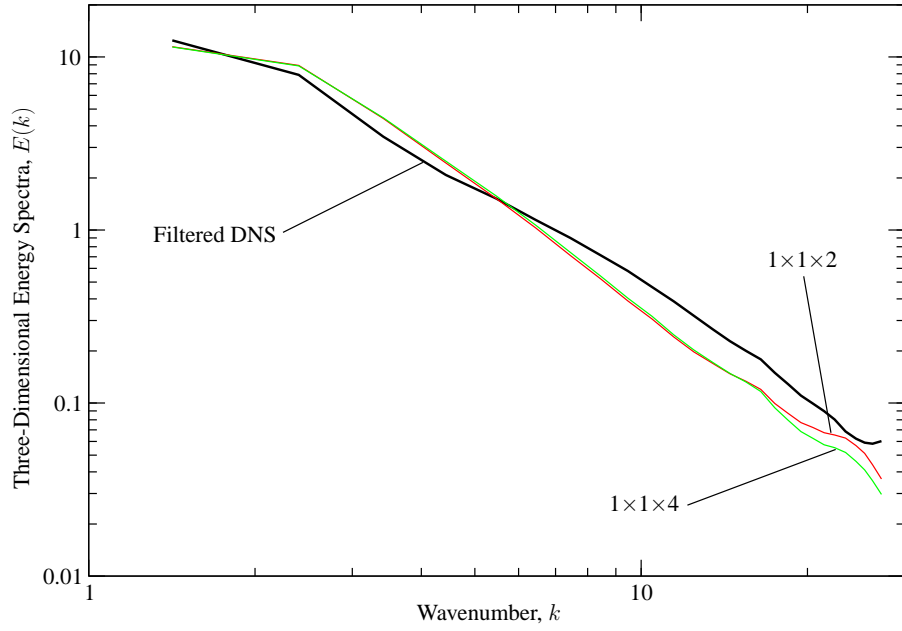
Quadratic Stencil Size	Type	DNS-based Flux Model		Theory-based Flux Model	
		$M_{uw}$	$M_{ww}$	$M_{uw}$	$M_{ww}$
$1 \times 1 \times 2$	Optimal	0.3165	—	0.3193	—
	Standard	0.3317	—	0.3320	—
$1 \times 1 \times 4$	Optimal	—	0.2145	—	0.2179
	2 DOF	—	0.2168	—	0.2187
	1 DOF	—	0.2168	—	0.2181
	Standard	—	0.2372	—	0.2395

simply the theoretical energy transfer of the flux minus the energy transfer due to the quadratic part of the model.

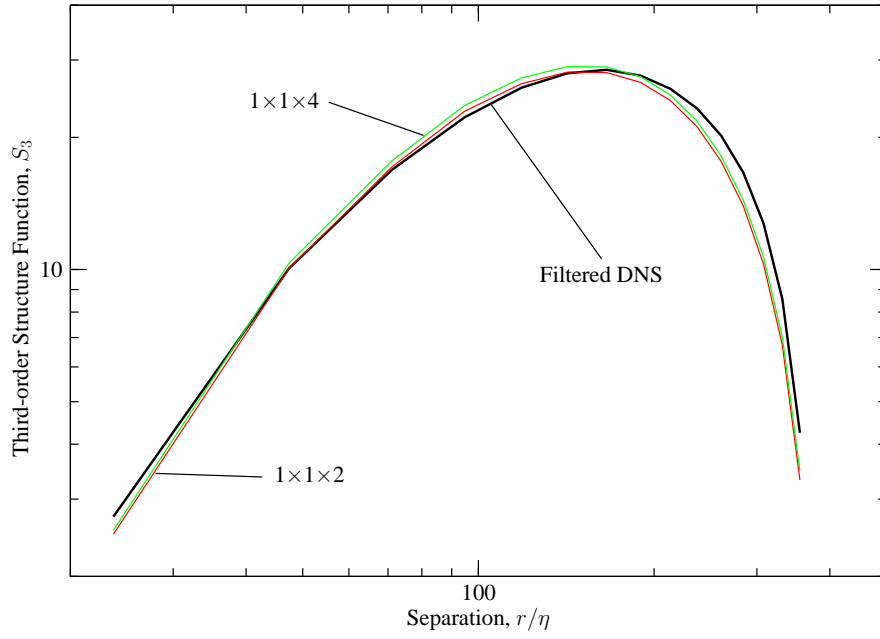
**Analysis of quadratic part of the theory-derived models** To corroborate the conclusion arrived at previously, based on DNS data, that standard discretizations for the quadratic part of the convective flux models are accurate representations of the ideal LES, with negligible difference in accuracy when compared with optimal models, is repeated for the theory-based OFVLES models.

In Table 2 the *a priori* variation for the theory-based OFVLES models are displayed, along with DNS-based variations for comparison. The trend for the theory-based models is similar to the DNS-based ones. The *a priori* variation for models with a single DOF is only slightly larger than that of the optimal model, while the standard discretizations have variations that are around 10% larger. Notice that the *a priori* variations of the theory-based models are only slightly larger than the DNS-based ones, despite the fact that the variations are computed based on low-Reynolds-number data.

In Fig. 3, *a posteriori* statistics for the theory-based models with varying quadratic parts are displayed. The difference among the energy spectra of the different models is negligible in most of the wavenumber range. Only at the highest wavenumber is it possible to distinguish the statistics of the different models. The result is similar for the third-order structure function, reinforcing



(a) Three-dimensional energy spectra,  $E(k)$



(b) Third-order structure function,  $S_3$

Figure 2: Filtered DNS statistics compared with theory-based OFVLES results for varying linear part stencil sizes.

the conclusion reached previously, that is, that the standard discretization for the quadratic part of the convective flux model is sufficiently accurate, being negligibly less accurate than the optimal model.

**Grid/Filter refinement for high-Reynolds-number turbulence** A high-Reynolds-number flow was also simulated using theory-based models. The results obtained for this case are compared with a filtered infinite-Reynolds-number theoretical energy spectrum and a grid/filter refinement study was also conducted (Fig. 4).

No grid convergence is observed, since the filter width is varying among the different simulations, but the dependence of the solutions on the filter width is as expected. The three-dimensional energy spectra of the more refined models clearly becomes asymptotic to the filtered theoretical energy spectrum. The third-order structure functions converge to a linear in  $r$  dependence in the central range of separation values, as clearly seen in the  $128^3$  simulation, which is representative of inertial-range energy transfer. The larger separations are affected by the forcing; the small separation energy transfer is damped by the filtering. These results demonstrate that the theoretical modeling of the velocity correlations necessary for OFVLES allows the extension of optimal models to high-Reynolds-number turbulence, though a treatment for third-order, three-point correlation is needed.

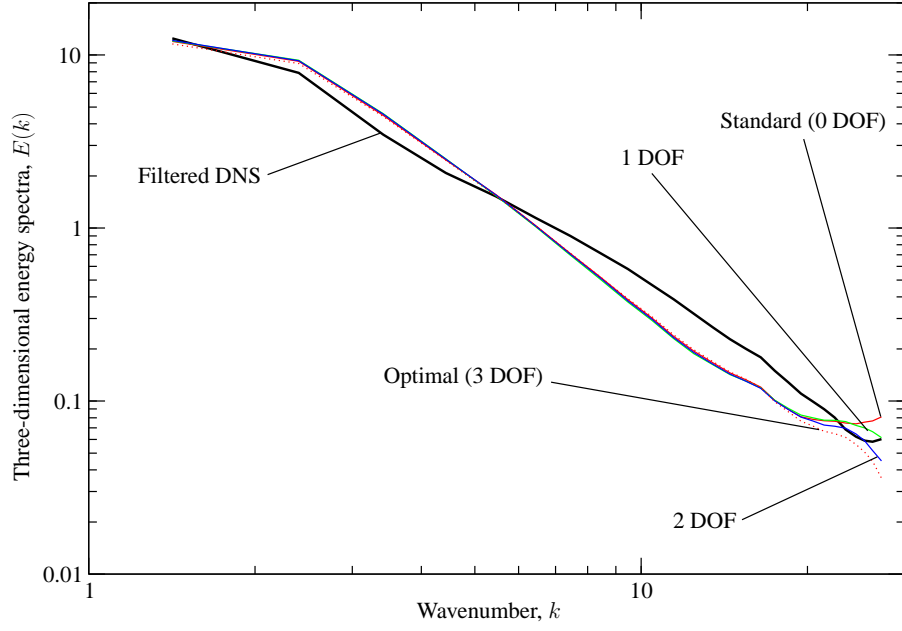
## 4.2 Dynamic Computation of Correlations

In the previous section, theory-based and scaled DNS velocity correlations were used to extend OFVLES models to high-Reynolds-number turbulence. Dependence on DNS data was restricted only to the three-point, third-order velocity correlations in a given grid configuration. To remove the dependence on DNS data completely, an alternate way of computing the three-point, third-order velocity correlations is needed. It is also important to derive correlations for turbulence that departs from the assumptions made in the preceding section, such as near-wall and low-Reynolds-number flows, to extend OFVLES to more complex flows.

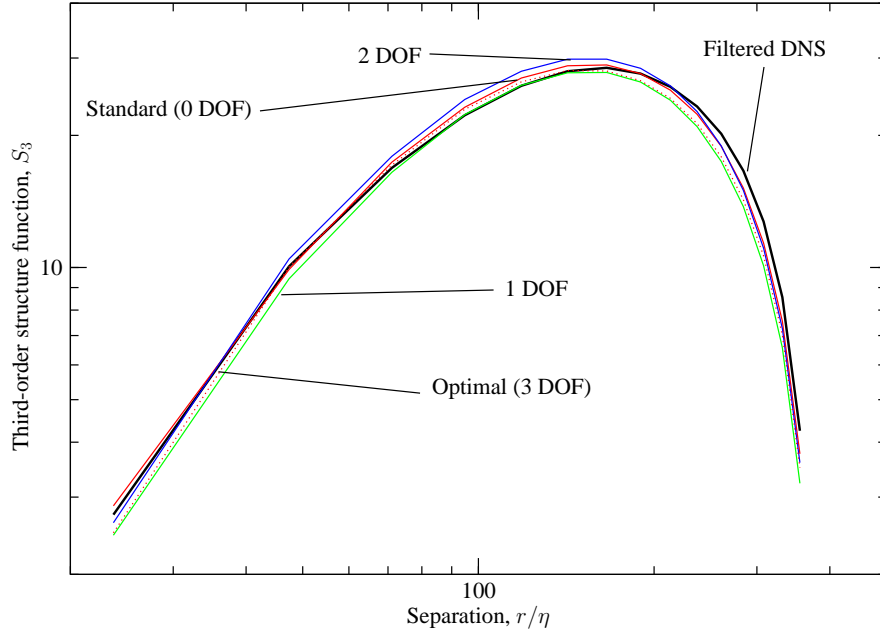
The estimate–event correlations,  $\langle mE_i \rangle$ , appearing on the right-hand side of the estimation equations, Eqs. (9)–(11), can be rewritten as  $C_j \langle E_i E_j \rangle$ , where  $\langle E_i E_j \rangle$  is a matrix of event–event correlations, consisting only of functions of the filtered velocity, and  $C_j$  is a vector of model coefficients. It is possible to compute the event–event correlation matrix on the fly using the velocity field from an ongoing simulation, thus eliminating the need of a theoretical model for all terms on the right-hand side of Eqs. (9)–(11). This dynamic procedure for computing correlations is extremely advantageous in complex turbulence, since it limits the necessary theoretical modeling to two-point, third-order and three-point, fourth-order velocity correlations for quadratic event estimates and to only the two-point, third-order velocity correlation when using a standard discretization for the quadratic part of the flux model.

A more fundamental reason for computing event–event correlations using a dynamic procedure rather than theoretical or DNS-based expressions is the following. When using theoretical or DNS-based expressions for the event–event correlations, the model coefficients are adjusted *a priori* to match the estimate–event correlations with the modeled-term–event correlations. On the other



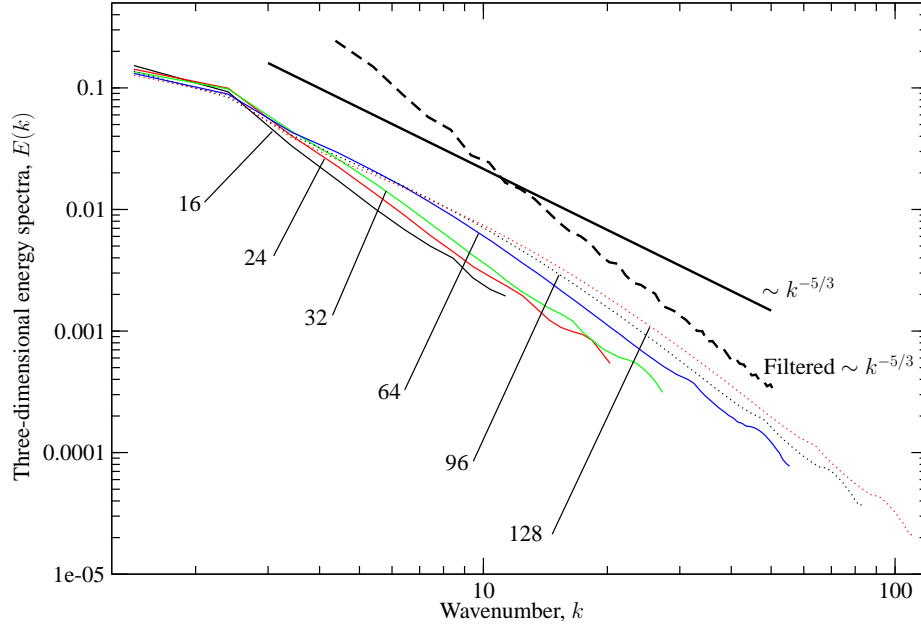


(a) Three-dimensional energy spectra,  $E(k)$

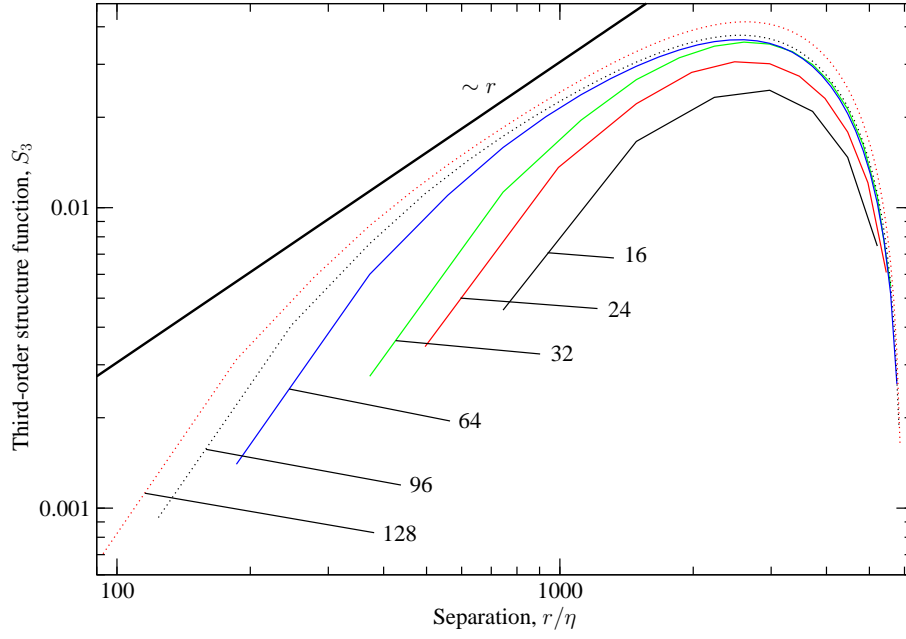


(b) Third-order structure function,  $S_3$

Figure 3: Filtered DNS statistics compared with theory-based OFVLES results for varying constraints on the quadratic part of the model.



(a) Three-dimensional energy spectra,  $E(k)$



(b) Third-order structure function,  $S_3$

Figure 4: Theoretical three-dimensional energy spectrum and third-order structure function compared with theory-based OFVLES results. Numbers in the legend represent grid points per direction.

hand, the dynamic procedure matches the *a posteriori* estimate–event correlations with the theoretical flux–event correlations, as the simulation is running. It can be argued that, if done correctly, the dynamic procedure does not contain any modeling error in the event–event correlations, since they are a true representation of the statistics in the simulation, not an *a priori* estimate.

On the other hand, the dynamic approach for collecting event–event correlations is limited by the sample size defined by the discretization and flow. Non-homogeneous grids and flows limit the application of space-averaging. The small sample size in these cases is an issue in other LES models, such as the dynamic Smagorinsky model, and no definite solution has been found to date.

#### 4.2.1 Issues in the Dynamic Computation of Correlations

Unlike DNS- and theory-based OFVLES models, it is not possible to use all the DOF of the quadratic part of the flux model for the optimization of the variance of the model. After long simulation times, the results from the dynamic models exhibit inaccurate large-scale behavior. It is expected that fully converged velocity correlations, such as those used in DNS- and theory-based simulations, yield optimal models that are compatible with the large-scale dynamics, but poorly converged correlations, such as those used during the dynamic procedure, do not. Adding to the issue, time-averaging of the three-point, third-order correlations is exceedingly difficult because of long-time scales associated with the production-range (small-wavenumber) velocity. These long-time scales lead to slow convergence of the dynamically computed correlations and of the resulting optimal model. It is, therefore, important to constrain the large-scale behavior of the OFVLES dynamic models while the simulation is underway. To constrain the OFVLES models properly, it is important to realize that the large-scale dynamics of the OFVLES model should be similar to the standard model derived from order-of-accuracy considerations.

The use of  $1 \times 1 \times 2$  stencils for the linear part is also essential for the stability of dynamic OFVLES convective-flux models, especially the  $M_{uw}$  flux model. When using larger stencils for the linear part, the linear part of the  $M_{uw}$  model becomes numerically (linearly) unstable. Note that, as verified previously<sup>8,19</sup> and in 4.1.2, in the cases of DNS- and theory-based OFVLES models, the  $1 \times 1 \times 2$  stencil was optimal for the linear part of the models. The addition of extra dependencies on further removed velocity events did not increase the accuracy of the models, *a priori* or *a posteriori*, even when accurately represented. The addition of these events to the dynamic models not only failed to increase the accuracy of the model, as was verified for the  $M_{ww}$  flux, but caused the model to become unstable, as noted for the  $M_{uw}$  flux.

The more pressing issue in the OFVLES of bulk flow turbulence is the accurate computation of the energy dissipation  $\epsilon$ . In the case where the quadratic part of the model is constrained to the standard discretization, the only quantity that must be computed using Kolmogorov theory is  $\langle M_{ij} w_i^- \rangle$ , which is a linear function of  $\epsilon$ , as given by Eq. (30). For isotropic turbulence, the average dissipation can be computed by using the two-point correlation, Eq. (29), but for the case of a generic turbulence the problem has not been solved.

### 4.2.2 Results for Dynamic OFVLES

The results obtained with the dynamic OFVLES models differ from the DNS- and theory-based results in a fundamental manner. In both the DNS- and theory-based cases, the values of the dissipation and velocity variance from the DNS simulations were used to compute the OFVLES models before the simulation was initiated (implicitly in the DNS-based case and explicitly in the theory-based case). For dynamic OFVLES, these values must be computed on-the-fly since it is necessary that the correlation values computed dynamically and theoretically be consistent. Therefore, at every time step, the dissipation is approximated using the two-point correlation, Eq. (29), and the velocity variance is approximated by the resolved velocity variance. These approximations are then inserted into the expressions for the left-hand side of Eqs. (9)–(10).

The statistics obtained in simulations using the dynamic OFVLES model for the S2 and S4 stencil are shown in Figs. 5 and 6. The number of DOF available for the optimization of the quadratic part was varied for each of the stencils. Note that one DOF is for the  $M_{uw}$  flux, while the remaining DOF are for the  $M_{ww}$  flux.

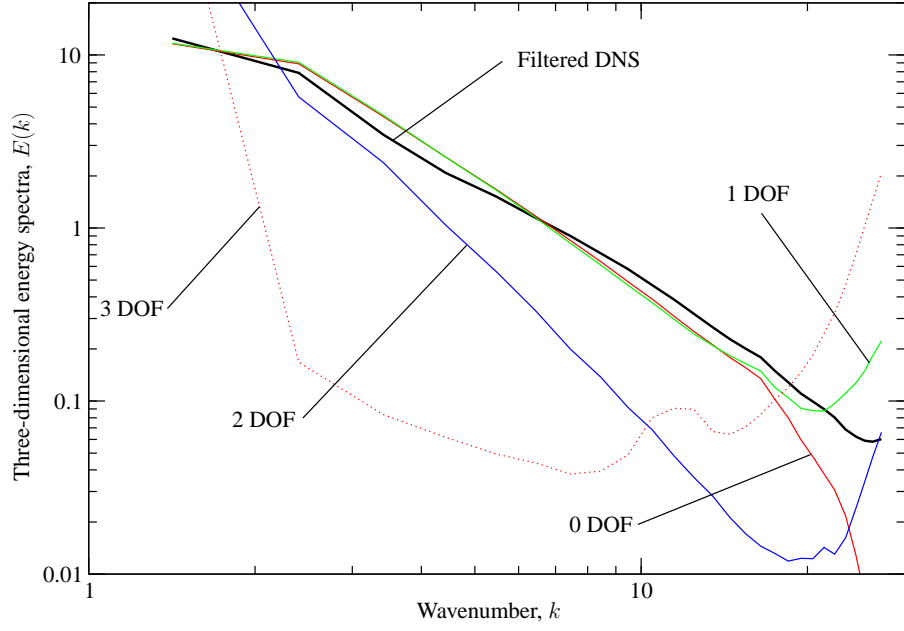
It is clear, for both the S2 and the S4 stencils, that unconstrained dynamic OFVLES models are not accurate for the energy spectra throughout the wavenumber range. The only case where the unconstrained model produced an accurate energy spectrum, the S4 stencil with 3 DOF, displays the worst results for the third-order structure function. The best results for both the energy spectrum and third-order structure functions were obtained with either a single DOF for optimization of the quadratic part or the standard discretization, as for the theory-based OFVLES models.

In Figs. 7 and 8, the dynamic OFVLES statistics are compared with those of DNS- and theory-based OFVLES models and the dynamic Smagorinsky model, where all models use the S4 stencil. In Fig. 7, all models use the standard discretization for the quadratic part of the convective flux, while in Fig. 8 the OFVLES models use an optimal quadratic part with one DOF. Also, it is important to remember that both the theory-based and the dynamic OFVLES models do not contain viscous terms, while the DNS-based and dynamic Smagorinsky simulation do. The lack of viscous terms for the OFVLES models could account for the small differences between the models at the large wavenumbers and smallest scales.

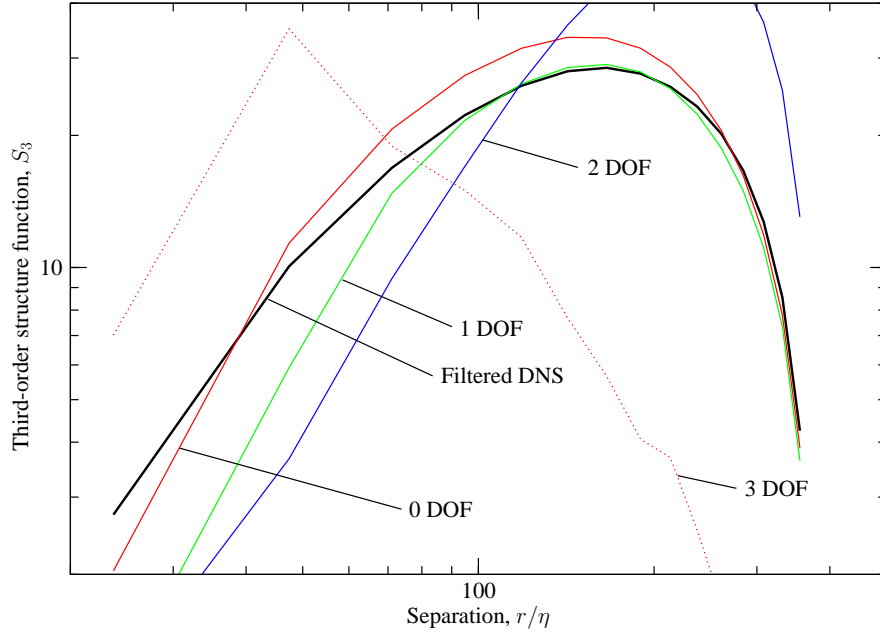
It is difficult to determine whether the use of the standard discretization or the optimal model with a single DOF is more accurate. While the third-order structure function results for standard discretization seem to be more accurate than those for the models with a one DOF optimal quadratic part, the opposite is true for the energy spectrum. However, these results show that the accuracy of the dynamic OFVLES model is comparable with that of other approaches, with the only noticeable discrepancy being the results for the third-order structure function at the smallest separation.

## 4.3 Application: Simulation of a Temporally-Evolving Shear Layer

In the previous section, the optimal finite-volume LES model was applied only to isotropic turbulence. To evaluate OFVLES in a more complex flow, the simulation of a temporally-evolving shear layer is pursued here. The shear layer is appropriate as the next test case given that the flow

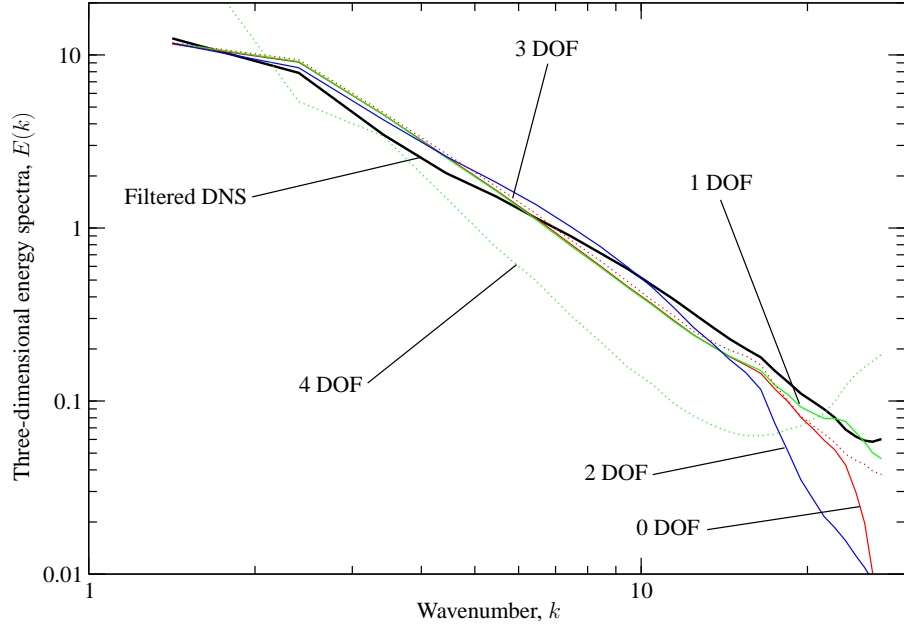


(a) Three-dimensional energy spectra,  $E(k)$

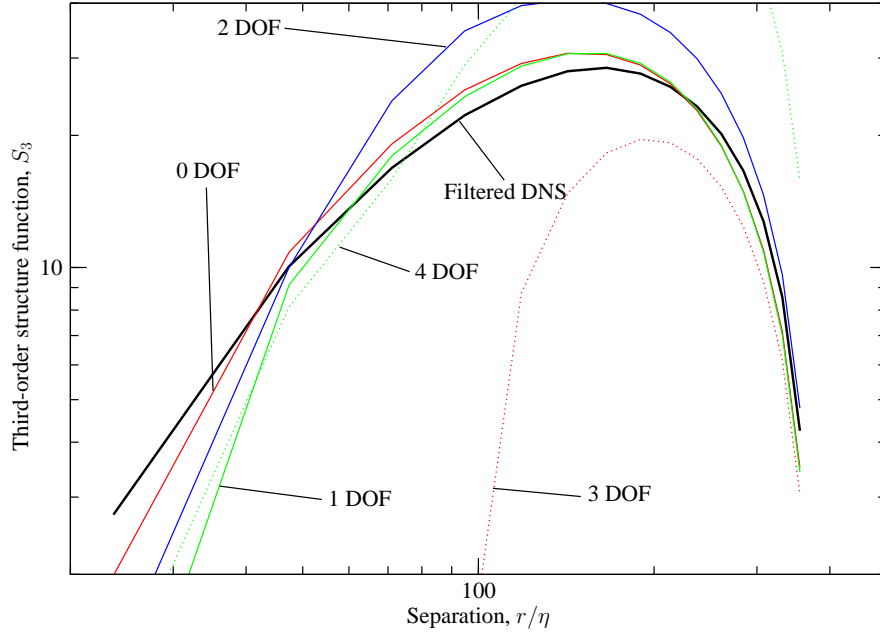


(b) Third-order structure function,  $S_3$

Figure 5: Filtered DNS statistics compared with dynamic OFVLES results. The quadratic parts of the OFVLES models are constrained to differing degrees. S2 stencil.

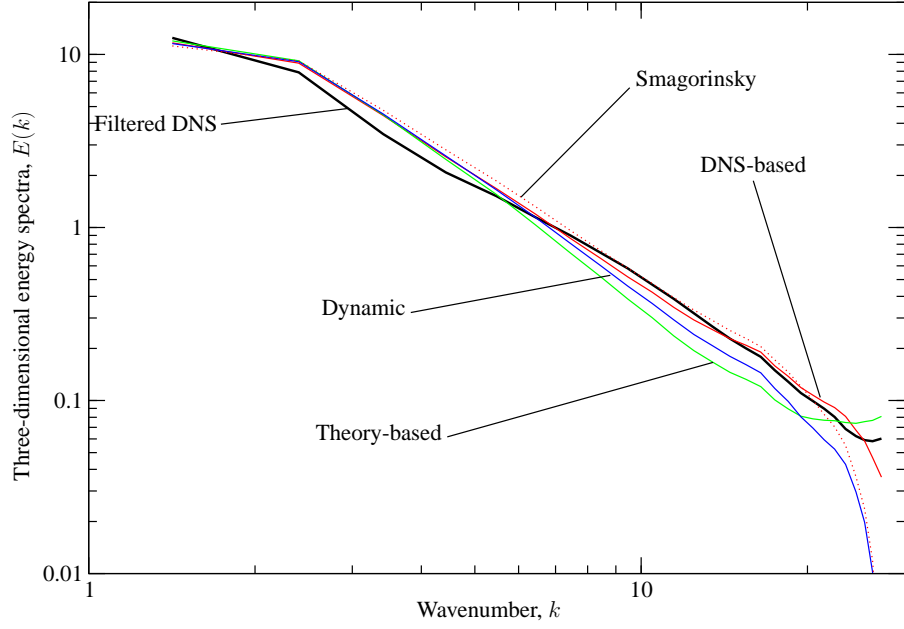


(a) Three-dimensional energy spectra,  $E(k)$

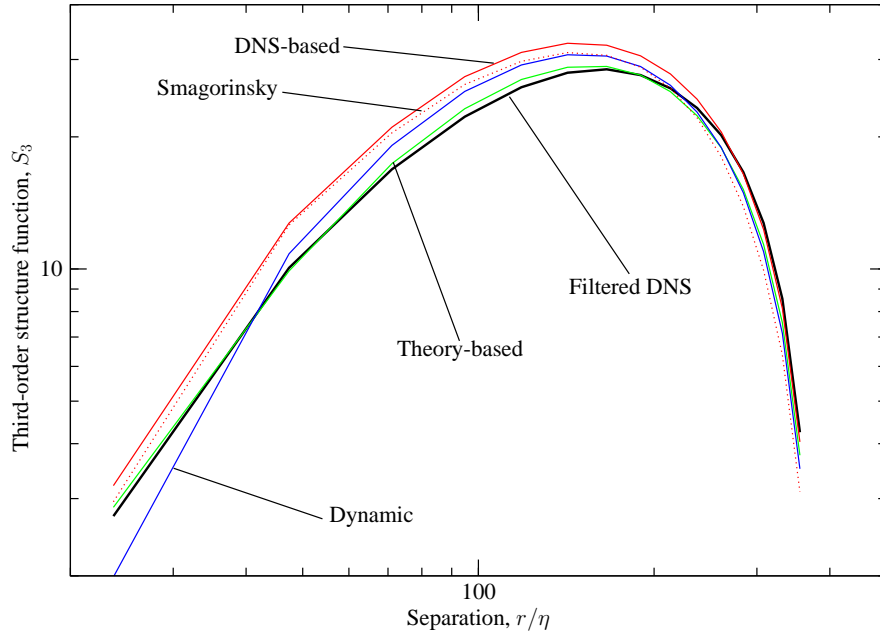


(b) Third-order structure function,  $S_3$

Figure 6: Filtered DNS statistics compared with dynamic OFVLES results. The quadratic parts of the OFVLES model are constrained to differing degrees. S4 stencil.

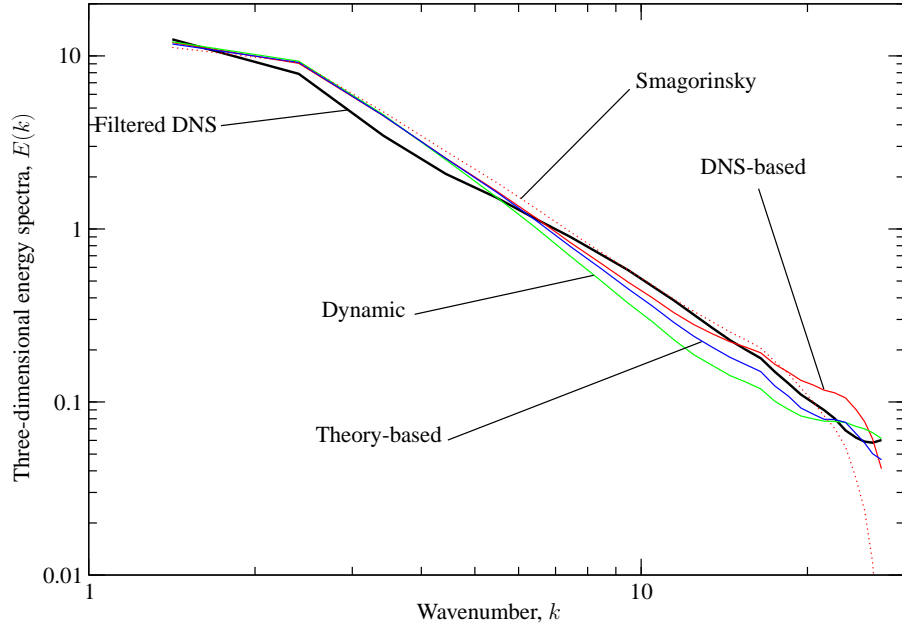


(a) Three-dimensional energy spectra,  $E(k)$

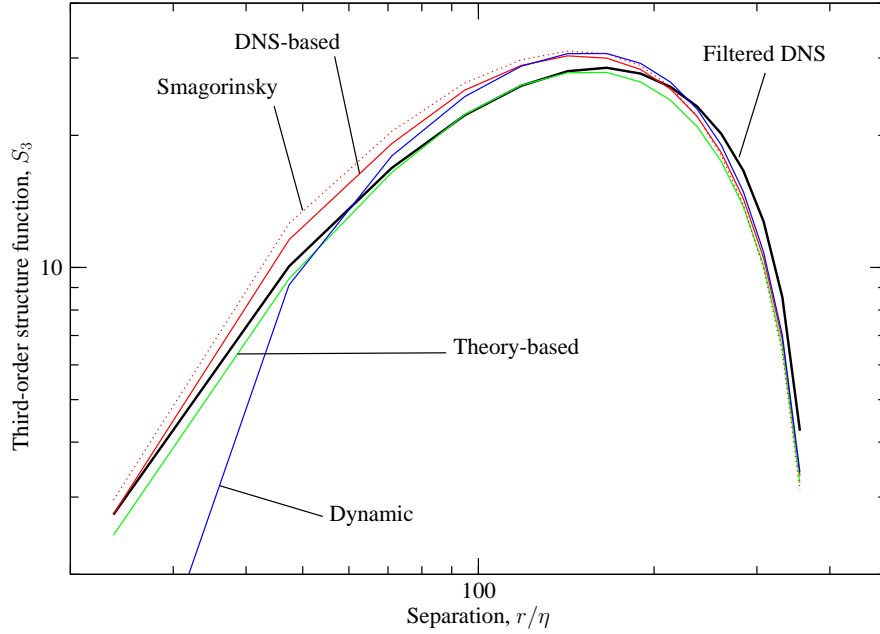


(b) Third-order structure function,  $S_3$

Figure 7: Filtered DNS statistics compared with theory-based, DNS-based and dynamic OFVLES and dynamic Smagorinsky results. All models are constrained to using Taylor-series derived approximations for the quadratic part of the convective flux. S4 stencil.



(a) Three-dimensional energy spectra,  $E(k)$



(b) Third-order structure function,  $S_3$

Figure 8: Filtered DNS statistics compared with theory-based, DNS-based and dynamic OFVLES and dynamic Smagorinsky results. OFVLES models are constrained to using 1 DOF for the quadratic part of the convective flux. Dynamic Smagorinsky model uses the standard discretization for the quadratic part. S4 stencil.



physics are more complex without the necessity of modeling near-wall turbulence. One can expect that the results obtained using the dynamic OFVLES model in the simulation of a shear layer is representative of the performance of OFVLES models away from the wall.

#### 4.3.1 Issues of Dynamic OFVLES for the Shear Layer

Compared with the isotropic turbulence case, an important difference in the formulation of the dynamic OFVLES model in the shear layer is the existence of a mean velocity. For shear-layer turbulence, the estimation equations for the constant and linear term must be rewritten as

$$\langle M_{ij} \rangle = A_{ij} + L_{ij}^+ \langle w_i^+ \rangle + L_{ij}^- \langle w_i^- \rangle + \langle \Psi_{ij} \rangle, \quad (51)$$

$$\langle M_{ij} w_i^- \rangle = A_{ij} \langle w_i^- \rangle + L_{ij}^+ \langle w_i^+ w_i^- \rangle + L_{ij}^- \langle w_i^- w_i^- \rangle + \langle \Psi_{ij} w_i^- \rangle, \quad (52)$$

$$\langle M_{ij} w_i^+ \rangle = A_{ij} \langle w_i^+ \rangle + L_{ij}^+ \langle w_i^+ w_i^+ \rangle + L_{ij}^- \langle w_i^- w_i^+ \rangle + \langle \Psi_{ij} w_i^+ \rangle, \quad (53)$$

where

$$\Psi_{ij} = \sum_{\alpha, \beta} Q_{ij} w_i^\alpha w_j^\beta \quad (54)$$

is used to simplify the notation.

For the current simulation, the linear coefficients are constrained to be of equal value but opposite sign,  $L_{ij}^+ = -L_{ij}^-$ , leading to a purely dissipative model with no dispersion. With this simplification, Eqs. (51)–(53) become

$$\langle M_{ij} \rangle = A_{ij} + L_{ij} \langle w_i^+ - w_i^- \rangle + \langle \Psi_{ij} \rangle, \quad (55)$$

$$\langle M_{ij} (w_i^+ - w_i^-) \rangle = A_{ij} \langle w_i^+ - w_i^- \rangle + L_{ij} \langle (w_i^+ - w_i^-)^2 \rangle + \langle \Psi_{ij} (w_i^+ - w_i^-) \rangle. \quad (56)$$

The OFVLES flux models on faces in the homogeneous directions, that is, with face normals pointing in the  $x$  and  $z$  directions, may be simplified by noting that  $\langle w_i^+ \rangle = \langle w_i^- \rangle$ , decoupling Eq. (55) from Eq. (56). Also note that the value of  $A_{ij}$  is irrelevant for the momentum computation, since it is constant for opposing faces in the homogeneous directions of the shear flow. Therefore, for the  $x$  and  $z$  directions, the equation for the linear term of the dynamic OFVLES model is

$$\langle M_{ij} (w_i^+ - w_i^-) \rangle = L_{ij} \langle (w_i^+ - w_i^-)^2 \rangle + \langle \Psi_{ij} (w_i^+ - w_i^-) \rangle, \quad (57)$$

where the solution for  $L_{ij}$  is

$$L_{ij} = \frac{\langle M_{ij} (w_i^+ - w_i^-) \rangle - \langle \Psi_{ij} (w_i^+ - w_i^-) \rangle}{\langle (w_i^+ - w_i^-)^2 \rangle}. \quad (58)$$

Note that, since in the homogeneous directions the mean velocities  $\langle w_i^+ \rangle$  and  $\langle w_i^- \rangle$  are identical, the equation for the OFVLES model is identical to the one used in homogeneous turbulence.

The estimation of the OFVLES flux models for faces in the  $y$  direction is considerably more complicated due to two factors. First, the value of the constant  $A_{ij}$  does contribute to the filtered

evolution equation, since flux models on opposing faces in the  $y$  direction will have different values for the constant coefficient. Second, the equations for the linear and constant parts of the flux model are coupled, since  $\langle w_i^+ \rangle \neq \langle w_i^- \rangle$ .

The solution for the OFVLES model fluxes in the  $y$  direction is given by

$$A_{ij} = \langle M_{ij} \rangle - \langle \Psi_{ij} \rangle - L_{ij} \langle (w_i^+ - w_i^-) \rangle, \quad (59)$$

$$L_{ij} = \frac{\langle (M_{ij} - \langle M_{ij} \rangle) (w_i^+ - w_i^-) \rangle - \langle (\Psi_{ij} - \langle \Psi_{ij} \rangle) (w_i^+ - w_i^-) \rangle}{\langle (w_i^+ - w_i^-)^2 \rangle - \langle w_i^+ - w_i^- \rangle^2}. \quad (60)$$

While the dynamically computed terms in Eqs. (58) and (59)–(60) are easily solved for during the simulation, the same is not true for the correlations depending on  $M$ , which are computed via the Kolmogorov relations. The correlations developed using Kolmogorov's inertial-range theory do not account for the existence of a mean velocity, being correct only for the correlations of the velocity fluctuations. However, as is shown in Zandonade<sup>19</sup>, if small-scale isotropy of the velocity correlations is a valid approximation in shear flow, the theoretical expressions for these correlations, developed from Kolmogorov's inertial range theory, may still be used.

To compute the third-order, three-point velocity correlations using the theoretical expressions developed above, it is necessary to estimate the dissipation at the face where the flux is computed. For the shear-layer simulation, the dissipation is approximated using the scaling equation

$$\langle (w_i^+ - w_i^-) (w_j^+ - w_j^-) \rangle = C_{ij}^\epsilon \epsilon^{2/3}, \quad (61)$$

where the scaling coefficient  $C^\epsilon$  is computed using the Kolmogorov relation for the second-order structure function

$$C_{ij}^\epsilon = \frac{C_1}{3V^2} \left( \int_V \int_V |\mathbf{x}^+ - \mathbf{x}^-|^{-4/3} \left( (\mathbf{x}^+ - \mathbf{x}^-)_i (\mathbf{x}^+ - \mathbf{x}^-)_j - 4|\mathbf{x}^+ - \mathbf{x}^-|^2 \delta_{ij} \right) d\mathbf{x}^- d\mathbf{x}^+ \right. \\ \left. + \int_{V^+} \int_{V^-} |\mathbf{x}^+ - \mathbf{x}^-|^{-4/3} \left( (\mathbf{x}^+ - \mathbf{x}^-)_i (\mathbf{x}^+ - \mathbf{x}^-)_j - 4|\mathbf{x}^+ - \mathbf{x}^-|^2 \delta_{ij} \right) d\mathbf{x}^- d\mathbf{x}^+ \right). \quad (62)$$

Therefore, the dissipation is computed using the relation

$$\epsilon = \left( \frac{\langle (w_i^+ - w_i^-) (w_j^+ - w_j^-) \rangle}{C_{ij}^\epsilon} \right)^{3/2}. \quad (63)$$

The dissipation is computed for every face using the appropriate velocity for a given grid and then averaged in each  $xz$  plane.

### 4.3.2 Details of the Simulation

The geometry for the simulation of the shear layer is displayed in Fig. 9, where the  $x$  and  $z$  directions are periodic. The initial condition is imposed by setting the plane-averaged mean velocity in the  $x$  direction to

$$\langle u \rangle_{xz}(y) = \Delta U \operatorname{erf} \left( \frac{y}{\delta} \right), \quad (64)$$

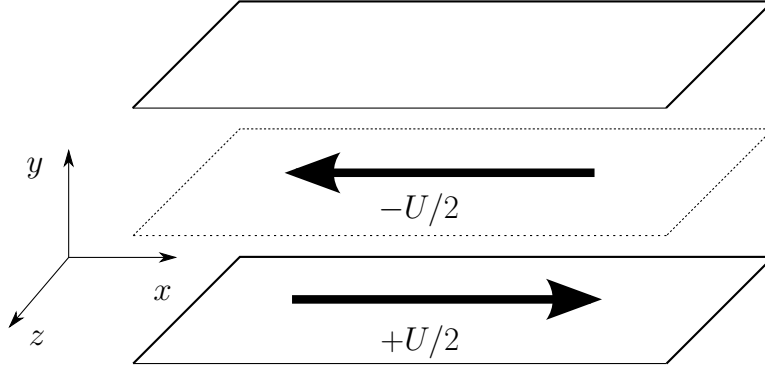


Figure 9: Geometry of the shear layer simulation.

where  $\delta$  is a parameter setting the initial thickness of the shear layer,  $\Delta U$  is the velocity difference across the shear layer and the subscript on the averaging operator defines the plane over which the averaging takes place. The velocity fluctuations are computed with a random number generator using a normal distribution and variance given by

$$\sigma^2(y) = q^2 \exp\left(-\frac{y^2}{\delta}\right), \quad (65)$$

where  $q^2$  is the velocity variance at the origin of the  $y$  coordinate system.

The filtered evolution equation is advanced in time using the standard fourth-order Runge–Kutta scheme. The dynamic OFVLES model is used for the convective fluxes, with a standard second-order divergence-form finite-volume model for the quadratic terms. The linear part of the OFVLES model depends on the two velocity events neighboring the flux face, a stencil shown to be optimal in previous chapters. The correlations needed for the OFVLES model are averaged in each  $xz$  plane, and are computed at every step of the Runge–Kutta scheme. The viscous fluxes are not computed in this simulation, so that the Reynolds number of the simulated flow is infinite.

Values of pressure are determined using the classical fractional step method of Chorin<sup>20</sup>. The solution of the filtered evolution equation is a three-step process. First, the momentum equation is solved without the pressure term, yielding a tentative solution for the velocity at a time  $t + \delta t$ . Second, a Poisson equation for pressure is solved that guarantees that the velocity at the end of the iteration will be solenoidal. Finally, the pressure gradient is subtracted from the tentative velocity to yield the final solenoidal velocity field:

$$w_i^* = \Delta t \left( \Delta_j M_{ij} + \frac{1}{Re} \frac{\partial^2 w_i^n}{\partial x_j \partial x_j} \right), \quad (66)$$

$$\Delta t \frac{\partial^2 p}{\partial x_i \partial x_i} = \frac{\partial w_i^*}{\partial x_i} = H, \quad (67)$$

$$w_i^{n+1} = w_i^* - \Delta t \frac{\partial p}{\partial x_i}, \quad (68)$$

where  $H$  is the divergence of the tentative velocity solution. Note that Eq. (67) is simply the divergence of Eq. (68), where  $\partial w_i^{n+1} / \partial x_i$  is set to zero.

The periodicity of the  $x$  and  $z$  directions allows the use of the Fourier transform to reduce the cost of solving the Poisson equation. Fourier transforming Eq. (67) in the  $x$  and  $z$  directions yields:

$$\Delta t \left( - (k_x^2 + k_z^2) + \frac{\partial}{\partial y^2} \right) \hat{p} = \hat{H}. \quad (69)$$

The second derivative of pressure in the  $y$  direction can be computed by a second-order finite-difference method:

$$\frac{p(\mathbf{x} + \Delta_y)}{\Delta_y^2} - \left( \frac{2}{\Delta_y^2} + k_x^2 + k_z^2 \right) p(\mathbf{x}) + \frac{p(\mathbf{x} - \Delta_y)}{\Delta_y^2} = \frac{\hat{H}}{\Delta t}, \quad (70)$$

where  $\Delta_y$  is the grid separation in the  $y$  direction. Equation (70) is a tridiagonal system of equations that is solved using the tridiagonal matrix algorithm (TDMA) for each  $k_x$  and  $k_z$  wavenumber, except for the  $(0, 0)$  mode, which is set to zero. The boundary conditions in the  $y$  direction are Neumann, where the derivative of pressure in the  $y$  direction is set to 0.

Also note that the  $k_x$  and  $k_z$  wavenumbers appearing in Eq. (70) are substituted by effective wavenumbers for the second-order-accurate first-derivative finite-difference operator. With this substitution, the current scheme is equivalent to a standard second-order finite-difference discretization of Eq. (67).

Periodic boundary conditions for the velocity are imposed at the  $x$  and  $z$  boundaries. For the boundaries in the  $y$  direction, irrotational flow is imposed. The vanishing vorticity at the boundary is imposed by using the  $y$  derivative of the continuity condition:

$$\frac{\partial^2 u}{\partial x \partial y} + \frac{\partial^2 v}{\partial y^2} + \frac{\partial^2 w}{\partial z \partial y} = 0. \quad (71)$$

The first and third terms in Eq. (71) can be expressed as derivatives of  $v$  given that the  $x$  and  $z$  components of vorticity are zero:

$$\omega_x = 0 \rightarrow \frac{\partial w}{\partial y} = \frac{\partial v}{\partial z}, \quad (72)$$

$$\omega_z = 0 \rightarrow \frac{\partial u}{\partial y} = \frac{\partial v}{\partial x}, \quad (73)$$

yielding a Poisson equation for  $v$ :

$$\nabla^2 v = 0. \quad (74)$$

The periodicity of the domain allows the Fourier transformation of Eq. (74) in the  $x$  and  $z$  directions:

$$- (k_x^2 + k_z^2) \hat{v}(y, k_x, k_z) + \frac{\partial \hat{v}(y, k_x, k_z)}{\partial y^2} = 0. \quad (75)$$

Substituting a second-order finite-difference approximation for the derivative in Eq. (75) yields a difference equation for the discrete velocity:

$$\frac{\hat{v}_{j+1}(k_x, k_z) - (2 + k^2) \hat{v}_j(k_x, k_z) + \hat{v}_{j-1}(k_x, k_z)}{\Delta_y^2} = 0, \quad (76)$$

where  $k^2 = k_x^2 + k_z^2$  and the subscripts containing  $j$  are the  $y$  indices of the grid points.

The difference equation (76) may be solved by noting that the solution must be of the form:

$$\hat{v}_j = r^j. \quad (77)$$

Substituting Eq. (77) into Eq. (76) yields:

$$\hat{v}_j(k_x, k_z) = \left( 1 + \frac{k^2 \Delta_y^2}{2} \pm \sqrt{k^2 \Delta_y} \sqrt{1 + \frac{k^2 \Delta_y^2}{4}} \right)^j \hat{v}_0(k_x, k_z), \quad (78)$$

where  $\hat{v}_0(k_x, k_z)$  is the Fourier coefficient for an interior  $xz$  plane. To guarantee that  $\hat{v}$  vanishes as  $j \rightarrow \infty$ ,  $\hat{v}_j(k_x, k_z)$  is given by

$$\hat{v}_j(k_x, k_z) = \left( 1 + \frac{k^2 \Delta_y^2}{2} - \sqrt{k^2 \Delta_y} \sqrt{1 + \frac{k^2 \Delta_y^2}{4}} \right)^j \hat{v}_0(k_x, k_z). \quad (79)$$

With  $v$  at the boundary set by Eq. (79), the corresponding boundary conditions for  $u$  and  $w$  may be found by using Eqs. (72) and (73) with first-order finite-difference approximations for the derivatives.

### 4.3.3 Results for the Shear Layer Simulation

The temporally-evolving shear layer displays self-similar growth while the growth rate is linear. In the linear-growth-rate regime, quantities should be scaled by the velocity difference  $\Delta U$  and the momentum thickness

$$\delta_m = \int_{-\infty}^{\infty} \left( \frac{1}{4} - \left( \frac{\langle u \rangle_{xz}}{\Delta U} \right)^2 \right) dy. \quad (80)$$

The initial momentum thickness is denoted by  $\delta_0$ . The appropriately scaled time variable is

$$\tau = \frac{t \Delta U}{\delta_0}. \quad (81)$$

The results in this section were obtained using the parameters in Table 3. In that same table, the grid parameters for the OFVLES are compared with those used in the DNS by Rogers & Moser<sup>21</sup>. This DNS will be used as the benchmark when comparing the results from the OFVLES.

The growth of the shear layer during the simulation is displayed in Fig. 10, while the instantaneous growth rate is shown in Fig. 11. The growth rate is approximately linear in the range  $\tau = 200 - 500$ . During this time period the growth of the shear layer will be considered self-similar and the statistics will be collected. Note that the growth rate is slightly higher than the averaged value for the self-similar portion of the DNS. The offset between the start of self-similar growth in the DNS and in the LES is due to the use of different initial conditions in each of the simulations. In the

Table 3: Grid parameters for OFVLES and DNS shear layer simulations.

Parameter	OFVLES			DNS		
	$x$	$y$	$z$	$x$	$y$	$z$
Grid points (or modes)	128	128	32	512	210	192
Size of domain	$125\delta_0$	$80\delta_0$	$31.25\delta_0$	$125\delta_0$	$\infty$	$31.25\delta_0$

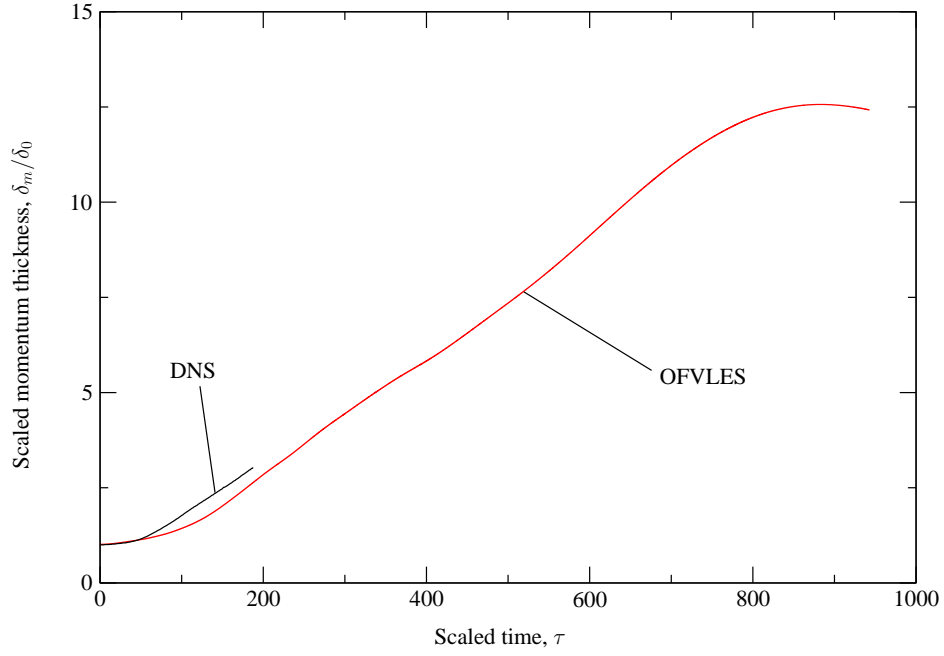


Figure 10: Growth of shear layer: dynamic OFVLES compared with DNS.

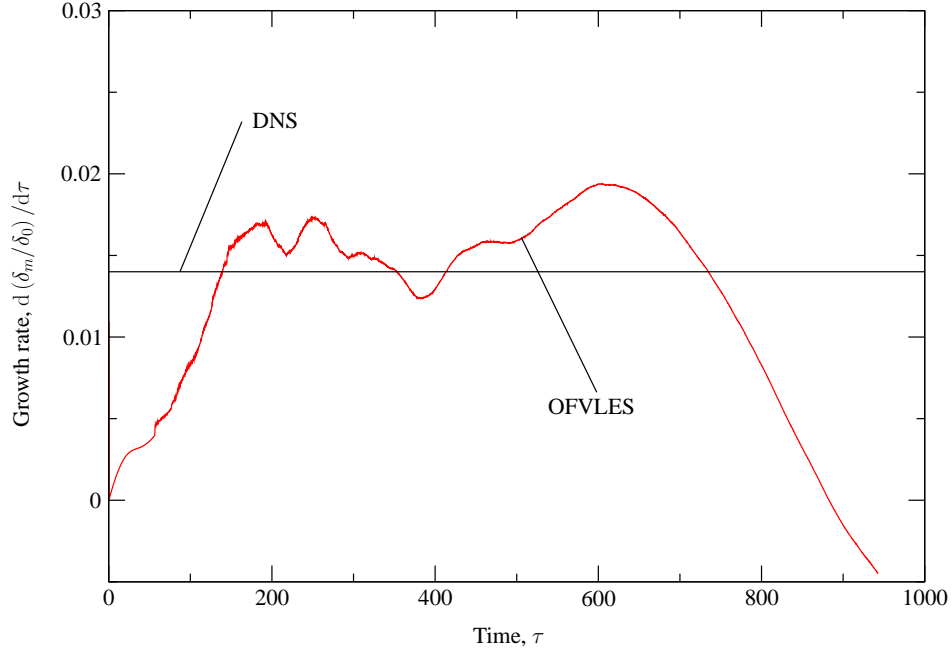


Figure 11: Growth rate of shear layer: instantaneous value for dynamic OFVLES compared with averaged value for self-similar portion of DNS.

DNS, turbulence profiles from a boundary-layer DNS were used to start the simulation, while in the LES a synthetic field (described in Section 4.3.2) was used as the initial field.

The large-scale structure of the simulated shear layer at time  $\tau = 300$  may be visualized in Figs. 12 and 13, which plot the instantaneous vorticity magnitude and velocity vectors in an  $xy$  plane. The dynamic OFVLES results display large-scale features similar to the ones depicted in the spanwise vorticity contour plots by Rogers & Moser<sup>21</sup> for velocity fields in the linear growth regime. The accurate description of the large-scale structures is expected, given that the standard discretization scheme used as the quadratic part of the OFVLES model is accurate for the large scales and the linear part of the model is most important for scales close to the filter scale.

The profiles for the mean velocity and Reynolds stresses, averaged during the self-similar portion of the simulation, are shown in Figs. 14-18. The results obtained with the OFVLES model are comparable to those obtained with the DNS, except for the  $\langle vv \rangle$  Reynolds stress, which was higher in the OFVLES results. This discrepancy may be due to the approximation of the mean flux used to compute the flux models for the faces with normals pointing in the  $y$  direction. These results are evidence of the robustness of the OFVLES model in the case of bulk-flow turbulence, since accurate results were obtained even though approximate expressions were used for computing the dissipation and the mean flux.

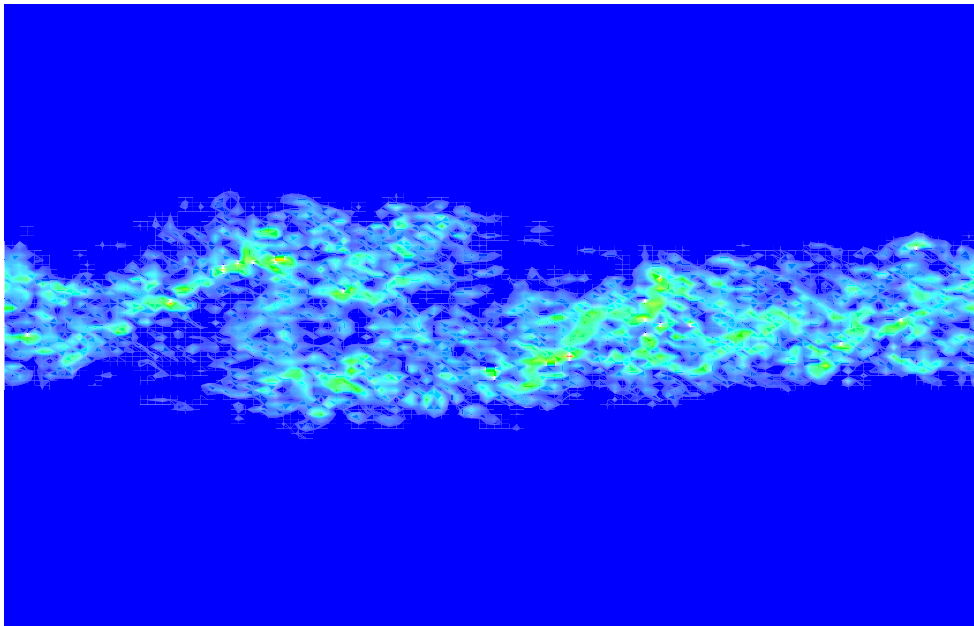


Figure 12: Shear layer visualization: vorticity magnitude in an  $xy$  plane.



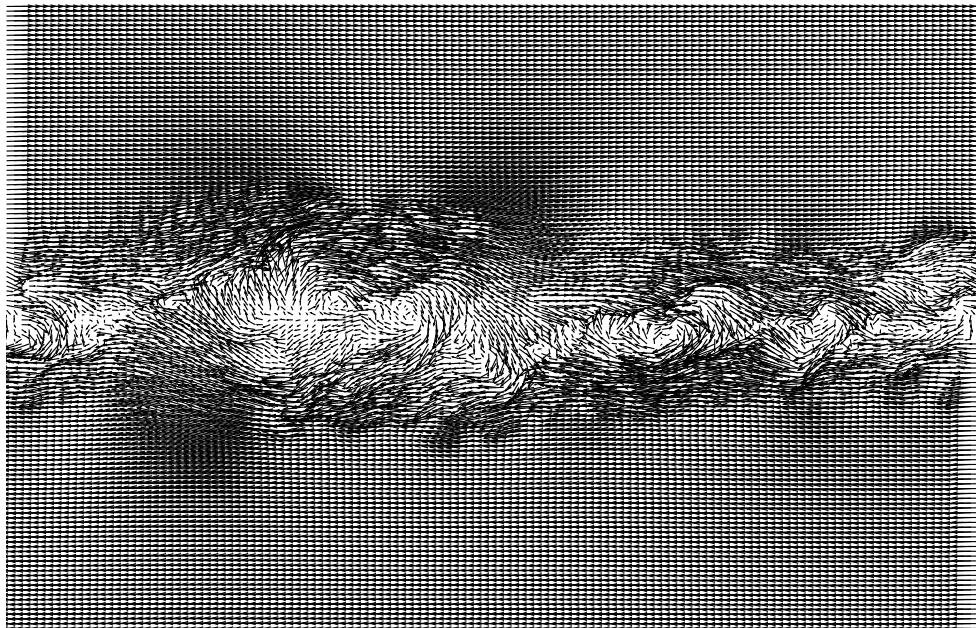


Figure 13: Shear layer visualization: velocity vectors in an  $xy$  plane.

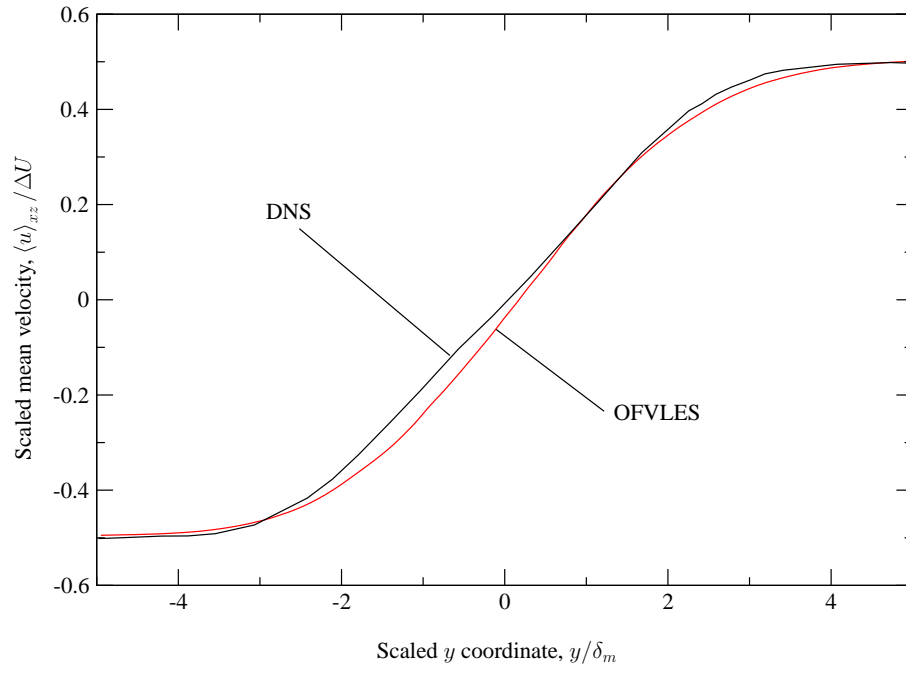


Figure 14: Mean velocity profile for shear layer: dynamic OFVLES compared with DNS.

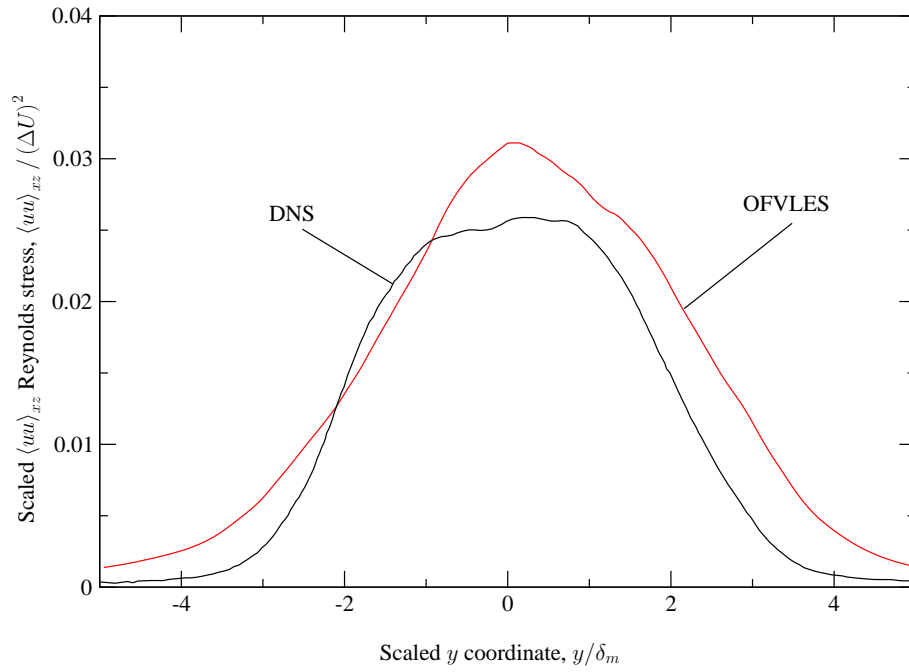


Figure 15: Mean  $\langle uu \rangle$  Reynolds stress for shear layer: dynamic OFVLES compared with DNS.

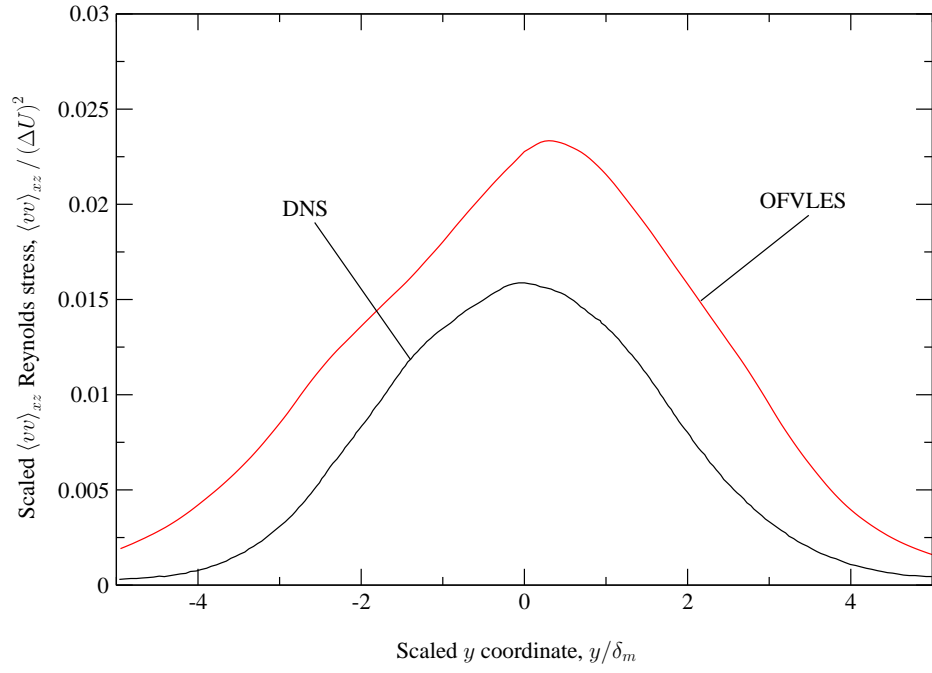


Figure 16: Mean  $\langle vv \rangle$  Reynolds stress for shear layer: dynamic OFVLES compared with DNS.

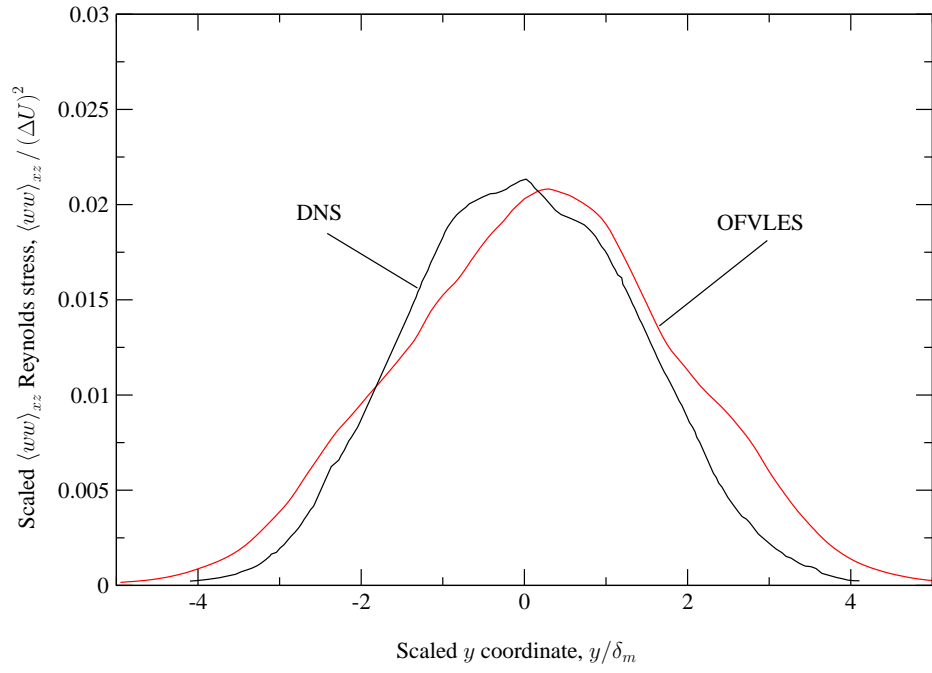


Figure 17: Mean  $\langle ww \rangle$  Reynolds stress for shear layer: dynamic OFVLES compared with DNS.

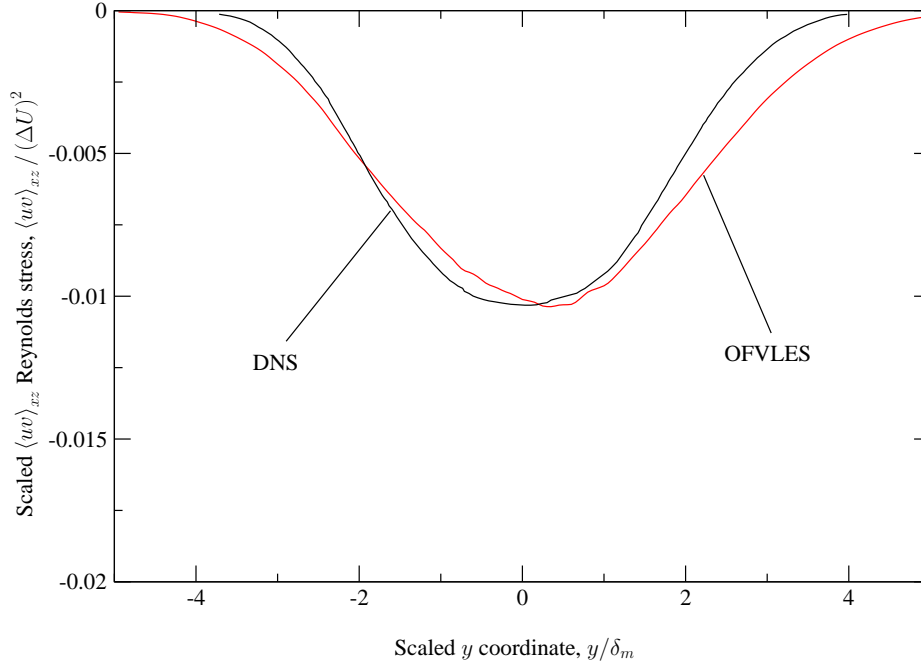


Figure 18: Mean  $\langle uv \rangle$  Reynolds stress for shear layer: dynamic OFVLES compared with DNS.

## 4.4 Conclusions

The validity of the stochastic estimate as an approximation to the ideal LES was previously tested<sup>8</sup> by using DNS data for the necessary correlations. The OFVLES models developed from the DNS data were shown to be more accurate and less expensive than current LES models such as the dynamic Smagorinsky model, even if much more limited in their applicability due to the reliance on the DNS-based velocity correlations. The important properties of OFVLES models for isotropic turbulence were uncovered in this phase of the research. It was determined that the optimal stencil of velocity events in the linear part of the stencil was that of the two events closest to the face where the flux is modeled. Larger stencils led to models which had almost identical *a priori* and *a posteriori* behavior as the smallest stencil, at a much greater cost. Another important feature of OFVLES models is the fact that the accuracy of the quadratic part of the model computed through the optimal procedure is similar to that of a standard numerical discretization for the convective flux. Application of these two constraints on OFVLES models lead to inexpensive, yet accurate LES models for isotropic flow.

The second stage of the development of OFVLES models was concerned with removing the dependence of the models on DNS data. To this end, it was necessary to develop alternate methods to compute the velocity correlations appearing in the estimation equations. Theoretical models for the velocity correlations are derived from Kolmogorov's inertial-range expressions. A purely theoretical model has not been developed at this time, due to one velocity correlation, the three-point, third-order correlation, remaining unclosed. Also, a dynamic approach for computing resolved velocity correlations is developed to substitute DNS data, including the three-point, third-order velocity correlation. Results from both the theory and dynamic approaches for determining velocity correlations are quite encouraging, being only slightly less accurate than the DNS-derived models.

Note that the theory used to determine the velocity correlations is valid only in the limit of an infinite Reynolds number and the DNS simulations used as a benchmark were at a low Reynolds numbers. The OFVLES models based on dynamic and theory-based correlations do not depend on any DNS data, and are the first optimal models to display this characteristic.

The application of the OFVLES models to a more complex flow, the temporally-growing shear layer, was also successful. The results obtained for mean velocity and Reynolds stresses in the LES are comparable to the DNS results of Rogers & Moser<sup>21</sup>, while using a low-order-accurate numerical method and a mesh sixteen times coarser in the  $x$ - $z$  plane than the DNS. These results are important because they are an indication of the performance of OFVLES models in bulk-flow turbulence.

Although OFVLES has been successfully applied in the simulation of isotropic and shear-flow turbulence, several issues remain to be resolved before these models can meet widespread use:

- **Dissipation:** To evaluate the flux–velocity correlations that are derived from theory, it is necessary to compute the averaged dissipation at the face where the flux is modeled. In isotropic turbulence many different approaches exist for computing the dissipation, based mainly on Kolmogorov’s expressions for the second- and third-order structure functions; the second-order function was used in this work. On the other hand, in more complex flows no standard procedure for computing dissipation has been developed. For these flows, an accurate method for computing the dissipation is necessary in order for the OFVLES methods to remain useful. The optimal model simply ensures the correct distribution of the dissipation among the different fluxes and, therefore, if the dissipation is not computed accurately, the optimal model itself will be in error.
- **Averaging for the dynamic procedure:** In the flows analyzed in this dissertation, the existence of homogeneous directions in the flow eased the task of averaging the dynamically gathered correlations. In more complex grid geometries—note that even a simple flow geometry with a complex grid arrangement would suffer from this issue—it is not clear how to proceed with the averaging of the velocity correlations. While spatial averaging may be used in the case of isotropic turbulence and other flows that have the appropriate spatial symmetries (such as plane-by-plane averaging for plane channel flow), for complex geometries some kind of time averaging must be employed. The time average used for computing the correlations will affect the evolution of the LES, and finding the correct procedure for averaging is not trivial. The issue is similar to the averaging of the dynamic Smagorinsky coefficient, so it may be possible to use many of the same tools in the case of OFVLES.
- **Three-point, third-order velocity correlation:** While the dynamic approach would encounter problems in flows with no homogeneous directions due to the necessity of averaging the correlations, a purely theoretical model would not suffer from this issue. In fact, the only further work involved when applying the theoretical model to a completely unstructured grid is extra bookkeeping. A model of the three-point third-order correlation, which would enable such a theoretical model, is discussed in section 5.
- **Models for near-wall turbulence:** While all LES models lack appropriate wall-modeling, the problem in OFVLES is focused on developing appropriate velocity correlations near the wall. Development of models for near-wall LES are described in sections 6 and 7

- **Filtering/discretization in inhomogeneous grids:** Inhomogeneous grids are the norm in complex or wall-bounded geometries. In these grids, the varying filter scale yields an inhomogeneous representation of the filtered variables; that is, the representation of the variables is strongly dependent on the position in the grid. An appropriate deconvolution method is a necessity for filtered simulations, especially for inhomogeneous grids, in order to place the results in different simulations and even in different regions of a flow geometry on a common ground.
- **Application to other discretization schemes:** While the work described here has focused on the finite-volume discretization, the methods presented can readily be applied to finite-difference and finite-element methods. The only difference in the modeling procedure is a redefinition of the filter and, therefore, of the quadratures used to compute the velocity correlations. A preliminary study with finite-difference methods has been initiated, but a more in-depth analysis is necessary. No reason exists to believe that any of these discretization methods is better or worse suited for LES and, in order to be widely accepted, the OFVLES model must be adapted to the different discretization procedures.

## 5 Development of a Model for the Three-Point Correlation

Multi-point velocity correlations are central to the statistical description of homogeneous isotropic turbulence<sup>22,23</sup>. The two-point second-order velocity correlation, and its Fourier transform, the velocity spectrum tensor, are the most commonly considered correlations, and a variety of models for their evolution have been developed (e.g EDQNM<sup>16</sup>).

In the evolution equation for the two-point velocity correlation in homogeneous turbulence, the two point third order correlation appears because of the non-linear terms in the Navier-Stokes equations. In isotropic turbulence, the two-point correlation equation reduces to the Karman-Howarth equation.<sup>24</sup> In combination with the Kolmogorov inertial range scaling assumptions, this leads to the well-known Kolmogorov 4/5 law<sup>25</sup> for the third order longitudinal structure function in the inertial range.

Isotropy of the turbulence also implies that the two-point third-order correlation can be uniquely determined in terms of the third-order structure function, just as the two-point second-order correlation can be written in terms of the second-order structure function. The two-point third order correlation describes the transfer of energy from large-scales to small, and as such is of critical importance to the theory of the two-point statistics of turbulence. It is also this relationship to energy transfer that allows the third-order structure function to be determined under the Kolmogorov assumptions, without an adjustable constant.

Of course, the two-point third-order correlation is a restricted case of the three-point correlation. But there is no direct association of the more general three-point quantity with the two-point correlation equation or with energy transfer. There has thus been little motivation to study the three-point correlation, and because of the complexity of this quantity, there has been virtually no work to characterize it.

In Large Eddy Simulation (LES), however, there is a motivation to characterize the three-point third order correlation. To see why this is true, note that the evolution equation for the two-point correlation of an LES field includes a term involving the two-point third-order correlation of the LES (i.e. filtered) velocity field, that arises from the quadratic terms in the LES equations. This correlation of filtered velocities represents energy transfer among scales in the LES due to the nonlinear term and is thus of importance to analyzing the dynamics of the LES equations. It is also one of the statistical inputs to the optimal LES modeling approach<sup>1,8,26</sup>. The two-point third order correlation of filtered velocity can be determined by applying the filter (three times) to the three-point third-order correlation (see section 5.1.1), which is the reason for our interest in the three-point correlation.

The notable exception to the lack of work on the three-point third-order correlation is the paper by Proudman & Reid<sup>7</sup>, in which the most general isotropic form of the Fourier transform of the three-point correlation is derived. In this paper, we start with some mathematical background (section 5.1). Then from Proudman & Reid's result for the Fourier transform of the correlation, the equivalent form for the physical-space correlation is determined and we find the simplest expression consistent with the Kolmogorov 4/5 law (section 5.2). Conclusions and implications are discussed in section 5.3.

## 5.1 Background

The Kolmogorov inertial range theory for high Reynolds number turbulence yields expressions for the longitudinal structure functions, under the well known similarity assumptions that in the inertial range, the statistical properties of turbulence depend on the separation scale and the rate of dissipation<sup>22,27</sup>. The longitudinal structure functions are:

$$S_p(r) = \langle (u_{\parallel}(\mathbf{x}) - u_{\parallel}(\mathbf{x} + \mathbf{r}))^p \rangle = C_p(\epsilon r)^{p/3} \quad (82)$$

where  $r = |\mathbf{r}|$  is the magnitude of the separation vector  $\mathbf{r}$ , which is assumed to be in the inertial range,  $u_{\parallel}$  is the velocity component in the separation direction,  $\epsilon$  is the average rate of kinetic energy dissipation (per unit mass) and  $C_p$  are the Kolmogorov constants, which are generally determined empirically (e.g.  $C_2 \approx 2$ ). The Kolmogorov expressions for the structure functions are found to be quite accurate for  $p = 2$  and 3, and their accuracy degrades as  $p$ . One of the remarkable consequences of the theory is that the evolution equation for the two-point correlation, in which the third-order two-point correlation appears, requires that  $C_3 = -4/5$ , the so-called Kolmogorov 4/5 law.

Isotropy and the continuity constraints are sufficient to determine the second- and third-order two-point correlation tensors from the second and third order structure functions respectively. Using the Kolmogorov expressions above, the correlation tensors are:

$$\mathbb{R}_{ij}(\mathbf{r}) = u^2 \delta_{ij} + \frac{C_2}{6} \epsilon^{2/3} (r)^{-4/3} (r_i r_j - 4(r)^2 \delta_{ij}) \quad (83)$$

$$\mathbb{S}_{ijk}(\mathbf{r}) = \frac{\epsilon}{15} \left( \delta_{ij} r_k - \frac{3}{2} (\delta_{ik} r_j + \delta_{jk} r_i) \right) \quad (84)$$

where the two-point correlations are defined:

$$\mathbb{R}_{ij}(\mathbf{r}) = \langle v_i(\mathbf{x}) v_j(\mathbf{x} + \mathbf{r}) \rangle \quad (85)$$

$$\mathbb{S}_{ijk}(\mathbf{r}) = \langle v_i(\mathbf{x}) v_j(\mathbf{x}) v_k(\mathbf{x} + \mathbf{r}) \rangle, \quad (86)$$

and  $u^2$  is 2/3 the turbulent kinetic energy which is also the velocity variance. The result for the second-order correlation is well known, but we are not aware of a previous reporting of the third-order two-point correlation as shown here, though it is implicit to the derivation of the 4/5 law, and is alluded to by Frisch<sup>22</sup>. For completeness, an outline of the derivation is given in Appendix I.

The three-point third-order velocity correlation, which is the quantity of interest here is defined:

$$\mathbb{T}_{ijk}(\mathbf{r}, \mathbf{s}) = \langle v_i(\mathbf{x}) v_j(\mathbf{x} + \mathbf{r}) v_k(\mathbf{x} + \mathbf{s}) \rangle \quad (87)$$

The three points form a triangle, and vectors  $\mathbf{r}$  and  $\mathbf{s}$  determine its size, shape, and orientation. Because it is a function of two vector arguments,  $\mathbb{T}$  is much more complex than the two-point correlation  $\mathbb{S}$ . However, we seek the analog of (84) for the three-point correlation. That is a “simple” tensor form consistent with known constraints and the Kolmogorov theory, particularly the 4/5 law.



### 5.1.1 Relationship to LES

In the usual formulation of Large Eddy Simulation (LES) the filtered velocity is defined:

$$\tilde{v}_i(\mathbf{x}) = \int G(\mathbf{x} - \mathbf{x}') v_i(\mathbf{x}') d\mathbf{x}' \quad (88)$$

where  $G(\mathbf{x})$  is the homogeneous filter kernel. The Navier-Stokes equations are then filtered to arrive at an evolution equation for  $\tilde{\mathbf{v}}$ :

$$\frac{\partial \tilde{v}_i}{\partial t} + \frac{\partial \tilde{v}_i \tilde{v}_j}{\partial x_j} = \frac{1}{\rho} \frac{\partial \tilde{P}}{\partial x_i} + \nu \frac{\partial^2 \tilde{v}}{\partial x_j \partial x_j} + \frac{\partial \tau_{ij}}{\partial x_j} \quad (89)$$

where

$$\tau_{ij} = \tilde{v}_i \tilde{v}_j - \widetilde{v_i v_j} \quad (90)$$

is the subgrid stress. Our concern for the moment is not with the subgrid stress but with the convection term.

When deriving the evolution equation for the two-point correlation of the filtered velocity  $\tilde{\mathbb{R}}_{ij}(\mathbf{r}) = \langle \tilde{v}_i(\mathbf{x}) \tilde{v}_j(\mathbf{x} + \mathbf{r}) \rangle$ , the convection term gives rise to terms that can be written as derivatives with respect to separation of the two-point third order correlation of filtered velocities

$$\tilde{\mathbb{S}}_{ijk}(\mathbf{r}) = \langle \tilde{v}_i(\mathbf{x}) \tilde{v}_j(\mathbf{x}) \tilde{v}_k(\mathbf{x} + \mathbf{r}) \rangle, \quad (91)$$

in the same way that the unfiltered two-point third order correlation arises in the unfiltered two-point correlation equation. As in the unfiltered equation, the energy transfer between scales of the filtered velocity is mediated by this term, including any transfer to the unresolved sub-filter scales. Because  $\tilde{\mathbb{S}}$  includes the product of filtered velocities evaluated at the same point  $\mathbf{x}$ , it cannot be determined by filtering  $\mathbb{S}$ . It can, however be found by filtering  $\mathbb{T}$ :

$$\tilde{\mathbb{S}}_{ijk}(\mathbf{r}) = \int \int \int G(\mathbf{s}) G(\mathbf{s} - \mathbf{r}') G(\mathbf{s} + \mathbf{r} - \mathbf{s}') \mathbb{T}_{ijk}(\mathbf{r}', \mathbf{s}') d\mathbf{s} d\mathbf{r}' d\mathbf{s}' \quad (92)$$

which can be derived easily by applying the filter (88) separately to each of the velocities in the definition of  $\mathbb{T}$ .

The two-point correlation equation also includes terms arising from the sub-filter stress term in the LES equations, which are derivatives of the two-point correlation of the sub-filter stress with the velocity

$$\mathbb{Q}_{ijk}(\mathbf{r}) = \langle \tau_{ij}(\mathbf{x}) v_k(\mathbf{x} + \mathbf{r}) \rangle. \quad (93)$$

The definition of  $\tau_{ij}$  (90) means that  $\mathbb{Q}$  can be expressed

$$\mathbb{Q}_{ijk}(\mathbf{r}) = \hat{\mathbb{S}}_{ijk}(\mathbf{r}) - \tilde{\mathbb{S}}_{ijk}(\mathbf{r}) \quad (94)$$

where  $\hat{\mathbb{S}}_{ijk}(\mathbf{r}) = \langle \widetilde{v_i v_j}(\mathbf{x}) \tilde{v}_k(\mathbf{x} + \mathbf{r}) \rangle$  can be determined by filtering the two-point third-order correlation of the unfiltered velocity

$$\hat{\mathbb{S}}_{ijk}(\mathbf{r}) = \int \int G(\mathbf{s}) G(\mathbf{s} + \mathbf{r} - \mathbf{r}') \mathbb{S}_{ijk}(\mathbf{r}') d\mathbf{s} d\mathbf{r}'. \quad (95)$$

In addition to its importance in analyzing the energy transfer in LES as described above,  $\tilde{\mathbb{S}}$  is also a necessary input for LES modeling using the optimal LES approach<sup>1,8</sup>. In optimal LES, models for the divergence of the subgrid stress are formulated to minimize mean square error using stochastic estimation, which requires the correlations described above. Thus for the purposes of analysis of LES and for optimal LES modeling, we are motivated to develop an analytic model for the three-point third order correlation.

### 5.1.2 The Fourier Transform of $\mathbb{T}$

Proudman and Reid<sup>7</sup> determined a general form for the Fourier transform of  $\mathbb{T}$  in both  $\mathbf{r}$  and  $\mathbf{s}$  (this is a six-dimensional Fourier transform). For an incompressible, homogeneous, isotropic turbulence, the most general possible form for the Fourier transform  $\Phi$  of  $\mathbb{T}$  is given by

$$\Phi_{ijk}(\mathbf{k}, \mathbf{p}) = \Delta_{im}(\mathbf{q})\Delta_{jn}(\mathbf{k})\Delta_{kp}(\mathbf{p})[\delta_{np}k_m\phi + \delta_{mp}p_n\phi_1 + \delta_{mn}k_p\phi_2 + k_mp_nk_p\zeta] \quad (96)$$

where the wavevectors  $\mathbf{k}$ ,  $\mathbf{p}$  and  $\mathbf{q}$  are interrelated  $\mathbf{k} + \mathbf{p} + \mathbf{q} = 0$ , and  $\Delta_{mi}(\mathbf{k}) = \delta_{im} - k_ik_m/k^2$  is the divergence-free projector. The scalar functions  $\phi$ ,  $\phi_1$ ,  $\phi_2$  and  $\zeta$  depend only on the magnitudes of the wavevectors. For an outline of the derivation of (96), see Appendix II. Symmetries in the tensor  $\mathbb{T}$  imply symmetries among scalar functions:

$$\phi(k, p, q) = -\phi(p, k, q) = \phi_1(q, k, p) = \phi_2(k, q, p) \quad (97)$$

Proudman & Reid<sup>7</sup> also analyze the dynamic equation for  $\Phi$  in the context of the quasi-normal approximation to find independent (model) dynamic equations for  $\phi$  and  $\zeta$ . These equations imply that for *stationary* turbulence,  $\zeta$  is zero. We will thus assume that  $\zeta = 0$ , and with the symmetries expressed in (97),  $\Phi$  is determined through (96) by a single scalar function  $\phi$  of  $k$ ,  $p$  and  $q$ . We start with this form in developing our real-space model for  $\mathbb{T}$ .

## 5.2 Inertial-range model of $\mathbb{T}$

To construct a model for the three-point third-order correlation, a general tensor form consistent with (96) is derived, and then the scalar function appearing in the expression is selected for consistency with the Kolmogorov 4/5 law.

### 5.2.1 A general form for $\mathbb{T}$ in real space

To develop the analog of (96) in real space, it will be inverse Fourier transformed to yield an expression for  $\mathbb{T}$ . However, to simplify the computations in real-space, it is convenient to recast the expression as

$$\Phi_{ijk}(\mathbf{k}, \mathbf{p}) = \tilde{\Delta}_{im}(\mathbf{q})\tilde{\Delta}_{jn}(\mathbf{k})\tilde{\Delta}_{kp}(\mathbf{p})[\delta_{np}ik_m\tilde{\phi}(k, p, q) + \delta_{mp}ip_n\tilde{\phi}(p, q, k) + \delta_{mn}ik_p\tilde{\phi}(k, q, p)] \quad (98)$$

where  $\tilde{\Delta}_{mi}(\mathbf{k}) = k^2 \delta_{mi} - k_m k_i$  is a modified divergence free operator, and  $\hat{\phi}(k, p, q) = -i\phi(k, p, q)/(k p q)^2$  is a modified scalar function that has the same symmetry properties as  $\phi$ . The advantage of this form is that the inverse Fourier transform will not give rise to inverse Laplacian operators. An inverse Fourier transform of (98) yields

$$\mathbb{T}_{ijk}(\mathbf{r}, \mathbf{s}) = \mathcal{P}_{im}^t \mathcal{P}_{jn}^s \mathcal{P}_{kp}^r [\delta_{np} \partial_m^s \psi(r, s, t) + \delta_{mp} \partial_n^r \psi(t, r, s) + \delta_{mn} \partial_p^s \psi(t, s, r)] \quad (99)$$

which is thus our general expression for  $\mathbb{T}$  in stationary, homogeneous, isotropic incompressible turbulence. Here, the third separation vector is  $\mathbf{t} = \mathbf{r} - \mathbf{s}$ , the scalar function  $\psi(r, s, t)$  is the inverse Fourier transform of  $\hat{\phi}$ , and  $r, s$  and  $t$  are the magnitudes of the separation vectors  $\mathbf{r}, \mathbf{s}$  and  $\mathbf{t}$  respectively. The operators appearing in (99) are defined:

$$\partial_i^r \equiv \left. \frac{\partial}{\partial s_i} \right|_{\mathbf{r}} \quad (100)$$

$$\partial_i^s \equiv \left. \frac{\partial}{\partial r_i} \right|_{\mathbf{s}} \quad (101)$$

$$\partial_i^t \equiv - \left. \frac{\partial}{\partial r_i} \right|_{\mathbf{s}} - \left. \frac{\partial}{\partial s_i} \right|_{\mathbf{r}} \quad (102)$$

vskip 4pt

$$\mathcal{P}_{ij}^\alpha \equiv \delta_{ij} \partial_k^\alpha \partial_k^\alpha - \partial_i^\alpha \partial_j^\alpha \quad (103)$$

It is straight-forward to confirm that the expression for  $\mathbb{T}$  in (99) satisfies the relevant symmetry and continuity constraints for the third-order three-point correlation, provided that

$$\psi(r, s, t) = -\psi(s, r, t), \quad (104)$$

which is the analogue of (97). The constraints on  $\mathbb{T}$  are:

$$\partial_i^t \mathbb{T}_{ijk} = \partial_j^s \mathbb{T}_{ijk} = \partial_k^r \mathbb{T}_{ijk} = 0 \quad (105)$$

$$\mathbb{T}_{ijk}(\mathbf{r}, \mathbf{s}) = \mathbb{T}_{ikj}(\mathbf{s}, \mathbf{r}) \quad (106)$$

$$\mathbb{T}_{ijk}(\mathbf{r}, \mathbf{s}) = \mathbb{T}_{jki}(-\mathbf{t}, -\mathbf{r}) \quad (107)$$

$$(108)$$

The tensor form given in (99) is clearly linear in  $\psi$ , indeed it can be expressed as:

$$\mathbb{T}_{ijk} = \mathcal{L}_{ijk}(\psi) \quad (109)$$

where  $\mathcal{L}_{ijk}$  is the tensor-valued linear operator implied by (99). To complete the model of the three-point third-order correlation, we need only specify  $\psi(r, s, t)$  satisfying (104).

### 5.2.2 Scalar function $\psi$ in the inertial range

Our primary interest is a model for  $\mathbb{T}$  that is valid in the inertial range, analogous to the inertial range expression for  $\mathbb{S}$  (84). Kolmogorov's 4/5 law constrains  $S$  to vary linearly with separation.

Since  $\mathbb{T}$  must reduce to  $\mathbb{S}$  when  $r$ ,  $s$  or  $t$  are zero, this linearity must be reflected in  $\mathbb{T}$  as well. More generally, the Kolmogorov similarity argument<sup>22,25</sup> requires that in the inertial range

$$\mathbb{T}(\alpha \mathbf{r}, \alpha \mathbf{s}) = \alpha \mathbb{T}(\mathbf{r}, \mathbf{s}) \quad (110)$$

The simplest way to ensure this linearity is to choose  $\psi(r, s, t)$  to be a polynomial in  $r$ ,  $s$  and  $t$ . Since each term in (99) is a seventh derivative of  $\psi$ , only terms with total degree of 8, will contribute to the linear scaling of  $\mathbb{T}$ . This, along with the symmetry constraint on  $\psi$  (104) suggests that  $\psi$  be constructed from terms of the form

$$p_{a,b} \equiv (r^a s^b - r^b s^a) t^c \quad (111)$$

with  $a + b + c = 8$  and  $a, b, c \geq 0$ . There are only 20 expressions of this form, and of these 14 produce non-zero  $\mathbb{T}$  when substituted for  $\psi$  in (99).

However, all of these 14 non-trivial  $\mathbb{T}$  are singular when  $r$ ,  $s$  or  $t$  are zero. For example, terms such as:  $r_i r_j r_k r / s^3$  arise, which is clearly singular at  $s = 0$ . In addition, terms like  $\delta_{ij} s_k r / s$  arise, which is discontinuous at  $s = 0$ . It was found, however, that there is a 5-dimensional null space of the singular and discontinuous terms. There is thus a 5-dimensional space of possible  $\psi$  functions that yield non-singular, continuous  $\mathbb{T}$ . The space is spanned by the following 5 functions:

$$\psi^1 = \frac{1}{5760} [-27p_{0,3} - 3p_{0,5} + 4p_{2,3} + 18p_{3,5}] \quad (112)$$

$$\psi^2 = \frac{1}{1155840} [-315p_{0,3} + 4p_{0,7} + 56p_{2,5} - 140p_{3,4} + 1260p_{3,5}] \quad (113)$$

$$\psi^3 = \frac{1}{1257600} [-4p_{0,1} - 1935p_{0,3} - 40p_{1,2} + 80p_{1,3} - 60p_{1,4} + 16p_{1,5} + 180p_{2,3} + 990p_{3,5}] \quad (114)$$

$$\psi^4 = \frac{1}{462720} [-4p_{0,1} - 1215p_{0,3} - 36p_{1,2} + 64p_{1,3} - 36p_{1,4} + 4p_{1,6} + 108p_{2,3} - 20p_{2,5} + 40p_{3,4} + 270p_{3,5}] \quad (115)$$

$$\psi^5 = \frac{1}{10684800} [-60p_{0,1} - 16065p_{0,3} - 504p_{1,2} + 840p_{1,3} - 420p_{1,4} + 24p_{1,7} + 1260p_{2,3} + 7560p_{3,5}] \quad (116)$$

Where  $p_{i,j}$  are as defined in (111) above. These functions have been normalized so that each of the  $\mathbb{T}^n = \mathcal{L}(\psi^n)$  satisfies

$$\mathbb{T}_{ijk}^n(0, \mathbf{r}) = \frac{1}{15} \left( \delta_{ij} r_k - \frac{3}{2} (\delta_{ik} r_j + \delta_{jk} r_i) \right) \quad (117)$$

which is just (84) with  $\epsilon$  set to 1. The analytic model we seek for  $\mathbb{T}$  is thus given by:

$$\mathbb{T}_{ijk}(\mathbf{r}, \mathbf{s}) = \sum_{n=1}^5 a_n \mathbb{T}_{ijk}^n(\mathbf{r}, \mathbf{s}) \quad \text{with} \quad \sum_{n=1}^5 a_n = \epsilon \quad (118)$$

While the scalar basis functions  $\psi^n$  are relatively simple to write down (112–116), the basis tensors  $\mathbb{T}^n$  are not. Indeed the expressions are so complex, they will not be written out here. But a program is available to evaluate the tensor symbolically and numerically at <http://turbulence.ices.utexas.edu>

$a_1/\epsilon$	0.884
$a_2/\epsilon$	-2.692
$a_3/\epsilon$	-6.099
$a_4/\epsilon$	-5.853
$a_5/\epsilon$	14.760

Table 4: Values of the model coefficients found by fitting DNS data of Langford & Moser<sup>1</sup>

To display the features of the five basis tensors defined above, we examine the various components of the tensor for two special arrangements of the separation vectors. First is with the separation vectors  $\mathbf{r}$  and  $\mathbf{s}$  colinear (parallel, designated by  $\parallel$ ), which, without loss of generality, we choose to be in the  $x_1$  direction ( $\mathbf{r} = r\mathbf{e}_1$ ,  $\mathbf{s} = s\mathbf{e}_1$ ). In this case, there are only seven non-zero components, of which only  $\mathbb{T}_{111}^{\parallel}$  and  $\mathbb{T}_{122}^{\parallel}$  are independent. The other 5 ( $\mathbb{T}_{212}^{\parallel}$ ,  $\mathbb{T}_{221}^{\parallel}$ ,  $\mathbb{T}_{133}^{\parallel}$ ,  $\mathbb{T}_{313}^{\parallel}$  and  $\mathbb{T}_{331}^{\parallel}$ ) are related to  $\mathbb{T}_{122}^{\parallel}$  through symmetry.

The second separation vector configuration is with  $\mathbf{r}$  and  $\mathbf{s}$  orthogonal (designated by  $\perp$ ). Again, without loss of generality  $\mathbf{r} = r\mathbf{e}_1$  is chosen to be in the  $x_1$ -direction, and  $\mathbf{s} = s\mathbf{e}_2$  is chosen in the  $x_2$ -direction. In this configuration, there are 14 nonzero components, of which seven are independent:  $\mathbb{T}_{111}^{\perp}$ ,  $\mathbb{T}_{112}^{\perp}$ ,  $\mathbb{T}_{121}^{\perp}$ ,  $\mathbb{T}_{122}^{\perp}$ ,  $\mathbb{T}_{133}^{\perp}$ ,  $\mathbb{T}_{313}^{\perp}$ ,  $\mathbb{T}_{323}^{\perp}$ . Each of these is one of a pair of symmetrically related components.

Since the tensor functions vary linearly with separation, the tensors can be normalized by  $\rho \equiv \max(r, s, t)$ , which for the special separation configurations considered leaves only the dependence on  $s/r$ . The non-zero, non-redundant components of  $\mathbb{T}^{\parallel}/\rho$  and  $\mathbb{T}^{\perp}/\rho$  are shown in figure 19 as a function of  $\theta = \arctan(s/r)$ . Note that the five basis tensors have similar structure, and that two of them are quite similar. There has been no effort to orthogonalize the basis.

### 5.2.3 Fitting to DNS data

To determine the 5 coefficients  $\{a_1, a_2, \dots, a_5\}$  in (118), a least-squares fit to data from a Direct Numerical Simulation (DNS) of forced isotropic turbulence at  $Re_{\lambda} = 164^1$  is performed. Let  $\mathbb{E}(\mathbf{r}, \mathbf{s}) = \mathbb{T}^{\text{DNS}} - \mathbb{T}^{\text{model}}$ , be the error tensor. Then the fitting was done to minimize the objective function:

$$F = \left(1 - \frac{2}{\pi}\right) \int \mathbb{E}_{ijk}^{\parallel}(r, s) \mathbb{E}_{ijk}^{\parallel}(r, s) dr ds + \frac{2}{\pi} \int \mathbb{E}_{ijk}^{\perp}(r, s) \mathbb{E}_{ijk}^{\perp}(r, s) dr ds \quad (119)$$

under the constraint that  $\sum_n a_n = \epsilon$ , where only separation vectors  $\mathbf{r}$  and  $\mathbf{s}$  that are parallel or perpendicular are considered, to reduce the data requirements to a manageable level, and the integrals are taken over the domain in  $r$  and  $s$  for which  $\rho$  is in the approximate inertial range for the DNS ( $\rho \in [0.15, 0.25]$ ). This objective was selected as a (crude) approximation to the integral over all  $\mathbf{r}$  and  $\mathbf{s}$  in the inertial range. The coefficients obtained from this fit are given in table 4. The coefficient of determination is  $R^2 = 0.96$ , indicating that our model describes the DNS data quite well.

The ability of the model to represent the DNS correlations is shown in figure 20, in which non-

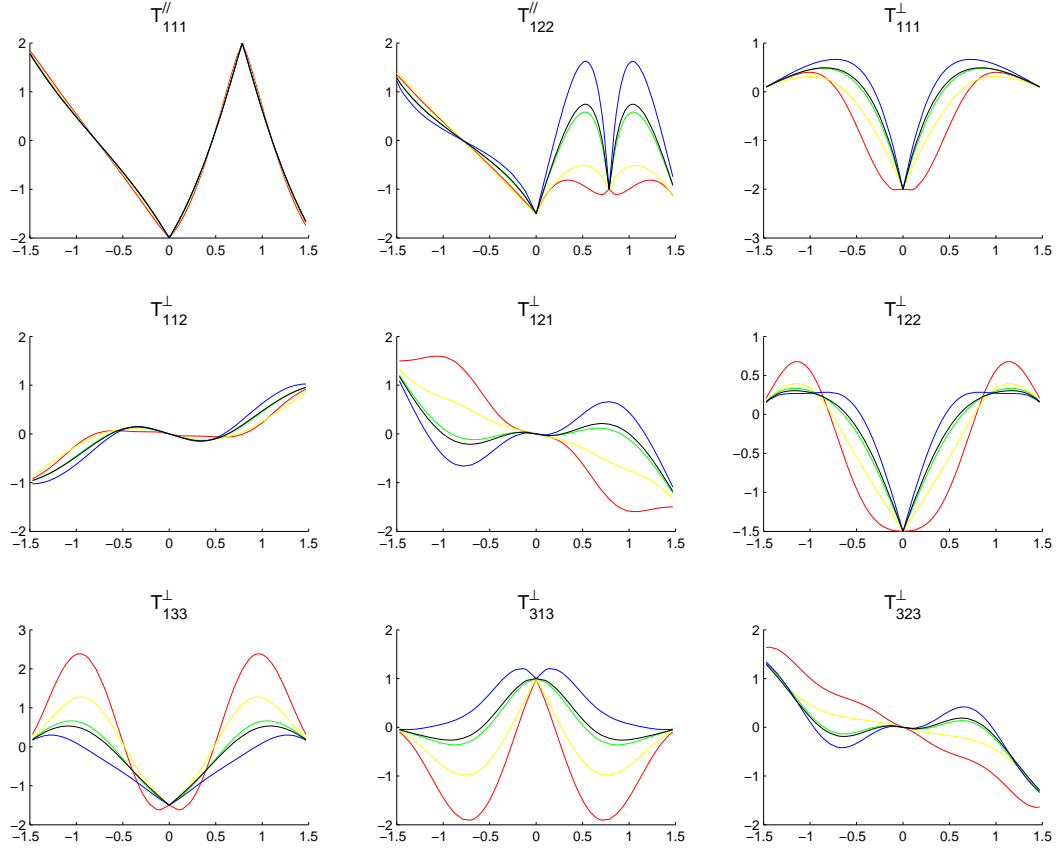


Figure 19: Basis functions for the non-zero, non-redundant components of  $\mathbb{T}^{\parallel}/\rho$  and  $\mathbb{T}^{\perp}/\rho$  (see text for definitions) as functions of  $\theta = \arctan(s/r)$ .  $\color{red}$ need color key $\color{blue}$

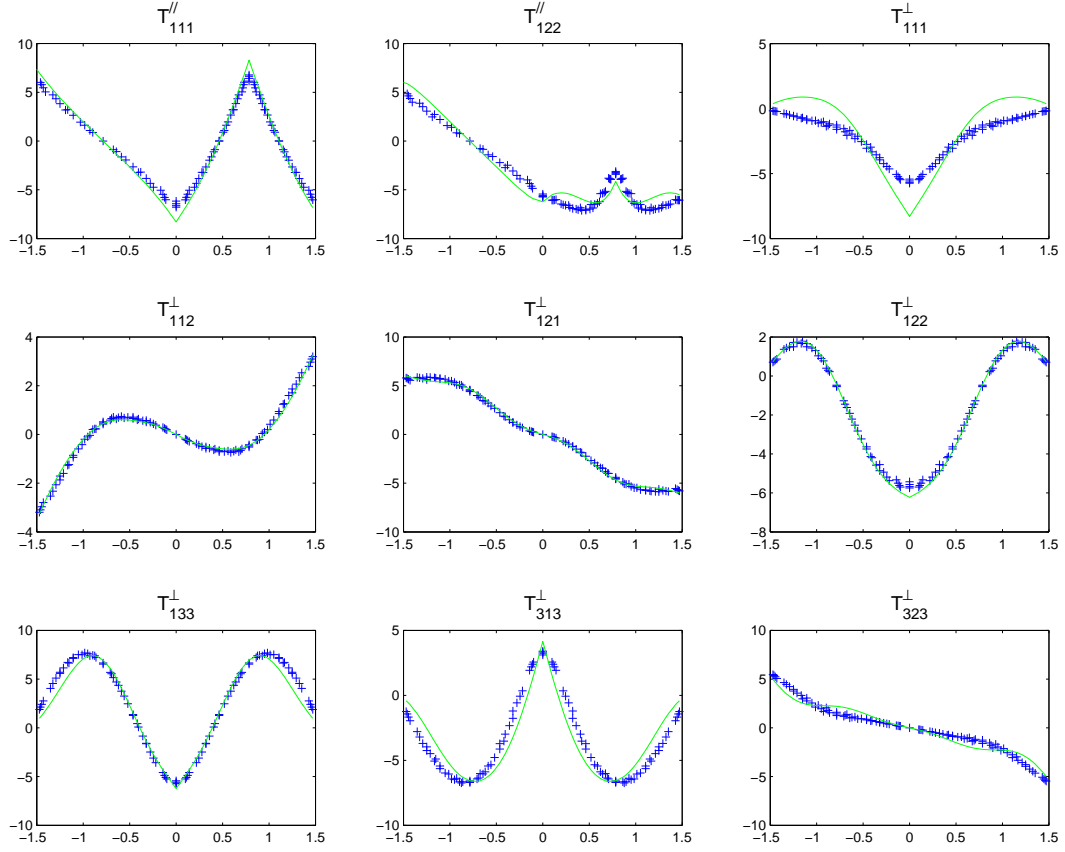


Figure 20: DNS data and analytical model for  $\mathbb{T}$

zero components of  $\mathbb{T}/\rho$  are plotted as a function of  $\theta$ , for the parallel and perpendicular separation vectors, as in figure 19. The agreement between model and correlations is very good. Further indication of the quality of the model is given in figure 21, where contour plots show the non-zero components of  $\mathbb{T}$  as functions of  $r$  and  $s$  in both the model and the DNS. Since there is a symmetry in each term shown, the DNS and model are shown together in each frame, with a line of symmetry dividing them. The model and DNS are very similar. But, there is a minor discrepancy for  $r$  and  $s$  near zero, which is due to viscous effects not represented in the model.

### 5.3 Discussion and Implications

It is remarkable that the simple considerations of isotropy and Kolmogorov scaling are sufficient to completely determine the two-point third-order correlation, a third-ranked tensor. The three-point third-order correlation is a much more complicated object, so it is equally remarkable that the same scaling and isotropy considerations, along with a plausible modeling ansatz regarding functional

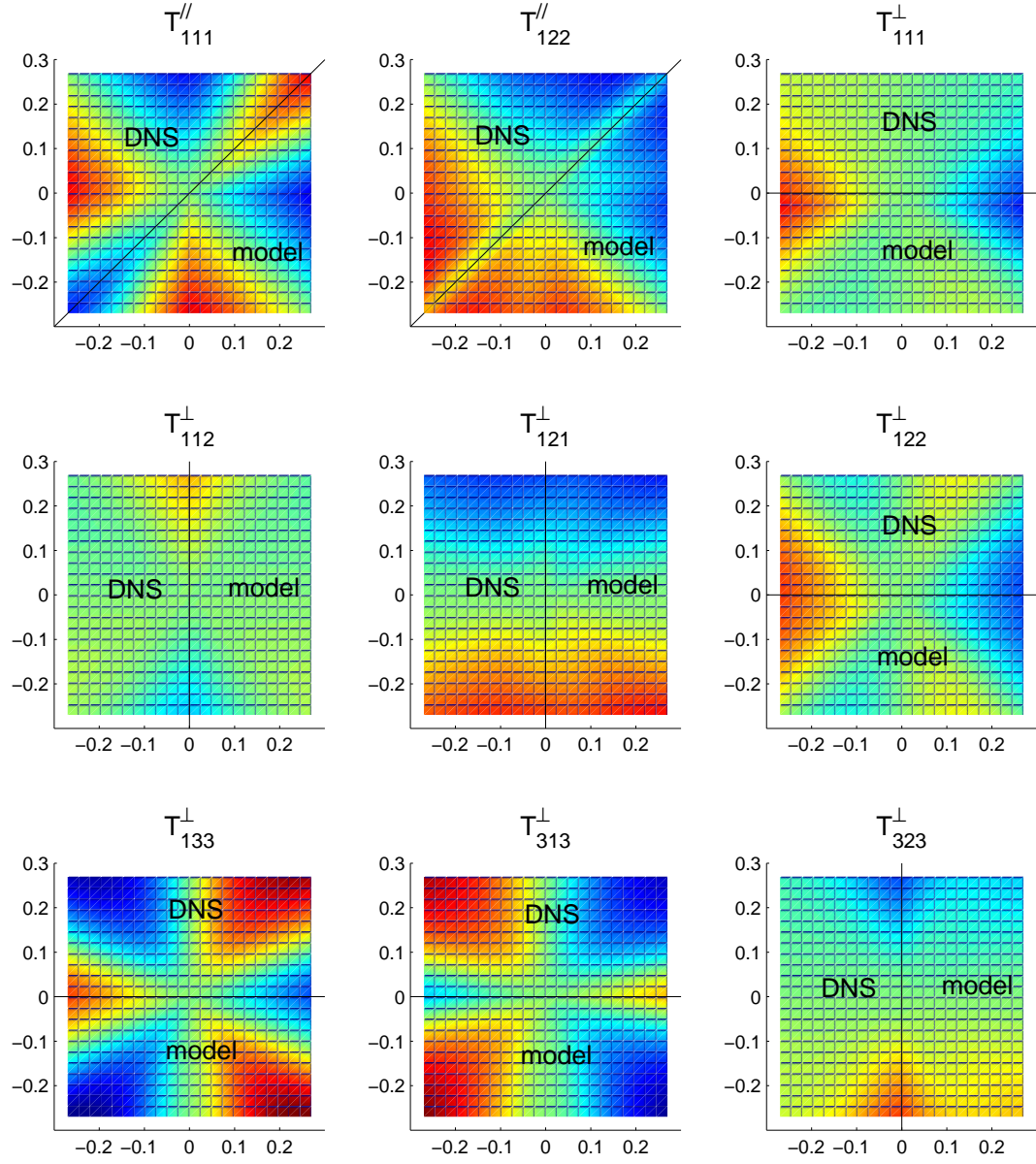


Figure 21: DNS data and analytical model for  $\mathbb{T}$



forms (111), is sufficient to specify a model for the three-point correlation in the inertial range with just four free constants. The model appears to fit low Reynolds number DNS data quite well. It would also be useful to test the model against higher Reynolds number DNS data.

While the considerations leading to the model are simple, the model itself is algebraically very complex. A special-purpose tensor algebra program was written to perform the necessary manipulations. Given the complexity of the expressions, it may be that the ability to evaluate tensor components numerically will be most useful, and a program to perform such evaluations has been developed, and is available at <http://turbulence.ices.utexas.edu>.

The three-point third-order correlation is of particular interest in the analysis and modeling of LES, because by applying the LES filter to the three-point correlation one can determine third-order correlations of the filtered velocity. This is important in analyzing the transfer of energy among scales, and in formulating LES models. In particular, the representation of the three-point correlation will allow optimal LES models of the type evaluated by Zandonade *et al*<sup>8</sup> to be formulated without the need for DNS statistical data.

## Determination of $\mathbb{S}$ in the inertial range

The derivation of (84) starts from the general form of an isotropic two-point third-order tensor function of a vector argument

$$\mathbb{S}_{ijk}(\mathbf{r}) = \langle u_i(\mathbf{x})u_j(\mathbf{x})u_k(\mathbf{x} + \mathbf{r}) \rangle = a r_i r_j r_k + b \delta_{jk} r_i + c \delta_{ik} r_j + d \delta_{ij} r_k \quad (120)$$

where the scalars  $a$ ,  $b$ ,  $c$  and  $d$  are functions of the magnitude of the separation vector  $r = \|\mathbf{r}\|$  only. Symmetry in  $i$  and  $j$  requires that  $b = c$ . Further, the continuity constraint  $\partial \mathbb{T}_{ijk} / \partial r_k = 0$  allows the functions  $a$ ,  $b$  and  $d$  to be eliminated in terms of the third-order longitudinal correlation function:

$$f(\mathbf{r}) = \langle v_{\parallel}^2(\mathbf{x})v_{\parallel}(\mathbf{x} + \mathbf{r}) \rangle, \quad (121)$$

where  $v_{\parallel}$  is the velocity component parallel to the separation vector  $\mathbf{r}$ . The result is

$$\mathbb{S}_{ijk}(\mathbf{r}) = \left\{ \frac{1}{2} \left( f - r \frac{\partial f}{\partial r} \right) \frac{r_i r_j r_k}{r^3} + \frac{1}{4r^2} (\delta_{jk} r_i + \delta_{ik} r_j) \frac{\partial}{\partial r} ((r^2 f) - \frac{f}{2r} \delta_{ij} r_k) \right\}. \quad (122)$$

The third-order longitudinal correlation function is directly related to the third-order structure function, which in the Kolmogorov inertial range is  $S_3(r) = -\frac{4}{5}\epsilon r$ . The correlation  $f(r)$  can thus be written

$$f(r) = \frac{S_3(r)}{6} = -\frac{2\epsilon r}{15} \quad (123)$$

Substituting into 122 then immediately yields (84).

## The Most General Form for $\Phi$

Presented here is a condensed version of the derivation from Proudman and Reid<sup>7</sup>. The three-point third-order velocity correlation is  $\mathbb{T}_{ijk}(\mathbf{r}, \mathbf{s}) \equiv \langle v_i(\mathbf{x})v_j(\mathbf{x} + \mathbf{r})v_k(\mathbf{x} + \mathbf{s}) \rangle$ . It's Fourier transform is

$$\Phi_{ijk}(\mathbf{k}, \mathbf{p}) = i(2\pi)^{-6} \int \int \mathbb{T}_{ijk}(\mathbf{r}, \mathbf{s}) e^{-i(\mathbf{k} \cdot \mathbf{r} + \mathbf{p} \cdot \mathbf{s})} d\mathbf{r} d\mathbf{s} \quad (124)$$

Consistency with continuity requires:

$$(k_i + p_i)\Phi_{ijk}(\mathbf{k}, \mathbf{p}) = k_j\Phi_{ijk}(\mathbf{k}, \mathbf{p}) = p_k\Phi_{ijk}(\mathbf{k}, \mathbf{p}) = 0 \quad (125)$$

While the most general isotropic third-ranked tensor function of two vectors is:

$$\begin{aligned} \phi_{mnp}(\mathbf{k}, \mathbf{p}) = & \phi_1 k_m k_n k_p + \phi_2 k_m k_n p_p + \phi_3 k_m p_n k_p + \phi_4 p_m k_n k_p \\ & + \phi_5 p_m p_n p_p + \phi_6 p_m p_n k_p + \phi_7 p_m k_n p_p + \phi_8 k_m p_n p_p \\ & + \phi_9 k_m \delta_{np} + \phi_{10} k_n \delta_{mp} + \phi_{11} k_p \delta_{mn} + \phi_{12} p_m \delta_{np} + \phi_{13} p_n \delta_{mp} + \phi_{14} p_p \delta_{mn} \end{aligned} \quad (126)$$

where  $\{\phi_1, \phi_2, \dots, \phi_{14}\}$  are scalar functions of the magnitudes of the wavevectors  $k \equiv \|\mathbf{k}\|$ ,  $p \equiv \|\mathbf{p}\|$ , and  $q \equiv \|\mathbf{q}\|$ , and  $\mathbf{k} + \mathbf{p} + \mathbf{q} = 0$ .

To enforce incompressibility, we employ the divergence-free projector  $\Delta_{im}(\mathbf{k}) \equiv \delta_{im} - k_i k_m / k^2$ . So, to satisfy all three incompressibility conditions in equation (125) and isotropy, we apply three orthogonal projectors to  $\phi_{mnp}$ , the result is the most general form for  $\Phi_{ijk}$ .

$$\Phi_{ijk}(\mathbf{k}, \mathbf{p}) = \Delta_{im}(\mathbf{q}) \Delta_{jn}(\mathbf{k}) \Delta_{kp}(\mathbf{p}) \phi_{mnp}(\mathbf{k}, \mathbf{p}) \quad (127)$$

Furthermore, the triple projection operator directly eliminates all but 4 components of  $\phi_{mnp}$  shown in equation (126), so effectively the above equation becomes

$$\Phi_{ijk}(\mathbf{k}, \mathbf{p}) = \Delta_{im}(\mathbf{q}) \Delta_{jn}(\mathbf{k}) \Delta_{kp}(\mathbf{p}) [\phi_3 k_m p_n k_p + \phi_9 k_m \delta_{np} + \phi_{11} k_p \delta_{mn} + \phi_{13} p_n \delta_{mp}] \quad (128)$$

Renaming the scalar functions as follows:  $\phi_3 \rightarrow \zeta$ ,  $\phi_9 \rightarrow \phi$ ,  $\phi_{11} \rightarrow \phi_2$ ,  $\phi_{13} \rightarrow \phi_1$ , we obtain (96).

## 6 Modeling the Two-Point Correlation in Wall-Bounded Turbulence

For a given velocity field  $\mathbf{u}(\mathbf{x})$ , the two point correlation tensor  $R_{ij}$  is given by

$$R_{ij}(\mathbf{x}, \mathbf{r}) = \langle u'_i(\mathbf{x}) u'_j(\mathbf{x} + \mathbf{r}) \rangle \quad (129)$$

where  $\mathbf{u}' = \mathbf{u} - \langle \mathbf{u} \rangle$  is the fluctuating velocity field. Two point correlations of velocity fluctuations are important in turbulence modeling due to the rich information they contain about the local and global structure of turbulent flows. More importantly for the current purposes, multipoint correlations are used to construct Optimal LES (OLES) models<sup>1,8,28</sup>.

To construct fully analytical models for LES we need to be able to reconstruct the multipoint correlations of  $\mathbf{u}'$  from the statistics of the filtered fields, which are finite dimensional quantities. Therefore it is important that finite dimensional representations of the correlations of  $\mathbf{u}'$  be devised so that a correspondence can be developed between the LES statistics and the correlations. It is this need for building representations for velocity correlations in a turbulent flow with complex geometry that motivates the current work.

Most of the models for two point correlations have been expressed in the fourier wave-number space in terms of the spectrum tensor (e.g. theories based on EDQNM<sup>29</sup> and RDT<sup>30</sup>). While these models capture many of the fundamental processes of turbulence, the global nature of the fourier basis functions means that the representations of  $R_{ij}$  constructed from them cannot be used easily for flows in complex geometries, especially in wall bounded flows. Therefore we choose to construct our representation for  $R_{ij}$  in physical space, in terms of tensor functions of  $\mathbf{x}$  and  $\mathbf{r}$ .

One of the key properties of  $R_{ij}$  that needs to be represented is its anisotropy, both with regard to how different  $R_{ij}(\mathbf{x}, \mathbf{r})$  is from  $R_{kk}(\mathbf{x}, \mathbf{r})\delta_{ij}/3$  for a constant  $\mathbf{x}, \mathbf{r}$  (componental anisotropy) and how  $R_{\alpha\beta}(\mathbf{x}, \mathbf{r})$  behaves over  $\mathbf{r}/r$  for a given  $\mathbf{x}$ ,  $\alpha$ ,  $\beta$  and  $r$  (directional anisotropy). In order to address these issues, Procaccacia<sup>31</sup> formulated a basis for  $R_{ij}$  in terms of subspaces which are invariant to rigid rotation of the frame of reference (i.e. an  $SO(3)$  decomposition) where each finite dimensional subspace is constructed from a particular spherical harmonics mode  $Y_m^l(\phi, \theta)$ . It was proposed that there was a hierarchy of subspaces, where the subspace with lower  $l$  contributes the most to  $R_{ij}(\mathbf{r})$  at intermediate separations<sup>3</sup>. This approach could potentially yield finite dimensional models for  $R_{ij}$ , but it is unclear whether the proposed hierarchy exists for turbulent flows in complex geometries. For instance, in a wall bounded inhomogenous flow, the  $SO(3)$  symmetry is broken in the equations for  $R_{ij}$ , and it becomes hard to argue that the proposed hierarchy will be true. This points to a need for, first, identifying the important dynamic and kinematic properties of  $R_{ij}$  (which are finite in number); second, ensuring that the finite dimensional representation of  $R_{ij}$  is capable of capturing these properties in any flow geometry.

In this work we construct a representation for  $R_{ij}$  in terms of structure tensors, proposed by Kassinos *et al*<sup>6</sup> (referred from now on as KRR). These second order tensors are single point moments of derivatives of fluctuating stream-functions, which can therefore be related to integrals of two point correlations over  $\mathbf{r}$ . Even though these tensors are single point moments, they contain information about the “structure” of turbulence, e.g. the distribution of energy in different components

---

<sup>3</sup>The term *intermediate separation* will be used throughout this work to denote  $r$  in the inertial range  $\eta \ll r \ll \mathcal{L}$ , where  $\eta$  is the kolmogorov length scale and  $\mathcal{L}$  is the scale defined by the geometry of the flow

of velocity, the dimension of turbulence, etc (discussed in detail in section 6.1). In the context of constructing a closure model for reynolds stresses, it was shown by KRR that it is vital to represent the pressure-strain correlation in terms of structure tensors in order to obtain the correct evolution of the reynolds stress components in the rapid distortion limit. In light of the useful properties of structure tensors, we propose that one should be able to extract the correct value of structure tensors from any representation of  $R_{ij}$ . Since  $R_{ij}$  is not unique to a given set of structure tensors, our approach is to use the theory of invariants<sup>32</sup> to formulate the most general linear representation of  $R_{ij}$  in terms of the structure tensors (section 6.2.1). We then devise two sets of constraints; the first set ensures that  $R_{ij}$  satisfies the continuity equation, and the second set ensures that  $R_{ij}$  has the necessary conditions such that the structure tensors calculated from the correlation are the same as the structure tensors used in the representation (section 6.2.2).

In a similar approach Oberlack<sup>5</sup> has represented  $R_{ij}(\mathbf{x}, \mathbf{r})$  in terms of  $\mathbf{r}$  and a tensor length scale related to the Reynolds stress tensor and the dissipation rate tensor  $\epsilon_{ij} = \nu \langle u'_{i,k} u'_{j,k} \rangle$ . The significant difference in our approach from the latter is that unlike the structure tensors, Reynolds stress and dissipation tensors do not have information about the directional anisotropy of  $R_{ij}$ , and therefore a better representation of the directional anisotropy can be expected in our approach.

In order to evaluate the capabilities and shortcomings of our representation, we obtain a model for  $R_{ij}$  by fitting it to correlation obtained from DNS and comparing the two correlations (section 6.3). This exercise points to improvements needed in the model.

## 6.1 Background

### 6.1.1 Definition of structure tensors

Structure tensors are single point moments of derivatives of stream-functions. The velocity field and stream-function are related to each other through the following equations:

$$u'_i = \epsilon_{its} \psi'_{s,t} \quad (130)$$

$$\psi'_{k,k} = 0 \quad (131)$$

Equation (131) ensures that  $\psi'$  is related to the vorticity through Poisson's equation:

$$\omega_i = \epsilon_{imn} u'_{n,m} = -\psi'_{i,tt} \quad (132)$$

In this work, our discussion and use of structure tensors will be limited to the specific case of homogeneous turbulence. The set of structure tensors which are nonzero for homogeneous turbulence are given by the Reynolds stress (or componentality)  $B_{ij}$ , dimensionality  $D_{ij}$ , circulicity  $F_{ij}$  and strophylisis  $\tilde{Q}_{ijk}^*$ . They are defined in terms of the fluctuating velocity stream-function as

follows:

$$B_{ij} = \epsilon_{ipq}\epsilon_{jts} \langle \psi'_{q,p} \psi'_{s,t} \rangle \quad (133)$$

$$D_{ij} = \langle \psi'_{n,i} \psi'_{n,j} \rangle \quad (134)$$

$$F_{ij} = \langle \psi'_{i,n} \psi'_{j,n} \rangle \quad (135)$$

$$\tilde{Q}_{ijk}^* = \mathcal{S}[Q_{ijk}] \quad (136)$$

$$\text{where } Q_{ijk} = -\langle u'_j \psi'_{i,k} \rangle \quad (137)$$

and  $\mathcal{S}$  is an operator which symmetrizes any third order tensor as follows:

$$\mathcal{S}[T_{ijk}] = \frac{1}{6} [T_{ijk} + T_{jki} + T_{kij} + T_{ikj} + T_{jik} + T_{kji}] \quad (138)$$

Expanding eqn (133), and using eqns (134), (135) and (131), the following relation can be derived among the structure tensors:

$$B_{ij} + D_{ij} + F_{ij} = \delta_{ij} q^2 \quad (139)$$

where  $q^2 = B_{kk}$ . Thus only two of the three second order structure tensors are linearly independent for homogeneous turbulence, and we choose  $\mathbf{B}$  and  $\mathbf{D}$  for our modeling purposes. It was shown by KRR that in the presence of frame rotation, the strophylisis  $\mathbf{Q}^*$  becomes important, and therefore we will use it for our model as well.

### 6.1.2 Exact relation between structure tensors and $R_{ij}$

To express structure tensors in terms of  $R_{ij}$ , we define a new tensor  $\Phi_{ijk}(\mathbf{r}) = -\langle u'_j(\mathbf{x}) \psi'_{i,k}(\mathbf{x} + \mathbf{r}) \rangle$ . Using eqn (132), we get

$$\begin{aligned} \frac{\partial^2 \Phi_{ijk}(\mathbf{r})}{\partial r_i \partial r_l} &= -\frac{\partial}{\partial r_k} \left\langle u'_j(\mathbf{x}) \frac{\partial^2 \psi'_{i,k}(\mathbf{x} + \mathbf{r})}{\partial r_l \partial r_l} \right\rangle \\ &= \frac{\partial}{\partial r_k} \langle u'_j(\mathbf{x}) \omega_i(\mathbf{x} + \mathbf{r}) \rangle \\ \Rightarrow \nabla_{\mathbf{r}}^2 \Phi_{ijk}(\mathbf{r}) &= \epsilon_{imn} \frac{\partial^2 R_{jn}(\mathbf{r})}{\partial r_k \partial r_m} \end{aligned} \quad (140)$$

Assuming that the right hand side of eqn (140) vanishes at infinity (enabling us to use the free space green's function of the laplacian), and noting that  $Q_{ijk} = \Phi_{ijk}(0)$ , the following is obtained:

$$\tilde{Q}_{ijk}^* = \mathcal{S}[Q_{ijk}] = \mathcal{S} \left[ \frac{\epsilon_{imn}}{4\pi} \int_V \frac{1}{r} \frac{\partial^2 R_{jn}(\mathbf{r})}{\partial r_k \partial r_m} d\mathbf{r} \right] \quad (141)$$

Where  $V = \mathbb{R}^3$ . The relation for  $B_{ij}$  and  $D_{ij}$  can now be given as follows

$$B_{ij} = \epsilon_{ilm} Q_{ljm} = \frac{1}{4\pi} \int_V \frac{1}{r} \frac{\partial^2 R_{ij}(\mathbf{r})}{\partial r_k \partial r_k} d\mathbf{r} \quad (142)$$

$$D_{ij} = \epsilon_{ilm} Q_{mlj} = \frac{1}{4\pi} \int_V \frac{1}{r} \frac{\partial^2 R_{kk}(\mathbf{r})}{\partial r_i \partial r_j} d\mathbf{r} \quad (143)$$

Eqn (142) can be seen to be the evaluation of inverse laplacian of the laplacian of  $R_{ij}(\mathbf{r})$  at  $\mathbf{r} = 0$ , and thus represents the Reynolds stress tensor, which simply gives the amount of energy in different velocity fluctuation components.  $D_{ij}$  is a measure of how  $R_{ij}(\mathbf{r})$  varies with  $\mathbf{r}/r$  and this will be explained in the following subsection.

### 6.1.3 Information contained in $D_{ij}$

In order to understand the link between the anisotropy of  $R_{ij}(\mathbf{r})$  and  $D_{ij}$ , let us examine a hypothetical (but physically legitimate) correlation given as follows:

$$R_{ij}(\mathbf{r}) = B_{ij} + f(r)[r_l T_{lm} r_m] \delta_{ij} \quad (144)$$

where  $f(r)$  has the properties which ensure that the integral in eqn (142) does not become singular and that for  $r < L$ ,  $R_{ij} \approx B_{ij} + [r_l T_{lm} r_m] \delta_{ij}$ <sup>4</sup>. We will assume  $T_{ij}$  to be a positive-definite diagonal tensor, with  $T_{11} < T_{22}$ . The isocontour of  $R_{kk}(\mathbf{r})$  is an ellipsoid with principle axes coincident with the axes of the reference frame,  $1/\sqrt{T_{\alpha\alpha}}$  being the length of the principle axis in the  $\hat{e}_\alpha$  direction. Thus,  $R_{kk}(\mathbf{r})$  is more correlated in the  $x$  direction compared to the  $y$  direction (fig 22). Substituting the correlation into eqn (143) gives

$$D_{ij} \approx T_{ij} L^2 \quad (145)$$

Thus the eigenvalues and eigenvectors of  $D_{ij}$  give the values and directions of the principle axis of the isocontours of the ellipsoid characterizing  $R_{kk}$ . A similar conclusion can be extended for  $\tilde{Q}_{ijk}^*$ , though we will not elucidate on it, since the nature of anisotropy it captures is more complicated compared to  $D_{ij}$

## 6.2 Formulation of Representation

### 6.2.1 General form of the linear representation

In section 6.1 it was shown that the structure tensors contain relevant information about the anisotropy of  $R_{ij}$ . Conversely, we will assume that a representation of the form  $\tilde{F}_{ij}(\mathbf{r}, \mathbf{B}, \mathbf{D}, \tilde{\mathbf{Q}}^*)$  is capable

<sup>4</sup>A sufficient condition would be that  $f(r)$  is analytical for all  $r \in \mathbb{R}^+$ ,  $\lim_{r \rightarrow \infty} f(r) = 0$ . Also,  $f(r) \approx 1$  for  $\epsilon < r < L$ , and  $f(r) \ll 1$  for  $r \geq L$  where  $\epsilon \ll 1$  and  $L$  defines the integral scale of the correlation.

$$D_{11} < D_{22}$$

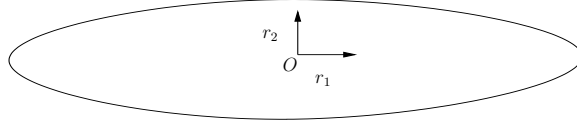


Figure 22: Schematic showing the connection of  $D_{ij}$  to the anisotropy of  $R_{ij}(\mathbf{r})$ . An isocontour of a hypothetical  $R_{kk}(\mathbf{r})$  at  $r_3 = 0$  is shown for a correlation for which  $D_{11} < D_{22}$ .

of reproducing the anisotropy of  $R_{ij}(\mathbf{r})$  in real turbulent flows. In order to ensure that the model becomes isotropic when the structure tensors are isotropic, we model in terms of the normalized anisotropies of the structure tensors instead. These anisotropic tensors are given by  $b_{ij} = \frac{B_{ij}}{q^2} - \frac{\delta_{ij}}{3}$ ,  $d_{ij} = \frac{D_{ij}}{q^2} - \frac{\delta_{ij}}{3}$  and  $Q_{ijk}^* = \frac{\tilde{Q}_{ijk}^*}{q^2}$ . Thus, we rewrite the representation as  $R_{ij}(\mathbf{r}) = q^2 F_{ij}(\mathbf{r}, \mathbf{b}, \mathbf{d}, \mathbf{Q}^*)$ , which we construct based on the following assumptions:

- We are not representing the correlation for the very small dissipative scales, i.e. we do not attempt to model the viscous healing. Therefore, we do not expect  $F_{ij}$  to be exactly equal to  $B_{ij}$  at  $r = 0$ . Instead, we let the zero separation correlation be some value  $B_{ij} + q^2 \Delta B_{ij}$
- $F_{ij}$  is assumed to be linear in its dependence on  $b_{ij}, d_{ij}$  and  $Q_{ijk}^*$ . This is consistent with the fact that the exact relationship between the structure tensors and  $R_{ij}$  is linear (eqns (141) - (143)).
- The tensor function  $F_{ij}(\mathbf{r}, \mathbf{b}, \mathbf{d}, \mathbf{Q}^*)$  is invariant to proper rotation of the reference frame as well as to changes in the handedness of the axes of the reference frame.
- The representation satisfies the symmetry  $R_{ij}(\mathbf{r}) = R_{ji}(-\mathbf{r})$ , which is exactly true for homogeneous turbulence.

We construct the most general linear representation  $F_{ij}(\mathbf{r}, \mathbf{b}, \mathbf{d}, \mathbf{Q}^*)$  using the invariant theory of tensors<sup>32</sup>, and obtain the following form for  $R_{ij}$ :

$$R_{ij}(\mathbf{r}) = B_{ij} + q^2 \left[ \Delta B_{ij} + R_{ij}^I(\mathbf{r}) + R_{ij}^b(\mathbf{r}, \mathbf{b}) + R_{ij}^d(\mathbf{r}, \mathbf{d}) + R_{ij}^Q(\mathbf{r}, \mathbf{Q}^*) \right] \quad (146)$$

where,

$$R_{ij}^I(\mathbf{r}) = f_1(r)\delta_{ij} + f_2(r)r_i r_j \quad (147)$$

$$R_{ij}^b(\mathbf{r}, \mathbf{b}) = f_3(r)b_{ij} + [f_4(r)\delta_{ij} + f_5(r)r_i r_j] \mathbf{r} \cdot \mathbf{b} \cdot \mathbf{r} + f_6(r)[r_i(\mathbf{r} \cdot \mathbf{b})_j + r_j(\mathbf{r} \cdot \mathbf{b})_i] \quad (148)$$

$$R_{ij}^d(\mathbf{r}, \mathbf{d}) = f_7(r)d_{ij} + [f_8(r)\delta_{ij} + f_9(r)r_i r_j] \mathbf{r} \cdot \mathbf{d} \cdot \mathbf{r} + f_{10}(r)[r_i(\mathbf{r} \cdot \mathbf{d})_j + r_j(\mathbf{r} \cdot \mathbf{d})_i] \quad (149)$$

$$R_{ij}^Q(\mathbf{r}, \mathbf{Q}^*) = f_{11}(r)[\epsilon_{imk}Q_{klj}^* + \epsilon_{jmk}Q_{kli}^*]r_l r_m + f_{12}(r)[r_j \epsilon_{ink} + r_i \epsilon_{jnk}]Q_{klm}^* r_l r_m r_n \quad (150)$$

Here  $f_1(r) - f_{12}(r)$  are scalar functions of  $r$ . The number of free scalar functions  $f_i(r)$  can be reduced by using the constraints mentioned in section 6.2.2.

### 6.2.2 Constraints

**The Continuity Constraint** The continuity equation for  $R_{ij}(\mathbf{r})$  in the context of homogeneous, incompressible turbulence is given by

$$\frac{\partial R_{ij}(\mathbf{r})}{\partial r_j} = 0 \quad (151)$$

We get the following constraints by substituting eqn (146) into eqn (151), and equating the coefficients of linearly independent vectors involving  $\mathbf{r}$  and the structure tensors to zero:

$$f'_1 + r^2 f'_2 + 4r f_2 = 0 \quad (152)$$

$$f'_4 + 6r f'_5 + r^2 f'_5 + f'_6 = 0 \quad (153)$$

$$2r f_4 + f'_3 + 5r f_6 + r^2 f'_6 = 0 \quad (154)$$

$$f'_8 + 6r f_9 + r^2 f'_9 + f'_{10} = 0 \quad (155)$$

$$2r f_8 + f'_7 + 5r f_{10} + r^2 f'_{10} = 0 \quad (156)$$

$$r^2 f'_{12} + 7r f_{12} + f'_{11} = 0 \quad (157)$$

After the imposition of the continuity constraint,  $\mathbf{R}^I$  and  $\mathbf{R}^Q$  have one unconstrained scalar function left while  $\mathbf{R}^b$  and  $\mathbf{R}^d$  each have two unconstrained scalar functions left.

**The Self-Consistency Constraint** When we evaluate the structure tensors by substituting the representation given by eqn (146) into the right hand side of eqns (147)-(150), we get a set of equations where  $\mathbf{B}$ ,  $\mathbf{D}$ ,  $\tilde{\mathbf{Q}}^*$  are related to a sum of integrals of the parts of the representation given by  $R_{ij}^I$ ,  $R_{ij}^b$ ,  $R_{ij}^d$  and  $R_{ij}^Q$ . We would like a self-consistency condition where when a structure tensor is evaluated from the representation, it should have contributions from only parts of the representation relevant to that structure tensor. More precisely, when a structure tensor is zero, we would like the same structure tensor evaluated from the representation to be zero. Most of the equations obtained from these constraints are identically true due to the inherent symmetries in the representation. The only equations which are not satisfied identically are the ones obtained by equating to zero the contribution of  $R_{ij}^d$  to  $B_{ij}$  in eqn (142) and the contribution of  $R_{ij}^d$  to  $B_{ij}$  in eqn (143):

$$\frac{1}{4\pi} \int_V \frac{1}{r} \frac{\partial^2 R_{ij}^d(\mathbf{r}, \mathbf{d})}{\partial r_k \partial r_k} d\mathbf{r} = 0 \quad (158)$$

$$\frac{1}{4\pi} \int_V \frac{1}{r} \frac{\partial^2 R_{kk}^b(\mathbf{r}, \mathbf{b})}{\partial r_i \partial r_j} d\mathbf{r} = 0 \quad (159)$$

These integral constraints are not strong enough for the small separation correlations, because the integral does not have to be zero when it is taken over finite volumes contained in  $V$ . We are



interested in using these correlations for LES modeling, and are therefore interested in obtaining a representation of the correlation for only small values of  $r$ . Thus, we apply a stronger constraint where we require that the angular integral of the integrands in eqns (158)-(159) are equated to zero:

$$\frac{1}{4\pi} \oint \frac{\partial^2 R_{ij}^d(\mathbf{r}, \mathbf{d})}{\partial r_k \partial r_k} d\angle = 0 \quad (160)$$

$$\frac{1}{4\pi} \oint \frac{\partial^2 R_{kk}^b(\mathbf{r}, \mathbf{b})}{\partial r_i \partial r_j} d\angle = 0 \quad (161)$$

Where  $d\angle = \sin\theta d\theta d\phi$  and  $(r, \theta, \phi)$  are the standard spherical coordinates. Performing the above integrals<sup>5</sup>, we obtain:

$$\frac{2b_{ij}}{15}(15g + 9rg' + r^2g'' + 35r^2f_5 + 13r^3f_5' + r^4f_5'') = 0 \quad (162)$$

$$\begin{aligned} \frac{d_{ij}}{15}(30f_7'/r + 15f_7'' + 40r^2f_9 + 20r^3f_9' + 2r^4f_9'' \\ + 60f_{10} + 60rf_{10}' + 10r^2f_{10}'') = 0 \end{aligned} \quad (163)$$

where  $g = 3f_4 + 2f_6$ .

### 6.2.3 Power law model for $f_i(r)$

The continuity and consistency constraints arise separately from the different parts of the correlation, and the scalar functions are accordingly decoupled from each other. Examining eqns (152)-(157) and eqns (162)-(163) we see that it is possible to break up the set of scalar functions into four subsets such that the constraints do not relate functions which do not belong to the same subset. These subsets are given by  $\{f_1, f_2\}$ ,  $\{f_3, f_4, f_5, f_6\}$ ,  $\{f_7, f_8, f_9, f_{10}\}$ ,  $\{f_{11}, f_{12}\}$ . We now postulate that these functions have a power law representation, with the rationale that it has the ability to reduce to the  $r^{2/3}$  power law for isotropic turbulence. Also, for homogeneous turbulence, dependence of the anisotropic part of the correlation on a power law of  $r$  has been proposed theoretically<sup>31</sup> and reported experimentally<sup>33</sup> in the past. In order to satisfy the constraints in a nontrivial way, the scalar functions belonging to the same subset need to have the same power law, corrected by an appropriate integral power of  $r$ . For instance, if we assume  $f_1 = a_1 r^{\gamma_1}$  and  $f_2 = a_2 r^{\gamma_2}$ , then eqn (152) yields:

$$a_1 \gamma_1 r^{\gamma_1-1} + 5a_2 r^{\gamma_2+1} = 0 \quad (164)$$

If  $\gamma_1 - 1 \neq \gamma_2 + 1$  then  $a_1 = a_2 = 0$  for  $r \neq 0$ . On the other hand, requiring  $\gamma_1 = \gamma_2 + 2$  yields the constraint  $\gamma_1 a_1 + 5a_2 = 0$ . Following a similar procedure for all the constraints, we obtain the form  $f_i(r) = a_i r^{z[i] + \alpha_n}$ , where  $z[i]$  are integers, and  $\alpha_1 - \alpha_4$  are the independent power-law indices corresponding to each group. These power-law forms of  $f_i(r)$  are then substituted into the constraints, given by eqns (152)-(157) and eqns (162)-(163) to yield 8 equations for 12  $a_i$ 's (6.4). Therefore there can be only four independent  $a_i$ 's, which we choose to be  $a_1, a_3, a_7$  and  $a_{11}$ .

---

<sup>5</sup>We have used the identities  $I_{ij}^2 = \frac{1}{4\pi} \oint r_i r_j d\angle = \frac{r^2 \delta_{ij}}{3}$  and  $I_{ijkl}^4 = \frac{1}{4\pi} \oint r_i r_j r_k r_l d\angle = \frac{r^4}{15}(\delta_{ij}\delta_{kl} + \delta_{ik}\delta_{jl} + \delta_{il}\delta_{jk})$  to derive eqns (162)-(163)

Given a set of indices  $\alpha_1 - \alpha_4$ , the ratios of the rest of the coefficients with respect to these four coefficients are fixed. Thus we can rewrite eqns (147)-(150) as:

$$\begin{aligned}
\Delta R_{ij}(\mathbf{r}) &= \frac{R_{ij}(\mathbf{r}) - B_{ij}}{q^2} = \Delta B_{ij} + a_1 r^{\alpha_1} \left[ r^2 \delta_{ij} + \frac{a_2}{a_1} r_i r_j \right] \\
&+ a_3 r^{\alpha_2} \left\{ r^4 b_{ij} + \left[ \frac{a_4}{a_3} \delta_{ij} r^2 + \frac{a_5}{a_3} r_i r_j \right] \mathbf{r} \cdot \mathbf{b} \cdot \mathbf{r} + \frac{a_6}{a_3} r^2 [r_i (\mathbf{r} \cdot \mathbf{b})_j + r_j (\mathbf{r} \cdot \mathbf{b})_i] \right\} \\
&+ a_7 r^{\alpha_3} \left\{ r^4 d_{ij} + \left[ \frac{a_8}{a_7} \delta_{ij} r^2 + \frac{a_9}{a_7} r_i r_j \right] \mathbf{r} \cdot \mathbf{d} \cdot \mathbf{r} + \frac{a_{10}}{a_7} r^2 [r_i (\mathbf{r} \cdot \mathbf{d})_j + r_j (\mathbf{r} \cdot \mathbf{d})_i] \right\} \\
&+ a_{11} r^{\alpha_4} \left\{ [\epsilon_{imk} Q_{klj}^* + \epsilon_{jmk} Q_{kli}^*] r_l r_m \right. \\
&\left. + \frac{a_{12}}{a_{11}} \frac{[r_j \epsilon_{ink} + r_i \epsilon_{jnk}] Q_{klm}^* r_l r_m r_n}{r^2} \right\}
\end{aligned} \tag{165}$$

The above relation implies that if we fix  $\{\Delta \mathbf{B}, \mathbf{b}, \mathbf{d}, \mathbf{Q}^*\}$  then there are 8 degrees of freedom (dof) in the representation, given by  $\alpha_1 - \alpha_4$  and  $a_1, a_3, a_7, a_{11}$ .

## 6.3 Fitting the representation to DNS correlations

### 6.3.1 Optimization algorithm

In order to check the usefulness of the representation, we construct a model  $R_{ij}^{\text{Model}}$  by evaluating the best fit of the representation with respect to the correlation tensor calculated from DNS of anisotropic turbulent flows,  $R_{ij}^{\text{DNS}}$ . For calculating the best fit we fix  $q^2$  and  $b_{ij}$  by using the value directly from DNS, since they are easily obtained from the data. We do not explicitly vary  $a_7$  and  $a_{11}$ , and instead absorb them into  $d_{ij}$  and  $Q_{ijk}^*$ . Thus the optimal values of  $d_{ij}$  and  $Q_{ijk}^*$  will be correct to some constant factor. The search space for obtaining the optimal fit is given by the set of variables  $\{\Delta \mathbf{B}, a_1, a_3, \mathbf{d}, \mathbf{Q}^*, \mathbf{p}\}$ , where  $\mathbf{p} = (\alpha_1 + 2, \alpha_2 + 4, \alpha_3 + 4, \alpha_4 + 4)$  is the four dimensional vector of power law indices. The best fit is obtained by minimizing the  $L^2$  norm of the error between the DNS correlation and the model correlation. This error is given by

$$E(\Delta \mathbf{B}, a_1, a_3, \mathbf{d}, \mathbf{Q}^*, \vec{\alpha}) = \|\Delta \mathbf{R}^{\text{DNS}} - \Delta \mathbf{R}^{\text{Model}}\|^2 \tag{166}$$

where

$$\|\mathbf{T}(\mathbf{r})\|^2 = \langle \mathbf{T} | \mathbf{T} \rangle \tag{167}$$

$$\text{and } \langle \mathbf{S} | \mathbf{T} \rangle = \int_{V'} S_{ij}(\mathbf{r}) T_{ij}(\mathbf{r}) d\mathbf{r} \tag{168}$$

$S_{ij}(\mathbf{r}), T_{ij}(\mathbf{r})$  being tensor fields and  $V' \subset \mathbb{R}^3$  having finite volume.  $V'$  needs to have finite volume since our model for  $R_{ij}(\mathbf{r})$  does not decay to zero for large  $r$  and therefore the error norm  $E$  depends implicitly on our choice of the volume  $V'$ . We will however perform our error minimization over a fixed  $V'$ , which will be chosen over an appropriate inertial range. For performing the minimization, we take advantage of the fact that the dependence of  $\Delta \mathbf{R}^{\text{Model}}$  on  $\{\Delta \mathbf{B}, a_1, a_3, \mathbf{d}, \mathbf{Q}^*\}$  is linear, which allows to use a two step approach. In the first step, we use least squares minimization to obtain the minimum  $E$  for a given  $\mathbf{p}$ , i.e. we obtain  $E'(\mathbf{p}') =$

$E(\Delta\mathbf{B}, a_1^0, a_3^0, \mathbf{d}^0, \mathbf{Q}^{*0}, \mathbf{p}')$  such that for a fixed  $\mathbf{p}'$ , the values  $\Delta\mathbf{B}^0$ ,  $a_1^0, a_3^0, \mathbf{d}^0$  and  $\mathbf{Q}^{*0}$  are the solutions to  $\partial E / \partial \Delta B_{ij} = 0$ ,  $\partial E / \partial a_1 = 0$ ,  $\partial E / \partial a_3 = 0$ ,  $\partial E / \partial d_{ij} = 0$  and  $\partial E / \partial Q_{ijk}^* = 0$  respectively. If the flow does not contain any symmetries (other than homogeneity), then this step involves optimization over 20 variables<sup>6</sup>. In the second step, we minimize  $E'(\mathbf{p})$  over  $\{\mathbf{p}; p_i \in [-1 + c_0, \infty], i = 1, 2, 3, 4\}$ <sup>7</sup>, where  $c_0$  is a small positive constant, chosen to be 0.03 in our case. The second step is carried out using the PRAXIS optimization software package, which is based on 'Brent's method'<sup>34</sup>. If  $\mathbf{p} = \mathbf{p}_{\min}$  is the exact minima for  $E'(\mathbf{p})$ , then the settings in the PRAXIS software ensure that the optimal  $\mathbf{p}$  is calculated within an error  $\epsilon = 0.01$  of  $\mathbf{p}_{\min}$ .

### 6.3.2 Results for homogeneous turbulence

The first fit of our representation is done with respect to correlations constructed from the DNS velocity field of an initially isotropic and homogeneous turbulent flow subjected to mean shear  $\langle u_{i,j} \rangle = \delta_{i1}\delta_{j2}S$ . The details of the DNS can be found in<sup>35</sup>. Some of the relevant details of the field used are given in table 5. The volume over which the fit is performed is given by the spherically symmetric annulus  $V' = \{\mathbf{r}; 0.26 < r < 0.6\}$ , where the lower and upper limit of  $r$  correspond to the Taylor micro-scale and the integral length scale respectively. Due to the symmetries in the flow, several components of  $\{\Delta\mathbf{B}, \mathbf{d}, \mathbf{Q}^*\}$  are identically zero, resulting, for a fixed  $\mathbf{p}$ , in 12 degrees of freedom in the representation. The relative error obtained between the best fit and the DNS correlation, given by  $\|\Delta\mathbf{R}^{\text{Model}} - \Delta\mathbf{R}^{\text{DNS}}\| / \|\Delta\mathbf{R}^{\text{DNS}}\|$  is 10%. A more qualitative comparison is done in figure 23, where we have chosen to show the isocontours of  $r_3 = 0$  because the correlations have the least symmetry in this plane.

We take note of two major differences between the model and the DNS. Firstly, the isocontours of  $\Delta R_{22}$  in the model have a different shape when compared with that of the DNS. This occurs because the Reynolds stress  $R_{22}(0)$  is much smaller than the other normal Reynolds stress components (table 5), and therefore this component does not get as good a fit as the other components. Secondly, we notice that the isocontours of  $R_{11}^{\text{Model}}$  are not as elongated as the isocontours of  $R_{11}^{\text{DNS}}$  in the streamwise direction. The elongation in  $R_{11}^{\text{DNS}}$  happens due to the fact that the high mean shear picks out the streamwise axis of the isocontours of the  $R_{11}$  component to grow at a faster rate compared to other components<sup>36</sup>. However, the volume  $V'$  over which the best fit is conducted is spherically symmetric, and therefore tries to fit the same power law functions upto an equal extent in all directions. This causes the fall-off in the correlation to get averaged over all directions and components, and thus the excessive elongation in the streamwise direction for  $R_{11}$  does not get properly captured.

On the other hand, we also observe that for  $r \in V'$ , the isocontours of the model and DNS correlations seem to have their principle axes inclined by the same amounts for all the components (i.e. except  $R_{22}$ ). Also, specific details of the isocontours of each component (e.g. the elliptic

<sup>6</sup>The 20 variables arise after taking into account the symmetries of the tensors in the search space. There are 6 independent components in  $\Delta B_{ij}$ , which has the symmetry  $\Delta B_{ij} = \Delta B_{ji}$ , 1 component each from  $a_1$  and  $a_3$ , 5 independent components from  $d_{ij}$  which has the symmetries  $d_{ij} = d_{ji}$  and  $d_{kk} = 0$ , 7 independent components from  $Q_{ijk}^*$ , which is invariant to any permutations in it's indices and has the symmetry  $Q_{ikk}^* = 0$

<sup>7</sup>The lower limit of  $\mathbf{p}$  is needed to ensure that while performing least square error minimization, inner products amongst tensor components of the form given in eqn (168) do not diverge. That is,  $\forall \mathbf{r} \in V'$ ,  $r^2 \oint S_{ij}(\mathbf{r})S_{ij}(\mathbf{r})d\mathcal{L} = O(1)$  and  $r^2 \oint T_{ij}(\mathbf{r})T_{ij}(\mathbf{r})d\mathcal{L} = O(1) \Rightarrow r^2 \oint S_{ij}(\mathbf{r})T_{ij}(\mathbf{r})d\mathcal{L} = O(1)$  (from the fact that  $(\mathbf{S}, \mathbf{T}) = \oint S_{ij}(\mathbf{r})T_{ij}(\mathbf{r})d\mathcal{L}$  is also an inner product and the Cauchy-Schwartz inequality)

Table 5: Specifics of the homogeneous turbulent field (MKS units)

Resolution	$256^3$
Box Size ( $l_x \times l_y \times l_z$ )	$2\pi \times 2\pi \times 2\pi$
Integral length scale $L$ ( $3\pi \times \int k^{-1} E(k) dk / \int E(k) dk$ )	0.6
Taylor length scale $\lambda$	0.26
rms velocity ( $q$ )	6.37
$(\langle u'_1 u'_1 \rangle, \langle u'_1 u'_1 \rangle, \langle u'_2 u'_2 \rangle, \langle u'_3 u'_3 \rangle)$	(26.12, -5.69, 5.55, 8.92)
$Re_\lambda$ at $St = 0$ (i.e. of initially isotropic field)	45.35
$Sq^2/\epsilon$ at $St = 0$	35.85

isocontours for the normal components and the dual-lobed shape of the isocontours of  $R_{12}(\mathbf{r})$  are captured well by the model.

Ideally, we would also like to compare the values of the structure functions calculated from the DNS and Model correlations using eqns (141)-(143). However, the model assumes a power law dependence for  $r$ , and is therefore not valid for all  $\mathbf{r} \in \mathbb{R}^3$  (specifically for  $r$  much smaller than the Taylor micro-scale and much larger than the integral scales). Instead, we define a scale-dependent dimensionality tensor  $D'_{ij}(r_0, r)$  given by:

$$D'_{ij}(r_0, r) = \frac{1}{4\pi} \int_{V''(r_0, r)} \frac{1}{r'} \frac{\partial^2 R_{kk}(\mathbf{r}')}{\partial r'_i \partial r'_j} d\mathbf{r}' \quad (169)$$

Where  $V''(r_0, r) = \{\mathbf{r}'; r_0 < r' < r\}$ . From figure 24 we see that there is excellent agreement for  $D'(\lambda, r)$  for  $\lambda < r < L$ . Thus, our model, supplemented with a good model for  $R_{ij}$  at very large and very small separations will ensure that we can obtain correct values of  $D_{ij}$  from the correlation.

### 6.3.3 Results for turbulent channel flow

The second set of correlations used to fit our representation were calculated from DNS fields of fully developed turbulent channel flow at  $Re_\tau = 940$ . Unlike the previous case this is a highly inhomogeneous flow and we try to examine the extent to which our homogeneous representation will be valid. The main reason to carry out this exercise is to find out whether the tensors forms in eqns (147)-(150) need to depend on any additional tensors due to the presence of inhomogeneity.

The only direction of inhomogeneity is the one perpendicular to the channel wall. The  $x$  axis is aligned in the streamwise direction and the  $y$  axis is aligned in the direction of inhomogeneity. Therefore the correlation will be redefined as  $R_{ij}(y, \mathbf{r}) = \langle u'_i(\mathbf{x}) u'_j(\mathbf{x} + \mathbf{r}) \rangle|_{x_2=y}$ . Our model does not satisfy the continuity equation<sup>8</sup> or the symmetry of the correlation<sup>9</sup> exactly, but for small  $r/y$  values we expect the effects of inhomogeneity to be small and we will assume that  $R_{ij}(y, \mathbf{r})$  is locally homogeneous at  $y$ . This of course implies that all our fitting parameters are functions of  $y$ .

After performing the best fit optimization, we found the relative error between our model and the fit to be 6%. Figure 25 shows that the model fits the data quite well for the reference  $y^+ = 220$

<sup>8</sup>Given by  $\left(\frac{\partial}{\partial y} \delta_{i2} - \frac{\partial}{\partial r_i}\right) R_{ij}(y, \mathbf{r}) = \frac{\partial}{\partial r_j} R_{ij}(y, \mathbf{r}) = 0$

<sup>9</sup> $R_{ij}(y, \mathbf{r}) = R_{ji}(y + r_2, -\mathbf{r})$

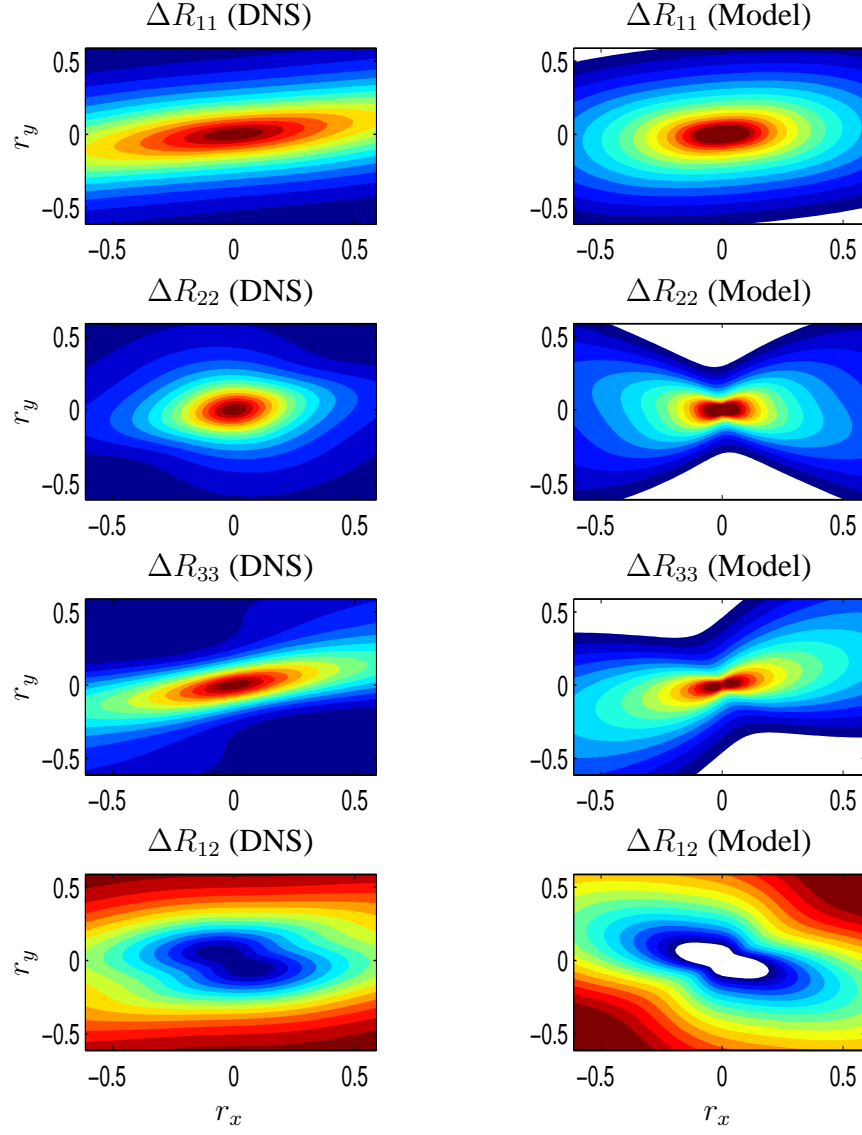


Figure 23: Isocontours of  $\Delta R_{ij}(\mathbf{r}) = R_{ij}(\mathbf{r}) - R_{ij}(0)$ , plotted for  $r_z = 0$ . The correlations in the left column were calculated from DNS of homogeneous shear flow, and the correlation in the right column from the best fit of the model with DNS. The contour levels for given a correlation component (i.e. for the same row) have the same range.

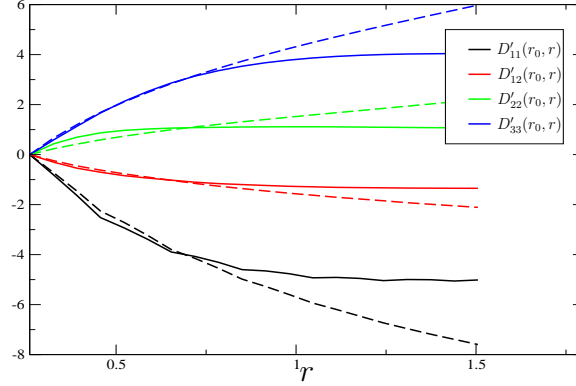


Figure 24: Comparison of  $D'_{ij}(r_0, r) = \frac{1}{4\pi} \int_{V''(r_0, r)} \frac{1}{r'} \frac{\partial^2 R_{kk}(\mathbf{r}')}{\partial r'_i \partial r'_j} d\mathbf{r}'$ , where  $V''(r_0, r) = \{\mathbf{r}'; r_0 < r' < r\}$ . Here  $r_0 = \lambda = 0.26$ , and  $D'_{ij}$  has calculated from both model (dashed lines) and DNS (bold lines).

location in the log layer. The inclination of principle axes are well captured and the magnitude of the contour levels match. The main shortcoming of our model lies in it's inability to capture the effects of inhomogeneity, which is best seen in the  $R_{12}$  component, where the isocontours of the DNS extend out further in the positive  $r_2$  half of the plane as compared to the negative  $r_2$  half due to the presence of the wall. Our model on the other hand is symmetric in  $\mathbf{r}$ , and is not able to capture this aspect of the data, which points to the need for further improvements in the representation.

## 6.4 Conclusions

A finite dimensional representation of the two point correlation tensor was constructed using the invariant theory of tensors. A novel approach was taken in this work, where the representation depended upon structure tensors. Despite being single-point moments, these tensors capture the extent and orientation of the elongation of  $R_{kk}$  for values of  $r$  of the order of the integral scale of the correlation. Our representation depended linearly on the structure tensors, and we were able to significantly reduce the number of degrees of freedom in our model using the continuity and self consistency constraints. A power-law dependence on  $r$  was assumed in the model, which prevented us from modeling the dissipative range and the large-separation range. In order to fit the correlation to the DNS data, we had to allow the Reynolds stress of the model to be a degree of freedom for our fit. The results show that our model fits the correlations calculated from DNS data well both quantitatively and qualitatively, and that complemented with a model for the large-separation and dissipative range separation, one could extract the structure tensors from experimental and numerical measurements of  $R_{ij}$  by fitting it to our model. In fact this model enables us to construct good reconstruction of  $R_{ij}$  using a finite number of data points, which can be potentially useful for OLES formulations, where information about the correlation is required from a finite dimensional field. However, the model does require a variety of improvements, most urgent being the need to model dissipative range and large-separation range of  $R_{ij}$ , and constructing a representation for the anisotropy which is valid for inhomogenous flows.

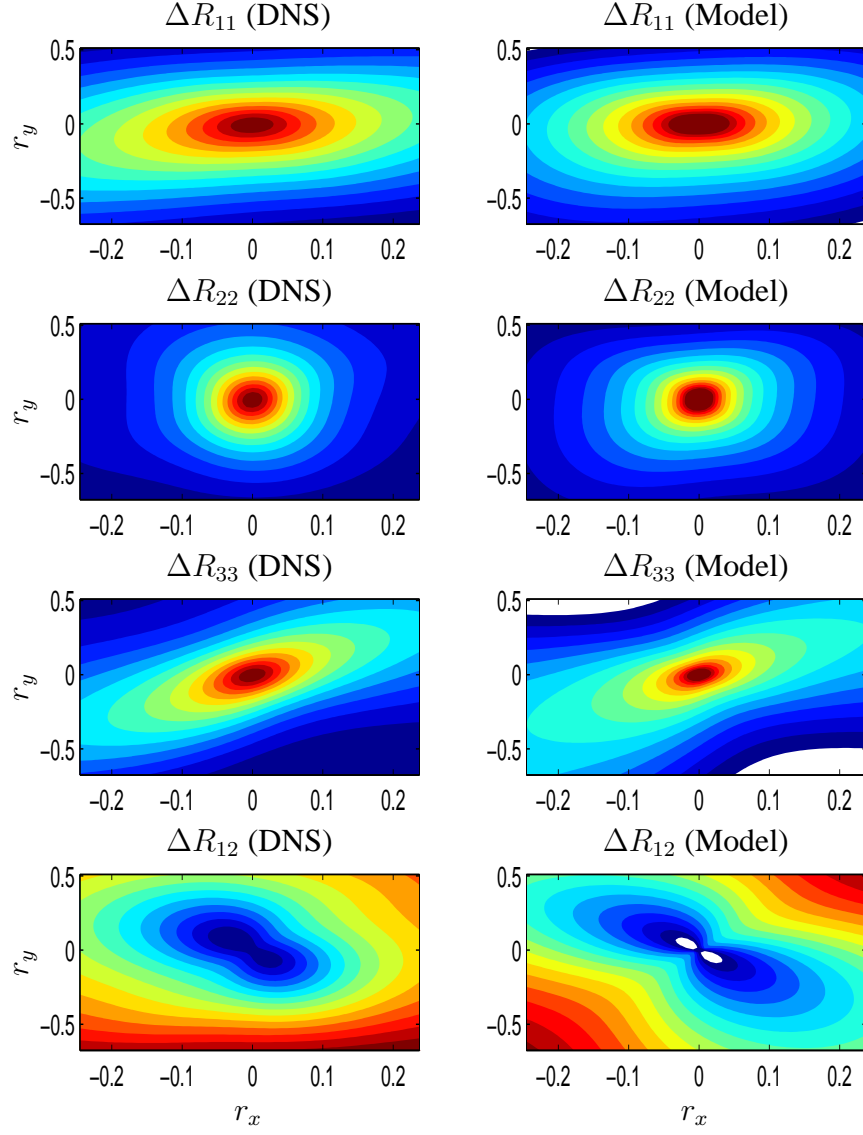


Figure 25: Isocontours of  $\Delta R_{ij}(y, \mathbf{r}) = R_{ij}(y, \mathbf{r}) - R_{ij}(y, 0)$  at  $y^+ = Re_\tau y/h = 220$ , plotted for  $r_z = 0$ . The correlations in the left column were calculated from DNS of channel flow, and the correlation in the right column from the best fit of the model with DNS. The contour levels for given a correlation component (i.e. for the same row) have the same range.

## Constraints arising from $f_i(r) \approx r^{z[i]+\alpha_n}$

In section 6.2.3 it was observed that the set of functions  $\{f_i(r)\}$  can be divided into four disjoint subsets, according to the set of constraints satisfied by them. These subsets are given by  $\{f_1, f_2\}$ ,  $\{f_3, f_4, f_5, f_6\}$ ,  $\{f_7, f_8, f_9, f_{10}\}$ ,  $\{f_{11}, f_{12}\}$ . Assuming a power law form  $f_i(r) = a_i r^{\gamma_i}$ , it is then necessary for  $\gamma_i$ 's to have a form so that every term in a given constraint equation has the same power of  $r$  (otherwise we get the solution  $a_i = 0$  for all  $i$ 's). We choose  $f_i$ 's to have the form:

$$f_1 = a_1 r^{2+\alpha_1} \quad f_2 = a_2 r^{\alpha_1} \quad (170)$$

$$f_3 = a_3 r^{4+\alpha_2} \quad f_4 = a_4 r^{2+\alpha_2} \quad f_5 = a_5 r^{\alpha_2} \quad f_6 = a_6 r^{2+\alpha_2} \quad (171)$$

$$f_7 = a_7 r^{4+\alpha_3} \quad f_8 = a_8 r^{2+\alpha_3} \quad f_9 = a_9 r^{\alpha_3} \quad f_{10} = a_{10} r^{2+\alpha_3} \quad (172)$$

$$f_{11} = a_{11} r^{2+\alpha_4} \quad f_{12} = a_{12} r^{\alpha_4} \quad (173)$$

Substituting the forms of  $f_1 - f_{12}$  in eqns (170)-(173) into eqns (152)-(157) and eqns (162)-(163) we get the following set of linear equations for  $a_1 - a_{12}$ :

$$\begin{aligned} a_1(2 + \alpha_1) + a_2(4 + \alpha_1) &= 0 \\ a_4(2 + \alpha_2) + a_6(2 + \alpha_2) + a_5(6 + \alpha_2) &= 0 \\ 2a_4 + a_3(4 + \alpha_2) + a_6(7 + \alpha_2) &= 0 \\ 3a_4 + a_5 + 2a_6 &= 0 \\ a_8(2 + \alpha_3) + a_{10}(2 + \alpha_3) + a_9(6 + \alpha_3) &= 0 \\ 2a_8 + a_7(4 + \alpha_3) + a_{10}(7 + \alpha_3) &= 0 \\ (15a_7 + 2(a_9 + 5a_{10}))(4 + \alpha_3)(5 + \alpha_3) &= 0 \\ a_{11}(2 + \alpha_4) + a_{12}(7 + \alpha_4) &= 0 \end{aligned} \quad (174)$$

Choosing  $a_1, a_3, a_7, a_{11}$  to be the independent coefficients, the ratios of the remaining coefficients with respect to the four independent coefficients become fixed, and are given as follows:

$$\frac{a_2}{a_1} = -\frac{(2 + \alpha_1)}{(4 + \alpha_1)}, \quad \frac{a_4}{a_3} = \frac{1}{2} \left( 1 - \frac{6}{(46 + \alpha_2(14 + \alpha_2))} \right) \quad (175)$$

$$\frac{a_5}{a_3} = \frac{(2 + \alpha_2)(4 + \alpha_2)}{2(46 + \alpha_2(14 + \alpha_2))}, \quad \frac{a_6}{a_3} = -\frac{(4 + \alpha_2)(8 + \alpha_2)}{(46 + \alpha_2(14 + \alpha_2))} \quad (176)$$

$$\frac{a_8}{a_7} = \left( \frac{7}{2} - \frac{6}{(10 + \alpha_3)} \right), \quad \frac{a_9}{a_7} = \frac{-5(2 + \alpha_3)}{2(10 + \alpha_3)} \quad (177)$$

$$\frac{a_{10}}{a_7} = -\frac{(14 + \alpha_3)}{(10 + \alpha_3)}, \quad \frac{a_{12}}{a_{11}} = -\frac{(2 + \alpha_4)}{(7 + \alpha_4)} \quad (178)$$

As long as the denominators of eqns (175)-(178) do not vanish<sup>10</sup>, the ratios of coefficients are uniquely determined. From section 6.3.1 we know that the search space for  $\mathbf{p} = (\alpha_1 + 2, \alpha_2 + 4, \alpha_3 + 4, \alpha_4 + 4)$  is given by  $\{\mathbf{p}; p_i \in [-1 + c_0, \infty], i = 1, 2, 3, 4\}$ , where  $c_0 = 0.03$ . Therefore none of the roots of the denominators of eqns (175)-(178) are within the range of the search space.

<sup>10</sup>This is true if  $\alpha_1 \neq -4, \alpha_2 \neq -7 \pm \sqrt{3}, \alpha_3 \neq -10, \alpha_4 \neq -7$



## 7 Testing and Evaluation of the Filtered Wall Formulation for the Wall-Layer

One of the pacing problems in the development of reliable large eddy simulation (LES) models for use in turbulent flows of technological interest is the so-called LES wall-modeling problem<sup>37</sup>. It arises because the length-scale associated with the wall layer of a turbulent wall-bounded shear flow (wall units) gets smaller relative to the shear layer thickness approximately like the inverse Reynolds number (like  $Re_\tau^{-7/8}$  in the channel flow). The “large-scale” turbulence in this thin layer also scales in wall units. If the cost of an LES of wall-bounded flows is to remain finite in the limit of infinite Reynolds number, then this wall layer and the large-scale turbulence it supports cannot be represented directly, and so must be modeled. However, current LES models are generally not valid for this near-wall layer because underlying assumptions such as small-scale homogeneity and isotropy are not valid. The alternative is to resolve the near-wall turbulence. The most successful LES of wall-bounded shear flows employ this technique, though this is clearly not viable for arbitrarily large Reynolds number. In this paper, we propose a possible solution to this wall-modeling problem.

Our approach is motivated by the observation that in an LES, locating anything, including the wall, to more precision than the filter width is inconsistent with the representation. This leads us to a formulation in which the wall is filtered as well as the turbulence. This allows the use of homogeneous or nearly homogeneous filters normal to the wall, avoiding commutation error. Also, the the dynamics of the sublayer can be effectively filtered out, which we will see is advantageous. Filtering the wall, however, also introduces an extra term in the filtered equations which must be modeled, along with the usual subgrid stress term. A modeling approach for this extra term is proposed here.

To allow the filtered boundary approach to be evaluated with minimum uncertainty arising from the subgrid stress model, optimal LES models will be used<sup>1,8,26,28</sup>. In optimal LES, the subgrid force term (or the subgrid stress) is approximated using stochastic estimation. Optimal LES is a formal approximation to what we have called the ideal LES evolution<sup>1</sup>, which can be shown to produce one-time statistics that are exact, and minimum mean-square variation in the instantaneous large-scale evolution. The optimal LES formalism has the advantage in this context of being valid even in the absence of small-scale isotropy or homogeneity; that is, it is valid for near-wall turbulence. As input, optimal LES requires detailed two-point correlation data. For the purposes of testing the viability of the proposed wall-modeling approach, this data has been obtained from the direct numerical simulation data of Moser *et al*<sup>38</sup>.

In the remainder of this paper, the filtered boundary formulation is introduced and a test of it’s capabilities is presented. The optimal LES models used here are briefly described. The results of filtered boundary LES of the turbulent channel at  $Re_\tau = 590$  are then presented followed by a brief discussion of the implications of these results, particularly the properties of the subgrid stress model needed in this formulation.

## 7.1 Filtered Wall Formulation

In the filtered boundary LES formulation, the wall-bounded domain is embedded in a larger domain, with the Navier-Stokes equations applied to the interior, and  $\mathbf{u} = 0$  applied to the exterior domains. However, since  $\mathbf{u} = 0$  is a solution to the Navier-Stokes equations, we can also extend Navier-Stokes into the exterior domain, with the wall boundary supporting a stress discontinuity just sufficient to maintain  $\mathbf{u} = 0$  in the exterior. A filter is then applied to this larger domain. The resulting filtered equations are then:

$$\frac{\partial \tilde{u}_i}{\partial t} + \frac{\partial \tilde{u}_j \tilde{u}_i}{\partial x_j} = -\frac{\partial \tilde{p}}{\partial x_i} + \frac{1}{Re} \frac{\partial \tilde{u}_i}{\partial x_j \partial x_j} + b_i + M_i \quad (179)$$

where  $M_i = -\partial \tau_{ij} / \partial x_i$  is the usual LES model term and  $b_i$  is the boundary term. The subgrid stress is given by  $\tau_{ij} = \tilde{u}_i \tilde{u}_j - \widetilde{u_i u_j}$  and the boundary term ( $b_i$ ) can be written

$$b_i(\mathbf{x}) = \int_{\partial R} \sigma_{ij}(\mathbf{x}') n_j G(\mathbf{x} - \mathbf{x}') d\mathbf{x}'$$

where  $\sigma$  is the stress at the boundary, including pressure and viscous stress,  $\partial R$  is the boundary of the fluid region  $R$  and  $n_j$  is the unit normal to the surface. If a sufficiently fine filter width is used then  $M_i$  is negligible and the only effect is the filtering of the boundary (i.e. a filtered boundary “DNS”). Such a “DNS” was used as a test case (see below). In many LES of wall bounded flows, approximate boundary conditions are used to model the effect of the wall layer<sup>39</sup>. The approximate boundary conditions are prescribed in terms of the wall shear stress, so wall stresses must be determined in terms of the resolved velocities. In the present formulation, the unfiltered wall stresses are also required, and for analogous reason.

In the current description, in which the unfiltered velocity is zero in the buffer domain external to the walls, the wall stress is the surface forcing required to ensure that momentum and energy are not transferred to the buffer domain. That is, that the velocity remains zero. This suggests a technique for determining the wall stress. It would be inappropriate to define a force to make the velocity zero at the boundary as in embedded boundary numerical methods<sup>40,41</sup>, since the filtered velocity is not zero at the wall. Instead, we choose  $\sigma_{wall}$  to minimize the transport of momentum to the exterior domain. To this end, the wall stresses at each time step are defined by minimizing

$$E = \int_B |\tilde{\mathbf{u}}|^2 + \alpha \left| \frac{\partial \tilde{\mathbf{u}}}{\partial t} \right|^2 d\mathbf{x} \quad (180)$$

where the integral is over the buffer domain. The  $|\tilde{\mathbf{u}}|^2$  term forces the energy in the buffer domain to be small, and the  $\alpha \left| \frac{\partial \tilde{\mathbf{u}}}{\partial t} \right|^2$  term ensures that large errors are not incurred in the stress to instantaneously correct small errors in the buffer domain. The constant  $\alpha$  controls the balance between these two competing requirements and is set to a value of order  $\Delta t^2$ .

In this paper, we consider turbulent flow in a channel and apply a Fourier cut-off filter and Fourier spectral method in all three spatial directions. In this case, the minimization of  $E$  required to determine the wall stress  $\sigma$  is straight forward since it can be done independently for each  $(k_x, k_z)$  wavenumber, resulting in a 6-parameter optimization in  $(\sigma_{xy}, \sigma_{yy}, \sigma_{zy})$ <sup>42</sup>.

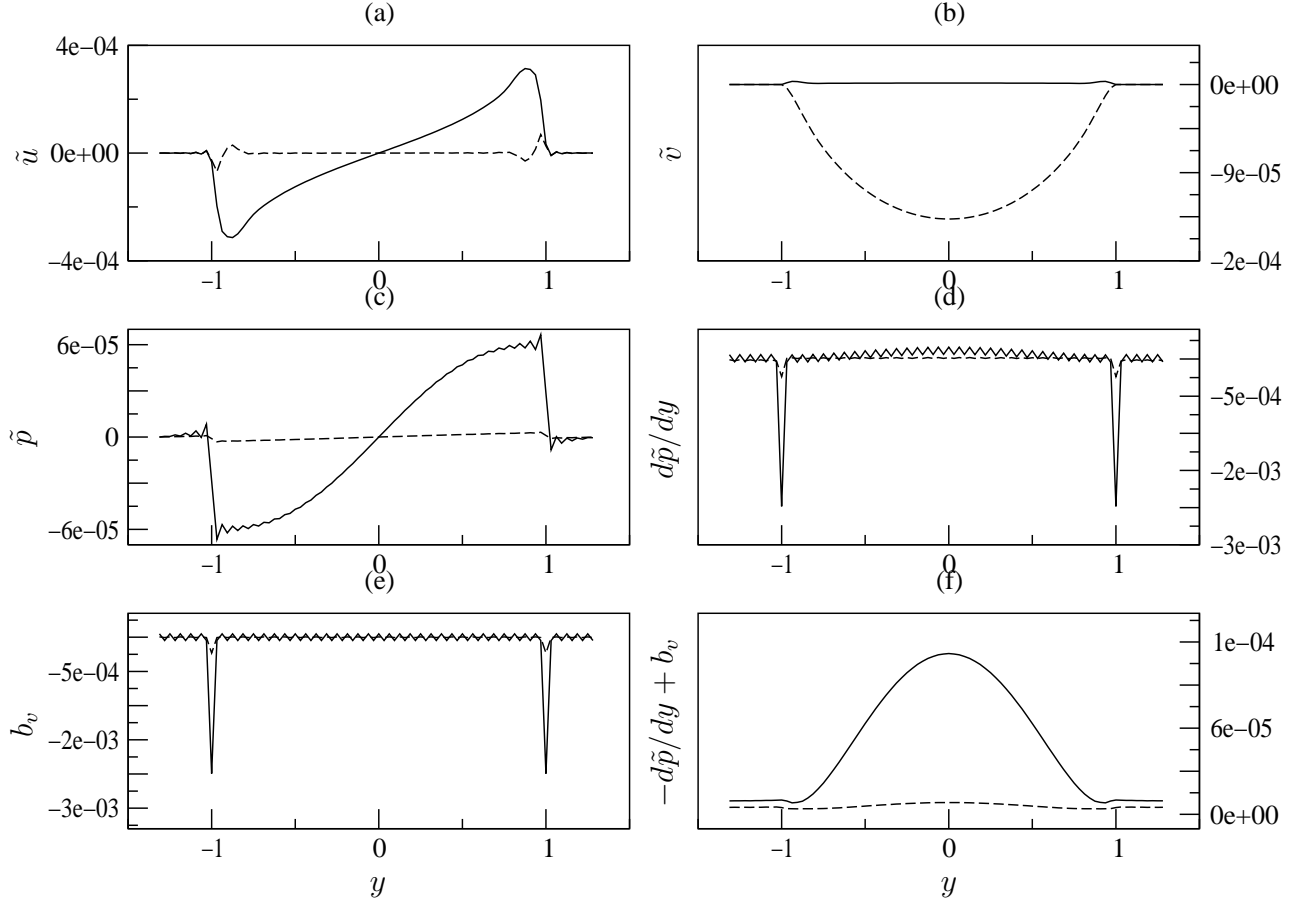


Figure 26: Effect of the boundary terms in the evolution of small disturbances in a channel flow. (a) filtered  $u$  velocity, (b) filtered  $v$  velocity, (c) filtered pressure, (d) pressure gradient, (e) boundary term for  $v$  equation, (f) pressure gradient + boundary term. — real part, - - - imaginary part.

To evaluate this approach, we consider two test cases: propagation of an Orr–Sommerfeld wave and low Reynolds number turbulence in a channel. In both cases, the Fourier cut-off filter is fine enough to make the model term  $M_i$  negligible.

In the Orr–Sommerfeld case, the simulated growth rate was within 0.25% of the exact value for the case considered. More interesting is the role the boundary term plays. Consider the exact unfiltered pressure fluctuations. They are formally zero in the exterior, resulting in a discontinuity in pressure, and the resulting Gibbs phenomenon in the filtered pressure is shown in figure 26c. The wall normal pressure gradient appears in the  $v$ -momentum equation, and this quantity is dominated by the filtered delta function at the boundary and the resulting Gibbs phenomenon (figure 26d). Yet the Gibbs phenomenon in velocity perturbations in figure 26a and b is imperceptible. The reason is that the term  $b_v$  (figure 26e) has exactly the same structure as the pressure gradient and cancels the Gibbs phenomenon (figure 26f). The role of the boundary terms in the momentum equation is thus to regularize the stress discontinuities at the wall (both pressure and viscous stresses).

To assess the applicability of this technique in simulating turbulent flow, a fully developed channel

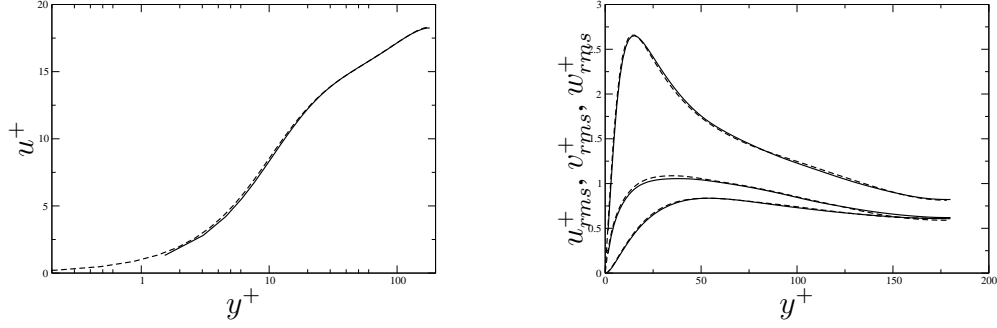


Figure 27: Mean (left) and rms (right) velocities in turbulent channel flow at  $Re_\tau = 180$ . ———present using filtered boundary formulation, — — —Moser et. al. (1999)

flow is computed on a  $128 \times 256 \times 128$  grid in  $x$ ,  $y$  and  $z$  respectively, with 20  $y$ -points in the buffer region. The friction Reynolds number is  $Re_\tau = 180$  and the domain size is the same as in the DNS of Moser *et al*<sup>38</sup>. The mean and rms velocities from this simulation are in excellent agreement with those from the DNS (see figure 27), and the near wall turbulence exhibits the familiar structures, such as streaks and inclined shear layers.

## 7.2 Optimal Large Eddy Simulation

Optimal LES is based on the observation that there is an ideal LES model, which guarantees correct single time statistics and minimum error in short-time dynamics<sup>1,23</sup>. This ideal model given by

$$m_i = \langle M_i | \tilde{u} = w \rangle, \quad (181)$$

where  $m_i$  is the model for the term  $M_i$  in (179),  $w$  is the LES field, and  $\tilde{u}$  is the filtered real turbulence. In essence, this is the average of  $M_i$  over all turbulence fields that map to the LES field through the filter. Unfortunately this model is intractable, so in optimal LES we approximate this model using stochastic estimation<sup>3,4,43</sup>. In the LES performed here, the stochastic estimation formulation is simplified by the homogeneity of the channel flow in directions parallel to the wall, and the formulation must be further simplified to avoid problems of over generalization<sup>28</sup>. The linear stochastic estimate used here can thus be written:

$$\hat{m}_i(y) = \langle \hat{M}_i \rangle + \hat{K}_{ij}(y) \hat{E}_j(y) \quad (182)$$

$$\langle \hat{M}_i'(y) \hat{E}_k^*(y) \rangle = \hat{K}_{ij}(y) \langle \hat{E}_j(y) \hat{E}_k^*(y) \rangle \quad (183)$$

where  $\hat{\cdot}$  indicates the Fourier transform, and the event vector  $E_j$  is a vector consisting of the fluctuating LES velocities  $w_j'$  and their  $y$  derivatives. The correlations appearing in (183) must be determined to complete the model. For the purposes of the test described below, the correlations were evaluated using the DNS data from Moser *et al*<sup>38</sup> at  $Re_\tau = 590$ . Using DNS data allows the optimal LES formulation to be evaluated without uncertainties introduced by further modeling of the correlations, or other modeling approximations.

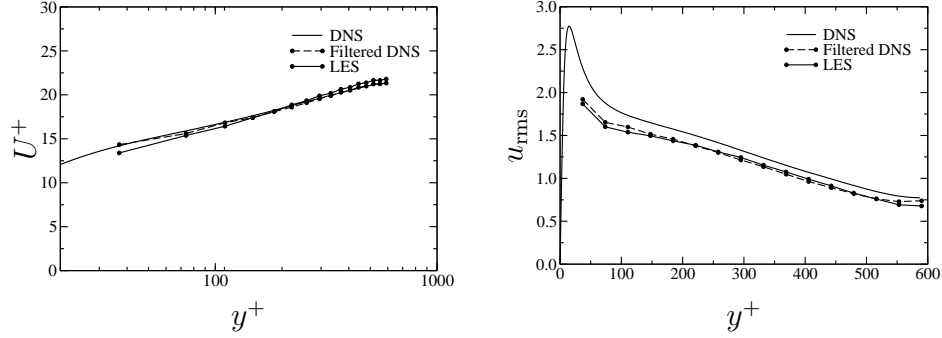


Figure 28: Mean velocity (left) and rms streamwise velocity fluctuations (right) in a turbulent channel at  $Re_\tau = 590$ . The LES was performed using the filtered boundary optimal LES formulation.

### 7.3 Filtered-Wall LES Results

The filtered boundary formulation and the optimal LES model were used to perform an LES of turbulent channel flow with bulk Reynolds number  $Re_b = 10,950$  corresponding to a channel with  $Re_\tau = 590$ . Periodic boundary conditions were used in streamwise ( $x$ ) and spanwise ( $z$ ) directions, with domain sizes  $L_x = 2\pi h$  and  $L_z = \pi h$  ( $h$  is the channel half width). DNS of this case was performed by Moser *et al*<sup>38</sup>, and optimal LES were performed by Volker *et al*<sup>28</sup>.

To accommodate the filtered boundary formulation, a buffer region is added outside the channel and periodic boundary conditions are used in the extended wall-normal ( $y$ ) domain. Fourier cut-off filters with effective filter widths of  $\Delta x^+ = 116$ ,  $\Delta y^+ = 37$  and  $\Delta z^+ = 58$  are used in the three spatial directions. In  $x$  and  $z$ , these are the same filters used in Volker *et al*<sup>28</sup>. Note that these filter widths are sufficiently large to eliminate the structure of the near-wall viscous and buffer layers.

The filtered boundary model and the optimal LES model were used to perform an LES of the channel flow. The statistical correlations required as input to the optimal LES formulation were determined from the DNS of Moser *et al*<sup>38</sup>. Sample results from this simulation are shown in figure 28. Note that despite the fact that the wall layer was not resolved, both the mean velocity and the rms velocities are in remarkably good agreement with the filtered DNS. Furthermore, the one-dimensional spectra in the  $x$  and  $z$  directions are in good agreement with the filtered DNS data.

It should be noted that the optimal LES form used here is the simplest of those proposed by Volker *et al*<sup>28</sup> for the channel, and that in that study models of this form performed poorly. The reason was that this form does not properly represent the wall-normal transport of energy and Reynolds stress. As pointed out by Haertel *et al*<sup>44</sup>, in the absence of wall-normal filtering, the contribution of the subgrid term to the resolved-scale energy equation is positive near the wall (see figure 29), which is due to the subgrid contribution to the transport of energy from the production peak to toward the wall. Volker *et al*<sup>28</sup> found that a more complicated form that did represent the wall normal transport produced a model that performed very well.

However, with coarse wall-normal filtering, the subgrid term is everywhere dissipative, as is also shown in figure 29. There is therefore no instability introduced by using the simple model form used here, with the result that the model produces high quality simulations, as shown above.

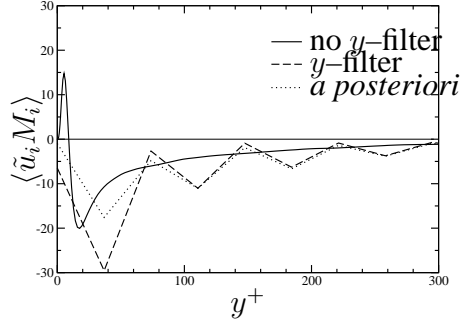


Figure 29: Subgrid energy transfer  $\langle \tilde{u}_i M_i \rangle$  in turbulent channel flow, as measured from DNS,<sup>38</sup> with and without wall-normal filtering, and *a posteriori* from the filtered-wall LES.

Also notice the large fluctuations (wiggles) in the profile of the subgrid dissipation shown in figure 29. The *a posteriori* dissipation from the LES reproduces these features, and is otherwise in general agreement with the *a priori* values. The reason for these oscillations is the Gibbs phenomenon introduced by filtering through the wall, and sublayer. These fluctuations are apparently important in the simulation, because they cancel similar Gibbs phenomena appearing in other terms, as with the Orr-Sommerfeld test case described in section 2.

## 7.4 Discussion

The results described above are intriguing because they suggest that it is not necessary to resolve the near-wall layer in an LES to obtain an accurate simulation of a wall-bounded flow. However, because the simulations reported here were based on knowledge of statistical correlations obtained from DNS, the work presented here does not constitute a practical broadly-applicable LES model. For this, the need for DNS statistical data must be overcome. None-the-less, the current results do demonstrate the value of the wall-filtering approach, and the “no-leakage” optimization model for the wall stresses. It would appear that this approach may form the foundation of a solution to the well-known LES wall modeling problem.

The results of this study are also curious, because the “no-leakage” model does not incorporate any information regarding the properties of the near-wall sublayer that has been filtered away. Whereas it has been commonly assumed that the wall boundary treatment must account for the presence of the sublayer. Further, the “no-leakage” model cannot by its nature account for the presence or absence of roughness. This raises the question of how information regarding near-wall properties of the turbulence (which are directly affected by roughness) is incorporated into the LES. The answer is that the nature of the near-wall turbulence is reflected in the subgrid fluctuations, which affect the LES through the subgrid model term  $M_i = -\partial \tau_{ij} / \partial x_j$ . In the simulation reported here, the optimal LES model of the subgrid term is formulated based on statistical data obtained from a smooth-wall DNS. Thus, the simulation produced results consistent with a smooth-walled channel. We propose that an optimal model formulated for a particular wall roughness would also produce an LES consistent with that rough wall.

It appears then, that the LES wall boundary condition problem may not be as difficult as has

been commonly believed. The filtered boundary, “no-leakage” formulation, appears to provide an adequate boundary condition. Instead, the challenge is the modeling of the volumetric subgrid stress term. However, at high Reynolds number, and with the sublayer effectively filtered out, the model need only represent the subgrid terms in the log-layer, where similarity scaling makes the modeling easier. As indicated above, it is also necessary that the effect of roughness on the log-layer subgrid model be characterized.

To relieve the need for DNS data, which was used for subgrid modeling here, a model for the subgrid term with minimal empirical input and which retains the good properties of the optimal LES model is needed. But, what properties of the subgrid model used here are important for LES performance in wall-bounded flows? The formulation of the optimal model provides guidance, because it was designed to accurately represent only the transfer of energy and Reynolds stress to the small scales, and the direct contribution of the subgrid to the mean Reynolds stress. More precisely, it provides an accurate representation of the dependence of the subgrid dissipation on the  $x$  and  $z$  wavenumbers and  $y$  location, as well as the anisotropy of the dissipation. Whether this much detail in the representation of the subgrid dissipation is needed, is not at this point clear, and is being investigated. Perhaps, if less detail is sufficient, standard models (e.g. Smagorinsky) may be applicable. However, such standard models are not likely to be able to produce the oscillatory behavior in the dissipation (figure 29), as our experience with dynamic Smagorinsky in this context shows. This suggests that the Fourier cut-off filter would be a poor choice for wall filtering, if standard subgrid models are to be used.

Finally, we note that the tests performed here were particularly arduous for the filtered boundary formulation because discontinuities in derivatives (as in the velocity at the wall) are poorly represented by Fourier spectral methods, with Gibbs phenomena as the result. It is particularly remarkable, then, that the wall stress model used here is able to treat and largely cancel this Gibbs phenomenon.

## 8 Other Information

This project was jointly funded by AFOSR under the subject grant and NSF under grant NSF-CTS-0352552. The following personnel were supported by these grants:

Henry Chang	Graduate student, University of Illinois, Urbana-Champaign Current Position: Graduate student, University of Texas at Austin
Amitabh Bhattacharya	Graduate student, University of Illinois, Urbana-Champaign
Prakash Vedula	Postdoc, University of Illinois, Urbana-Champaign Current Position: Professor, University of Oklahoma
Robert D. Moser	Professor, University of Illinois, Urbana-Champaign Current position: Professor, University of Texas at Austin
Ron J. Adrian	Professor, University of Illinois, Urbana-Champaign Current position: Professor, Arizona State University

A number of papers were published during the grant period based on research undertaken under this grant, and its predecessor. These are listed below:

### Publications

- Zandonade, P. S., Langford, J. A. & Moser, R. D. 2004 Finite volume optimal large-eddy simulation of isotropic turbulence, *Phys. of Fluids*, **16**, 2255-2271.
- de Alamo, J. C., Jimenez, J., Zandonade, P. & Moser, R. D. 2004 Scaling of the energy spectra of turbulent channels, *J. Fluid Mech.*, **500**, 135-144.
- Langford, J. A. & Moser, R. D. 2004 Optimal large-eddy simulation results for isotropic turbulence *J. Fluid Mech.* **521**, 273-294.
- Adrian, R. J., 2005 Twenty Years of particle image velocimetry, *Exp. Fluids* **39**, 159-169.
- Chakraborty, P. Balachandar, S., and Adrian, R. J., 2005 On the relationships between local vortex identification schemes, *J. Fluid Mech.* **535**, 189-214.
- Tomkins, C. D. and Adrian, R. J. 2005 Energetic spanwise modes in the logarithmic layer of a turbulent boundary layer, *J. Fluid Mech.* **545**, 141-162.
- Vedula, P. & Moser, R. D. 2005 On the validity of quasi-normal approximation in turbulent channel flow, *Phys. of Fluids* **17** 055106.
- Vedula, P., Adrian & R. J. 2005 Optimal solenoidal interpolation of turbulent vector fields: application to PTV and super-resolution PIV, *Experiments in Fluids* **39**, 213-221.
- Moser, R. D. 2006 On the Validity of the Continuum Approximation in High Reynolds Number Turbulence, *Phys. of Fluids* **18**, to appear.
- del Alamo J. C., Jimenez J., Zandonade, P., Moser, R. D. 2006 Self-similar vortex clusters in the turbulent logarithmic region *J. Fluid Mech.* **561** 329-358.
- Ewing, D., George, W. K., Rogers, M. M. & Moser, R. D. 2006 Two-Point Similarity in Temporally Evolving Plane Wakes, *J. FLuid Mechanics* (to appear)
- Guala, M., Hommema, S. E., and Adrian, R. J. 2006 Large-scale and very-large-scale motions in turbulent pipe flow, *J. Fluid Mech.* **554**, 521-542.
- Balakumar, B. J. and Adrian, R. J. 2007 Large and very-large scale motions in channel and boundary-layer flow, to appear in *Philosophical Transaction Of The Royal Society A* **365**, 665-681.
- Jimenez, J. and Moser, R. D. 2007 What are we learning from simulating wall turbulence?, *Philosophical Transaction Of The Royal Society A*, **365**, 715-732.



Adrian, R. J., 2007 Organization in wall turbulence, *Phys. Fluids* (to appear).  
Adrian, R. J. 2007 Stochastic estimation of vector field data, to appear in *Handbook of Experimental Fluid Dynamics*.

## Acknowledgment/Disclaimer

The authors are indebted to Prof. P. Vedula, Dr. P. Zandonade, Mr. A. Battacharya and MR. H. Chang for their critical contributions to this research.

This work is jointly sponsored by the National Science Foundation and the Air Force Office of Scientific Research, USAF, under grant/contract numbers NSF-CTS-0352552 and F49620-04-1-0032. The views and conclusions contained herein are those of the authors and should not be interpreted as necessarily representing the official policies or endorsements, either expressed or implied, of the Air Force Office of Scientific Research or the U. S. Government.

## References

- [1] J. Langford and R. Moser, Optimal LES formulations for isotropic turbulence, *Journal of Fluid Mechanics* **398**, 321 (1999).
- [2] J. Langford, *Toward Ideal Large-Eddy Simulation*, PhD thesis, University of Illinois at Urbana-Champaign, 2000.
- [3] R. Adrian, B. Jones, M. Chung, Y. Hassan, C. Nithianandan, and A. Tung, Approximation of turbulent conditional averages by stochastic estimation., *Physics of Fluids* **1**, 992 (1989).
- [4] R. Adrian, Stochastic estimation of sub-grid scale motions., *Applied Mechanics Review* **43**, 214 (1990).
- [5] M. Oberlack, Invariant modeling in large-eddy simulation of turbulence., in *Annual Research Briefs*, Center for Turbulence Research, 1997.
- [6] S. Kassinos, W. Reynolds, and M. Rogers, One-point turbulence structure tensors, *Journal of Fluid Mechanics* **428**, 213 (2001).
- [7] I. Proudman and W. H. Reid, On the decay of a normally distributed and homogeneous turbulent velocity field, *Phil. Trans. R. Soc. Lond. A* **247**, 163 (1954).
- [8] P. S. Zandonade, J. A. Langford, and R. D. Moser, Finite volume optimal large-eddy simulation of isotropic turbulence, *Physics of Fluids* **16**, 2255 (2004).
- [9] A. N. Kolmogorov, The local structure of turbulence in incompressible viscous fluid for very large Reynolds numbers, *Doklady Akademii Nauk SSSR* **30**, 301 (1941), In Russian.
- [10] A. N. Kolmogorov, Dissipation of energy in a locally isotropic turbulence, *Doklady Akademii Nauk SSSR* **32**, 19 (1941), In Russian.

- [11] A. N. Kolmogorov, The local structure of turbulence in incompressible viscous fluid for very large Reynolds numbers, *Proceedings of the Royal Society, Series A—Mathematical and Physical Sciences* **434**, 9 (1991), Translation to English.
- [12] A. N. Kolmogorov, Dissipation of energy in a locally isotropic turbulence, *Proceedings of the Royal Society, Series A—Mathematical and Physical Sciences* **434**, 15 (1991), Translation to English.
- [13] A. N. Kolmogorov, A refinement of previous hypotheses concerning the local structure of turbulence in a viscous incompressible fluid at high Reynolds number, *Journal of Fluid Mechanics* **13**, 82 (1962).
- [14] A. S. Monin and A. M. Yaglom, *Statistical Fluid Mechanics: Mechanics of Turbulence*, volume 2, MIT Press, Cambridge, Mass., 1975.
- [15] P. Vedula, P. Zandonade, and R. D. Moser, Validity of quasi-normal approximation in turbulent channel flow, *Physics of Fluids* **17**, 055106 (2005).
- [16] M. Lesieur, *Turbulence in Fluids*, Kluwer Academic Publishers, Dordrecht, 3rd edition, 1997.
- [17] I. Proudman and W. H. Reid, On the decay of a normally distributed and homogeneous turbulent velocity field, *Philosophical Transactions of the Royal Society* **A247**, 163 (1954).
- [18] R. D. Moser, Personal communication, 2003.
- [19] P. S. K. Zandonade, *Finite-Volume Optimal Large-Eddy Simulation*, PhD thesis, University of Illinois at Urbana-Champaign, Urbana, IL, 2007.
- [20] A. J. Chorin, Numerical solution of the navier-stokes equations, *Mathematics of Computation* **22**, 745 (1968).
- [21] M. M. Rogers and R. D. Moser, Direct simulation of a self-similar turbulent mixing layer, *Physics of Fluids* **6**, 903 (1994).
- [22] U. Frisch, *Turbulence: The Legacy of A. N. Kolmogorov*, Cambridge U. Press, 1995.
- [23] S. B. Pope, *Turbulent Flows*, Cambridge University Press, 2000.
- [24] T. von Karman and L. Howarth, On the statistical theory of isotropic turbulence, *Proc. R. Soc. Lond. A* **164**, 192 (1938).
- [25] A. N. Kolmogorov, Dissipation of energy in locally isotropic turbulence, *Dokl. Akad. Nauk SSSR* **32**, 16 (1941), reprinted in *Proc. R. Soc. Lond. A* **434** 15-17 (1991).
- [26] J. A. Langford and R. D. Moser, Optimal large-eddy simulation results for isotropic turbulence, *Journal of Fluid Mechanics* **521**, 273 (2004).
- [27] A. N. Kolmogorov, The local structure of turbulence in incompressible viscous fluid for very large Reynolds number, *C. R. Acad. Sci. URSS* **30**, 301 (1941), reprinted in *Proc. R. Soc. Lond. A* **434** 9-13 (1991).
- [28] S. Volker, P. Venugopal, and R. D. Moser, Optimal large eddy simulation of turbulent channel flow based on direct numerical simulation statistical data, *Physics of Fluids* **14**, 3675 (2002).

- [29] S. Orszag, Statistical theory of turbulence, in *Fluid Dynamics, 1973 Les Houches Summer School of Theoretical Physics*, edited by R. Balian and J. L. Peube, 1977.
- [30] A. Salhi and C. Cambon, Advances in rapid distortion theory: From rotating shear flows to the baroclinic instability, *Journal of Applied Mechanics* **73**, 449 (2006).
- [31] I. Arad, V. S. L'vov, and I. Procaccia, Correlation functions in isotropic and anisotropic turbulence: The role of the symmetry group, *Phys. Rev. E* **59**, 6753 (1999).
- [32] A. Spencer, Theory of invariants, in *Continuum Physics*, edited by A.C.Eringen, 1971, volume 1, pp. 239–353.
- [33] I. Arad, B. Dhruva, S. Kurien, V. L'vov, I. Procaccia, and K. Sreenivasan, Extraction of Anisotropic Contributions in Turbulent Flows, *Physical Review Letters* **81**, 5330 (1998).
- [34] R. Brent, *Algorithms for Minimization Without Derivatives*, Dover Publications, 2002.
- [35] S. C. Kassinos, B. Knaepen, and D. Carati, The transport of a passive scalar in magneto-hydrodynamic turbulence subjected to mean shear and frame rotation, *Physics of Fluids* **19**, 015105 (2007).
- [36] M. Lee, J. Kim, and P. Moin, Structure of turbulence at high shear rate, *Journal of Fluid Mechanics* **216**, 561 (1990).
- [37] U. Piomelli and E. Balaras, Wall-layer models for large-eddy simulations, *Ann. Rev. Fluid Mech.* **34**, 349 (2002), To appear.
- [38] R. Moser, J. Kim, and N. Mansour, Direct numerical simulation of turbulent channel flow up to  $Re_\tau = 590$ , *Phys. Fluids* **11**, 943 (1999).
- [39] E. Balaras, C. Benocci, and U. Piomelli, Two-layer approximate boundary conditions for large-eddy simulations, *AIAA Journal* **34**, 1111 (1996).
- [40] R. Verzicco, J. Mohd-Yusof, P. Orlandi, and D. Haworth, Les in complex geometries using boundary body forces, Technical Report Annual Research Briefs, Center for Turbulence Research, Stanford University, 1998.
- [41] J. Mohd-Yusof, Development of immersed boundary methods for complex geometries, Technical Report Annual Research Briefs, Center for Turbulence Research, Stanford University, 1998.
- [42] A. Das and R. D. Moser, Filtering boundary conditions for les and embeded boundary simulations, in *Proc. International conference on DNS/LES, 3rd*, edited by L. S. C. Liu and T. Beutner, Greyden Press, 2001.
- [43] R. Adrian, On the role of conditional averages in turbulence theory., in *Turbulence in Liquids*, edited by J. Zakin and G. Patterson, Science Press, Princeton, New Jersey, 1977, pp. 323–332.
- [44] C. Härtel and L. Kleiser, Analysis and modelling of subgrid-scale motions in near-wall turbulence, *J. Fluid Mech.* **356**, 327 (1998).